EFFECTS OF MATERIAL TREATMENTS ON GROWTH KINETICS OF PASSIVE FILMS ON STEEL ALLOYS

Vom Fachbereich Produktionstechnik
der
UNIVERSITÄT BREMEN

zur Erlangung des Grades
Doktor-Ingenieur
genehmigte

Dissertation

von
Ingmar Bösing, M.Sc.

Gutachter: Prof. Dr.-Ing. Jorg Thöming
Prof. Dr. Fabio La Mantia

Tag der mündlichen Prüfung: 02.12.2020

CHEMISCHE VERFAHRENS-TECHNIK

Universität Bremen

ZUSAMMENFASSUNG

Die Welt, die wir kennen und in der wir leben, wäre ohne Metalle undenkbar. Die Möglichkeit, die Eigenschaften der verschiedensten Metalle durch Kombination von unterschiedlichen Elementen und durch Materialbehandlungen unseren Bedürfnissen anzupassen, prägt die Technik und die Wissenschaft. So kann das Mikrogefüge eines Stahls mit Hilfe einer Wärmebehandlung verändert werden, und dieses wiederum beeinflusst die Eigenschaften der jeweiligen Legierung. Ein entsprechendes, in der Industrie etabliertes Verfahren ist zum Beispiel das Härten martensitischen Stahls. Dabei wird durch eine Kombination von Austenitisieren, also dem Erhitzen des Materials bis sich ein austenitisches Gefüge einstellt, gefolgt vom schnellen Abschrecken, ein neues Gefüge im Stahl erzielt.

Das Härten von martensitischem rostfreiem Stahl wird unter anderem verwendet, um Werkzeugstahl herzustellen, daher ist dieser Prozess aus der materialverarbeitenden Industrie nicht mehr wegzudenken und die Einflüsse des Härtens auf das Mikrogefüge sind intensiv untersucht worden. Durch das schnelle Abschrecken verbleibt der Kohlenstoff in der tetragonal raumzentrieten Kristallstruktur des Martensits und übersättigt diesen. Diese Übersättigung an Kohlenstoff führt zu der gewünschten gesteigerten Härte des Stahls. Neben der Änderung der Phase können sich aber auch verschiedene Karbide, abhängig von der Temperatur, auflösen. Dies führt zu einer Erhöhung des Kohlenstoffs, aber auch zu mehr Eisen oder Chrom im Kristallgitter.

Obwohl der Einfluss der Mikrostrukturänderungen auf die mechanischen Eigenschaften intensiv untersucht wurde und gut verstanden ist, besteht noch immer keine Einigkeit bezüglich des Effekts des Härtens auf die Langlebigkeit des Materials. Zahlreiche in den letzten 20 Jahren veröffentlichte Publikationen kommen zu teilweise widersprüchlichen Ergebnissen. So wurden sowohl Ab- als auch Zunahmen des Korrosionswiderstands in Folge des Härteprozesses beobachtet. Diese Widersprüche liegen zum Teil an den unterschiedlich durchgeführten Messungen, aber auch daran, dass der Einfluss der Mikrostruktur auf die Korrosion und die Passivität, die schützende Oxidschicht auf der Metalloberfläche, nicht hinreichend verstanden ist.

Im Rahmen dieser Arbeit wurden umfassende elektrochemische Messungen mit Modellierungen des Passivschichtwachstums kombiniert, um diese Widersprüche zu lösen.

Zudem wurden die physikalischen Ursachen für das geänderte elektrochemische Verhalten in Folge des Härtens von martensitischem Stahl ergründet. Es konnte gezeigt werden, dass zwischen unterschiedlichen Korrosionphänomenen differenziert werden muss. Zum einen kann eine Änderung der Mikrostruktur das Wachstum und die Auflösung der Passivschicht beeinflussen. Dies führt zu unterschiedlichem Materialverlust im passivierten Zustand. Darüber hinaus kann aber auch der Zusammenbruch der schützenden Passivschicht sowie die Materialauflösung nach dem Zusammenbruch der Schicht durch die Mikrostruktur beeinflusst werden. Durch die elektrochemischen Messungen ist es möglich den Einfluss der Mikrostruktur auf die unterschiedlichen Korrosionsmechanismen zu beschreiben. Die anschließende Modellierung des Passivschichtwachstums führt zu einer Erklärung der physikalischen Ursachen der Beobachtungen.

Das beschriebene Härteverfahren wurde anschließend auf eine weitere Legierung, einen niedrig legierten Wälzlagerstahl, übertragen. Dieses Material zeigt etwas andere Mikrostrukturänderungen in Folge der gleichen Wärmebehandlung. So verändert sich vor allem das Verhältnis zwischen Martensit und Austenit, wohingegen die Auflösung der Karbide weniger Einfluss auf das Korrosionsverhalten hat. Eine Zunahme der Martensitphase führte zu einer beschleunigten Auflösung der Passivschicht im passivierten Zustand. Auch der Zusammenbruch der Passivschicht ist durch die Martensitphase beeinflusst, die beobachteten Effekte wurden allerdings durch den Einfluss von weiteren Mikrostruktureigenschaften überlagert.

Um den Einfluss der Martensitphase auf die Passivschicht isoliert zu untersuchen wurde eine weitere Messreihe durchgeführt. Die Modellierung auf Basis des Point Defect Models konnte zeigen, dass eine Zunahme der Martensitphase zu einer beschleunigten Auflösung des Metalls an der Metall/Passivschicht-Grenzfläche, sowie eine beschleunigten Auflösung der Passivschicht an der Passivschicht/Elektrolyt-Grenzfläche führt.

Das Point Defect Model zur Beschreibung des Wachstums von Oxidschichten auf Modellen wurde das erste Mal in der Arbeitsgruppe von Digby Macdonald in den frühen 1980er Jahren vorgestellt und wird seitdem immer weiterentwickelt. Zwar wurde das Modell immer wieder an einzelnen Materialien erprobt, doch ist diese Arbeit der erste Fall in dem das Modell zum Vergleich zwischen verschiedenen Materialien genutzt wurde. Um die Arbeit mit dem Point Defect Model in den Materialwissenschaften zu etablieren, kann diese Thesis als Handbuch zum Vorgehen genutzt werden. Daher liegt der Fokus nicht nur auf den materialwissenschaftlichen Erkenntnissen, sondern es ist auch eine breite Basis an Theorie bezüglich des Point Defect Models gegeben. Eine ausführliche Beschreibung der Wachstumskinetik der Passivschicht ist gefolgt von der Herleitung des Impedanzmodells, basierend auf dem Point Defect Model. Um den Einfluss der einzelnen kinetischen Parameter auf die Wachstumskinetik und auf das Impedanzverhalten aufzuzeigen, wurde eine ausführliche Sensitivitätsanalyse durchgeführt.

ABSTRACT

The possibility to adjust the properties of metals, particularly steel, by a combination of elements and material treatments, enables the metal-based civilization as we know it and we live in. The heat treatment of steel can be used to change the microstructure and these microstructure changes affect the properties of the material. A very common heat treatment is the hardening, which is done by a combination of austenitizing, the heating of the steel up to temperatures at which austenitic crystal structure is achieved, followed by quenching, the cooling of the material with high temperatures gradients.

Hardening of martensitic stainless steel enables the use of iron-carbon-chromium alloys as tool steels for the processing of various materials. This process is long known and the effects of the hardening procedure on the microstructure are well investigated. The hardening of martensitic stainless steel leads to the formation of a martensitic crystal structure. Martensite has a body centered tetragonal structure with several carbon atoms embedded in the lattice, which increases the hardness. Additional to the phase transformation, the carbides (namely iron and chromium carbides) can dissolve depending on the austenitizing temperature.

Although the mechanical properties changes resulting from this process are well understood, the impact on the longevity and durability of the materials is a matter of debate. Several publications regarding this process came to contrary results and predicted increased corrosion resistance as well as decreased corrosion resistance resulting from the hardening process. These contradictions are due to different measurements and due to the fact that the impact of the microstructure on the corrosion behavior and the passivity are not fully understood.

By a combination of comprehensive electrochemical measurements and kinetic modeling of passive film growth, this contradiction is solved in this thesis. It is shown that it is necessary to distinguish between the material dissolution in the passivated state, the breakdown of the passive film, which leads to active dissolution, and the dissolution in the active state. These different mechanisms of corrosion can be affected in different ways by the microstructure changes. While the electrochemical measurements are used to compare the behavior of the material during the different stages of corrosion, the modeling is used to reveal the physical causes that lead to the differing behavior.

In the following part of the thesis, the heat treatment process is used at another alloy. The investigated, low alloyed, bearing steel shows different microstructure changes due to the same heat treatment. These different changes, especially the differing martensite/austenite phase ratio, affects the electrochemical properties in another way. A higher martensite content accelerates the passive film formation and the film dissolution. The film breakdown, and thus the transition to the active dissolution is also affected by the martensite content. Furthermore, both, film dissolution and film breakdown, are also affected by the carbide dissolution.

To isolate the effect of the martensite content on the passive film growth, an additional sample set, consisting of three samples, which differs only in martensite content, is produced by rotary swaging. The modeling of passive film kinetics could confirm the observations done at the bearing steel. The faster formation of passive film at the metal/film interface as well as the faster dissolution of the film at the film/solution interface lead to faster material loss, in the active state as well as in the passivated state.

In addition to the material scientific investigations during the work on this thesis, the kinetic modeling of passive film growth is developed as a tool in material science. The modeling of the passive film growth is based on the Point Defect Model, which is used during these investigations, was first presented by the working group of Digby Macdonald in the early 1980s and is further developed since then. The present work is the first case the model was used, to compare the kinetic parameters of different materials and thus to evaluate the influence of microstructure on the passive film kinetics. For this reason, this thesis can also be used as a guide for the work with the Point Defect Model in material science. Therefore, the theoretical background of passive film kinetics, the Point Defect Model, the derivation of the impedance model resulting from the Point Defect Model and the reduction of the model to make it suitable for the fitting is given. Furthermore, a sensitivity analysis regarding the different kinetic parameters is presented for a better understanding of the impact of single parameters on the passive film kinetics and the impedance behavior.

ACKNOWLEDGEMENTS

Science may never come up with
a better office communication
system than the coffee break.
Earl Wilson

I started the work on this thesis November 2016 at the Center for Environmental Research and Sustainable Technology in the chemical process engineering working group. During the work on this project, I was part of the collaborated research center SFB 1232, which was funded by the German Research Association (DFG). My project as part of the collaborated research center was entitled "Electrochemical High Throughput Characterization of Metallic Micro-Probes" and was supervised by Jorg Thöming and Michael Baune. Both, Jorg Thöming and Michael Baune, have created a working atmosphere and group in which I really enjoyed to work (at least most of the time).

I would like to thank Mr. Thöming for the supervision during the last years, the possibility to follow my scientific interests and the numerous opportunities to discuss my scientific work. Especially because my research topic was unique in our working group, I am thankful for all the time of fruitful discussions.

My second supervisor was Michael Baune, who supported me over the last years and always lend an ear to me, independently if it was for work related discussions or some conversations over a coffee (or milk in my case). I think Michael is one of the main reasons for the warm and friendly atmosphere in our working group, which I and several of my coworkers strongly appreciate.

Furthermore, I would like to thank Georg Pesch, who proof read some of my publications and gave me several advices regarding the scientific world. Without him, all my figures would be labeled with Calibri (and I wonder if anyone else would care). Georg already worked in the group when I started my PhD and I am happy that we became good friends, also outside of work.

Two friends I know from the times as a student at the University of Bremen, Jan Ilsemann and Simon Kunze, have agreed to proofread parts of my work, for which I am grateful. Furthermore, Jan was writing his thesis at the same time as me and it was nice to have a friend to rant with about all the difficulties during this process.

I wrote this thesis during the so-called “Corona crisis”. During the last weeks, my fiancée Lena Milchert and I worked together in home office. I am very happy to have you in my life and to have your support. I cannot imagine anyone else with whom I would enjoy spending every day in home office. Thank you for your support, every cup of tea and for your patience every time I was unresponsive because I was thinking about work and this thesis.

Special thanks also go to my parents, who were always there for me and without whose support I would not have come this far. Thank you for always believing in me and encouraging me to do what I enjoy.

LIST OF PUBLICATIONS

Bösing, Ingmar, Jorg Thöming, and Michael Baune. "Electrolyte composition for distinguishing corrosion mechanisms in steel alloy screening." *International Journal of Corrosion* 2017 (2017).

Bösing, Ingmar, et al. "The influence of microstructure deformation on the corrosion resistance of cold formed stainless steel." *MATEC Web of Conferences*. Vol. 190. (2018).

Bösing, Ingmar, et al. "Influence of heat treatment on the microstructure and corrosion resistance of martensitic stainless steel." *AIP Advances* 9.6 (2019).

Steinbacher, Matthias, et al. "Descriptors for High Throughput in Structural Materials Development." *High-Throughput* 8.4 (2019): 22.

Imani Moqadam, Saeedeh, et al. "Reproducibility of High-Throughput Sample Properties Produced by a High-Temperature Molten Metal Droplet Generator." *Metals* 10.3 (2020): 297.

Bösing, Ingmar, et al. "Influence of Systematically Changed Martensite Content on the Passive Film Properties of Austenitic Stainless Steel in Neutral Electrolyte." *Int. J. Electrochem. Sci* 15 (2020).

Bösing, Ingmar, Georg Marquardt, and Jorg Thöming. "Effect of Heat Treatment of Martensitic Stainless Steel on Passive Layer Growth Kinetics Studied by Electrochemical Impedance Spectroscopy in Conjunction with the Point Defect Model." *Corrosion and Materials Degradation* 1.1 (2020): 6.

Content

1

PROLOGUE

"Science is a wonderful thing
if one does not have to earn one's living at it"
Albert Einstein

1.1 INTRODUCTION

The above quote should, of course, be understood with a wink. In the last few years, in which I was lucky enough to earn my living with science, my interest in it has not faltered. Nevertheless, there are some adversities and contradictions in science that can drive a scientist crazy. A contradiction that I came across at the beginning of the work on this thesis comes from the field of corrosion science. Although the topic of corrosion of the ubiquitous material

steel, which is of great economic interest, is omnipresent, the contradiction I faced was unresolved. This thesis is dedicated to this contradiction in corrosion science and gives a solution with the help of a model of passive film growth kinetics. In the following, I will give a short introduction to the discussed topic and contradiction, a detailed discussion of the involved research is presented in Chapter 5.

Broad ranges of steels are used in a wide variety of applications worldwide, from the construction area to mobility and energy sector. The possibility to adjust these materials to countless areas of applications is unique. This variety is due to a combination of different alloying elements and material treatments. Both can change the hardness, ductility, deformability and durability.

The individually coordinated heating and cooling of steel can increase its hardness drastically. The effect of hardening of so-called martensitic stainless steel on its mechanical properties is long known. Due to the hardening process it is possible to increase the hardness up to a level at which the operational capability of tool steel is guaranteed. However, even though, steel and its different treatments are omnipresent, the consequences of these procedures on the durability of the material were long unknown and are still a matter of debate.

A research paper published in the early 2000s revealed increasing corrosion damage due to the hardening process. With increasing hardness the resistance to corrosion seemed to decrease drastically [1]. Especially at so-called stainless steel, the consequences of corrosion can be dramatic since the corrosion attacks are often invisible but can lead to material failure.

In the following years more researchers addressed the question which effect the hardening of martensitic stainless steel has on the corrosion behavior [2–7]. Surprisingly, the observed effects clearly contradicted each other in some cases. Some experiments seemed to confirm the findings of the first publication while other experiments predicted a better resistance against corrosion with an ongoing hardening process. On the one hand, this might be due to the complex influence of such a seemingly simple process on the material and its microstructure. On the other hand, the physical reasons for the observed phenomena are often not completely understand. However, understanding the interactions between material treatment, microstructure and the physio-chemical properties of the material plays a crucial role in understanding the corrosion behavior, predicting metallic material longevity and paving the way to safer but also more durable steels.

This thesis addresses exactly this question of the effect of hardening on the corrosion behavior, with its contrary answers and not fully understood physical causes. Electrochemical measurements are combined with kinetic modeling to investigate the physical causes of the observed electrochemical behavior and to distinguish and clarify the observed and seemingly contrary effects. The presented method can be used for a deeper understanding of the corrosion behavior of the metals surrounding us in our civilization at all times.

1.2 A SHORT HISTORY OF METALS IN OUR CIVILIZATION

The use of metals from early tools up to complex high-entropy alloys has a long history and is inextricably linked to the development of human society. The influence of metals on our civilization is so great that individual ages are named after the use of these materials. After the Stone Age, which ended 2200 BCE, the copper age started with the mining of copper and the first metallurgic technologies. But the use of metals was restricted to the pure elements [8]. The following Bronze Age, which lasted until 800 BCE was marked by the usage of the copper alloy bronze giving this age its name. Due to the uneven distribution of the resources copper and tin, trading was expanded and prosperity gained. The following Iron Age begins with the widespread of use of iron and steel tools as well as weapons over the use of bronze [9]. Before this time iron minerals were often used as coloring for cult events. For the common use of metallic iron, it was necessary to reduce the iron ores to pure iron. Depending on the region, traces of iron smelting could be traced back to 3000 BCE. But these finds were individual items of jewelry. The widespread use of iron in Europe starts at ca. 800 BCE which marks the beginning of this age. The Hittites in Asia in contrast, were much earlier able to process the, in this region common, magnetite to iron and steel. They already developed iron-based weapons and tools in the 15th century BCE. This knowledge could be one reason for their high influence in Asia over several centuries. Only after their empire was smashed their metallurgic technologies spread [10]. The Hallstatt burial ground in Austria marks the beginning of the Iron Age in Europe. This site contains numerous graves that were filled with iron and steel goods, such as weapons and jewelry [10]. Several hundreds of years later, the development of blast furnaces in the 14th century made the mass processing of iron and steel possible [11]. The age of industrialization (19th century) continued to boost this development and the use of iron alloys as construction material, for machine tools and steam locomotives but also for tanks and other weapons was possible [12].

During all this time, all steel constructions are subject to aging and deterioration. Humankind has developed several ways to slow down the processes of corrosion and to increase the longevity of steel construction. From addition of alloying elements like chromium to increase the natural corrosion protection in form of passivity (which will be discussed in detail in Chapter 3) to material treatments, coatings or technical solutions like galvanic anodes for cathodic protection. Nevertheless, the annual costs of corrosion damage worldwide are around 1.8 trillion US$ [13]. But containing corrosion plays not only a major economic role, but also in terms of sustainability, resource conservation and energy consumption. The understanding of the underlying corrosion mechanisms is key to prevent them and to develop methods to protect the steel regarding more sustainable materials. As part of this work, the

mechanism behind the influence of microstructure changes on the corrosion behavior, especially the passive film growth, shall be examined. As a new method, modeling based on the Point Defect Model is used to compare effects of material treatment on the passivity and its breakdown. All with the aim of a deeper understanding of material treatment effects on the longevity of materials and thus to enable advanced material science and development.

1.3 Structure and Aim of this Thesis

The focus of the thesis are the investigations of treatment effects and resulting microstructure changes on the corrosion behavior of carbon steel alloys. But this thesis is not only a presentation of experimental and theoretical results. It also presents PDM fitting as a new method in corrosion research to gain deeper insights to physical reasons of corrosion damages. For this purpose, the single chapters of this thesis have different priorities.

The basic electrochemical phenomena and measurement techniques that are necessary to understand both the experimental and modeling procedures are presented in Chapter 2. The chapter is based on 4 different textbooks. Since it is not my concern to replace these textbooks the introduction to the topics is somewhat steep. But the basic knowledge about electrochemistry and the theories presented in Chapter 2 should suffice to understand all results presented while interested readers are referred to the textbooks.

Chapter 3 takes a closer look at the phenomenon of passivity. Beginning with a short overview of the research of passivity, the fundamental principles presented are always linked to the passivity of steel alloys. A main part of the chapter is on film growth models, especially the Point Defect Model (PDM). A more qualitative description, which should be sufficient to understand the principles and the fitting results, is followed by a detailed mathematical derivation of the impedance model. This is particularly interesting for those readers that wish to work with the model by themselves.

The reduction of the model as well as the used dependencies are explained in Chapter 4. The PDM is grown over the years since its first presentation in the early 1980s. The claim of the model is a comprehensive description of all possible processes during passive film growth. This advantage of an advanced comprehensive model can be a weakness at the same time. The determined impedance data are often not sufficient to fit all model parameters and overfitting is possible. To avoid this the model is reduced to the necessary processes.

As a process engineer, material science was a completely new world to me. For all those who feel the same way, the beginning of Chapter 5 offers a brief overview of the material science basics. Later in the chapter, the existing scientific literature regarding the influence

of material treatment/microstructure and corrosion is presented. The topic of corrosion science and much more the topic material science have been around for many years. Accordingly, the scientific literature regarding both is numerous and detailed. To narrow it a bit down, I decided to put the focus on exactly the heat treatment I was investigating, the austenitizing process, and its effect on corrosion properties. Austenitizing changes different microstructure properties. For this reason, the effect of these single microstructure properties on corrosion behavior and passivity is also presented.

Whoever is only interested in the results can directly start with Chapter 6. The effect of austenitizing on martensitic stainless steel is presented in this chapter. Beginning with the experimental investigations and followed by the kinetic modeling. The results of this chapter have already been published in *AIP Advances* (9) 2019 [14] and *Corrosion and Material Degradation* (1) 2020 [15]. By merging the results in one joint chapter it is possible to arrive at a comprehensive conclusion.

The transfer of the same heat treatment on another alloy system is presented in Chapter 7. It is shown that the same heat treatment has different effects on the microstructure of the second alloy. Thus, the effects on the corrosion behavior and passive film kinetics differ as well. Nevertheless, we will see that the same microstructure changes result in the same changes of kinetic parameters.

From Chapter 7 it could be concluded that the microstructure parameter with the biggest impact on the passive film kinetics is the martensite content. To verify this, the martensite content is changed independently from other microstructure parameters. The strong effect on the passive film growth kinetics of the phase change (austenitic/martensitic) is presented in Chapter 8. The experimental results of this chapter have been published in *Matec Web of Conferences* 190 (2018) [16] and *International Journal of Electrochemical Science* 15 (2020) [17].

A sensitivity analysis of the single kinetic parameters on the impedance model as well as on the passive film thickness and the corrosion behavior is given in Chapter 9. This is especially interesting for the use of kinetic fitting as a method in corrosion science and to use the model to predict long term corrosion behavior. I will also give some thoughts about possible ways to investigate the breakdown of passivity by EIS measurements in the passive state.

A comprehensive summary of the results and on the use of the PDM as a tool for the investigation of material treatments on the corrosion behavior and their physical origin is given in Chapter 10. In addition to the critical discussion of the presented results an outlook about possible ways to parametrize a more comprehensive kinetic model is given.

2

Electrochemical Principles

We know very little, and yet it is astonishing
that we know so much, and still more astonishing
that so little knowledge can give us so much power
Bertrand Russell

The measurement techniques and the model used for the investigations presented in this thesis all base on electrochemical principles. In this chapter the basic electrochemical phenomena and measurement techniques and principles of corrosion are introduced. The aim of this chapter is to give an overview and to enable the understanding of the presented measurements. The busy reader (or those who are already equipped with sufficient knowledge of electrochemistry) may skip this chapter. The content and structure of this chapter is based on references [18–21]. Every reader who is looking for a more detailed insight into the discussed topics may be referred to these references.

2.1 FUNDAMENTALS OF ELECTROCHEMISTRY

2.1.1 ELECTROCHEMICAL EQUILIBRIUM

The easiest way to learn about basic electrochemical principles is to look at an electrochemical (half-)cell. The simplest half-cell is a metal in a solution which contains ions of the metal species (for example Cu^{2+} in a $Cu^{2+}SO_4^{2-}$ solution; Figure 2-1a). The metal acts as an electron conductor, a so-called electrode and the solution as an ion conductor, a so-called electrolyte. Before the metal is in contact with the solution the ions in both phases have (in general different) chemical potentials:

$$\mu_i = \mu_i^0 + RT \ln(a_i) \qquad 2\text{-}1$$

with the chemical potential μ of species i, calculated by the standard potential μ_i^0, the ideal gas conctant R, the absolute temperature T and the activity a_i. The electric potential φ_i of metal ions in the metal and metal ions in the solution is equal to zero.

In the moment of contact between both phases, the chemical potentials of both phases are not at equilibrium. In such a situation, ions from the phase with higher potential pass over to the phase with lower potential according to the reaction:

$$me^{x+} + xe^- \leftrightarrow me. \qquad 2\text{-}2$$

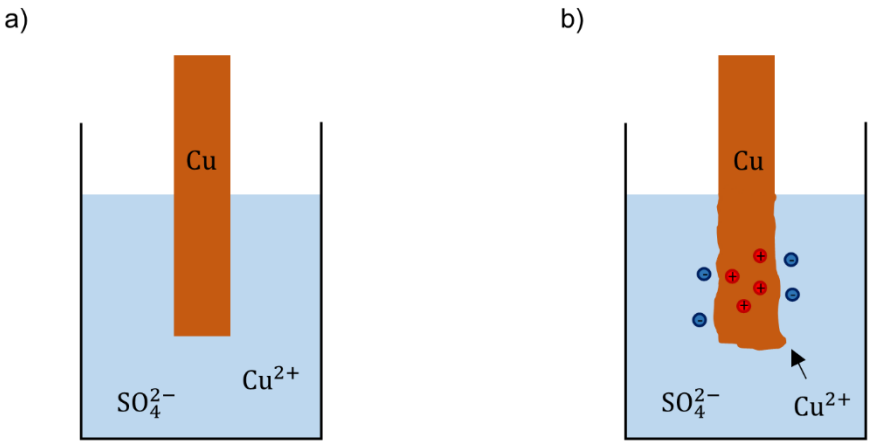

Figure 2-1: Half-cell consisting of a copper electrode and an electrolyte containing copper sulfate; a) in the moment of contact between both phases; b) after reaching electrochemical equilibrium.

Due to the ion transfer between both phases an electric potential φ builds up at each boundary layer and the metal and the solution boundary layer near the metal/solution interface are charged (Figure 2-1 b). The potential differences must be taken into account for the calculation of the equilibrium condition:

$$\mu_{\mathrm{me}^{z+}}(\mathrm{metal}) + z_i F\varphi(\mathrm{metal}) = \mu_{\mathrm{me}^{z+}}(\mathrm{solution}) + z_i F\varphi(\mathrm{solution}). \qquad 2\text{-}3$$

The expression $z_i F\varphi$ is the electrical potential energy, calculated by the charge number z, the Faraday constant F and the electrical potential of the ions in the metal/solution phase φ. This leads to the expression of the electrochemical potential:

$$\mu_i^* = \mu_i^0 + RT\ln(a_i) + z_i F\varphi, \qquad 2\text{-}4$$

The ion transfer between both phases goes on until the equilibrium of electrochemical potentials between the ions of both phases is reached: (Chapter 3 [18] and Chapter 2 [22])

$$\mu^*_{\mathrm{me}^{z+}}(\mathrm{metal}) = \mu^*_{\mathrm{me}^{z+}}(\mathrm{solution}). \qquad 2\text{-}5$$

2.1.2 Nernst Equation

The electric potential difference (or Galvani potential difference) of both phases ($\varphi_{\mathrm{me}} - \varphi_L$) can be calculated by Equation 2-5 and the definition of the electrochemical potential (Equation 2-4). Insertion of Equation 2-4 into Equation 2-5 leads to:

$$\mu^0_{\mathrm{me}} + RT\ln(a_{\mathrm{me}}) + z_i F\varphi_{\mathrm{me}} = \mu^0_{\mathrm{me}^{z+}} + RT\ln(a_{\mathrm{me}^{z+}}) + z_i F\varphi_{\mathrm{L}}\,, \qquad 2\text{-}6$$

where the subscript me refers to the metal ions inside the metal and the subscript me^{2+} refers to the metal ions in solution, which leads to the reversible potential or equilibrium potential of the cell reaction E_{rev} [19]:

$$\Delta\varphi = E_{\mathrm{rev}} = \varphi_{\mathrm{me}} - \varphi_L = \frac{\mu^0_{\mathrm{me}^{z+}} - \mu^0_{\mathrm{me}}}{zF} + \frac{RT}{zF}\ln\left(\frac{a_{\mathrm{me}^{z+}}}{a_{\mathrm{me}}}\right). \qquad 2\text{-}7$$

Considering the activity of the ions in the metal phase as $a_{\mathrm{me}} = 1$, using an abbreviation for $\frac{\mu^0_{\mathrm{me}^{z+}} - \mu^0_{\mathrm{me}}}{zF} = E_0$ and changing the potential relation from the solution to the so-called

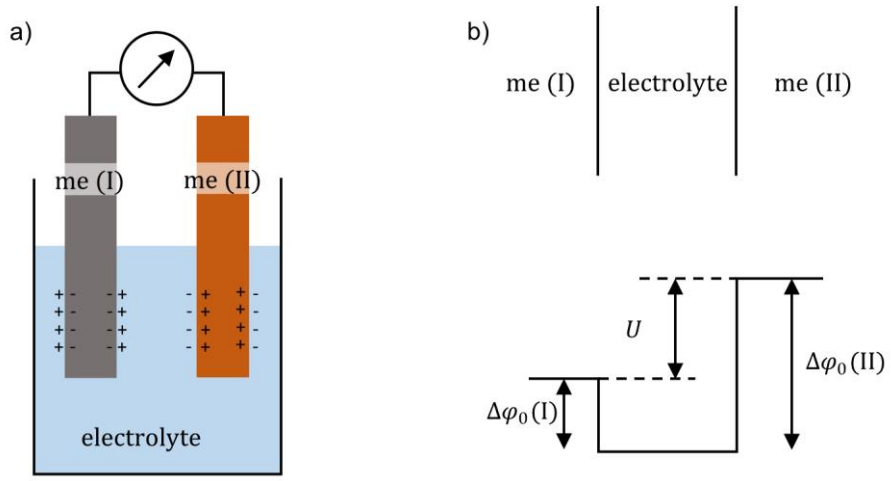

Figure 2-2: Potential distribution in electrochemical cells; a) schematic electrochemical cell; b) potential drops between electrodes and solutions.

standard hydrogen electrode (an electrode of the redox couple H^+/H_2, for which is $\varphi_0 = 0$ by definition) one gets the Nernst equation for the equilibrium potential E_{rev}:

$$E_{\mathrm{rev}} = E_0 + \frac{RT}{zF}\ln(a_{\mathrm{me}^{z+}}). \qquad 2\text{-}8$$

2.1.3 Cell Potentials

The measurement of a single Galvani potential is not possible since every measurement instrument must be in contact with both phases. At each measurement there will be a measurement instrument in contact with the solution phase and a new metal/solution interface between the instrument and the solution will appear. At this interface a new equilibrium Galvani potential at the measurement device is established. Thus, it is only possible to measure potential differences between two electrodes (Figure 2-2a). The theoretical difference of the electric potentials of metal (I) and metal (II) in solution is referred to as the cell voltage U (Figure 2-2b):

$$U = \varphi_0(I) - \varphi_0(II) = \Delta\varphi_0(I) - \Delta\varphi_0(II), \qquad 2\text{-}9$$

and can be used to calculate the electric potential of an electrochemical cell. Considering the definition of the Gibbs free energy of reaction:

$$\Delta G = \Sigma \nu_i \mu_i, \qquad 2\text{-}10$$

it is possible to calculate the standard cell potential by the standard Gibbs free energy:

$$\Delta G = -nFE_{\mathrm{rev}} \qquad 2\text{-}11$$

and if all activities are at unit activity:

$$\Delta G_0 = -nFE_0, \qquad 2\text{-}12$$

where n is the number of electrons that pass during the reaction. By combining the standard hydrogen electrode (hydrogen half-cell), which equilibrium potential at standard conditions is set to zero by definition, and a second half-cell it is possible to determine potentials of any redox couple in a half cell (Figure 2-3) (Chapter 3 [18]):

$$E_{\mathrm{rev}}^{\mathrm{Half-cell}} = E_0^{\mathrm{Half-cell}} + \frac{RT}{nF}\ln\left(\frac{a_{\mathrm{ox}}}{a_{\mathrm{red}}}\right) - E_0^{\mathrm{H.el.}} = E_0^{\mathrm{Half-cell}} + \frac{RT}{nF}\ln\left(\frac{a_{\mathrm{ox}}}{a_{\mathrm{red}}}\right). \qquad 2\text{-}13$$

2.1.4 Electrochemical Double Layer

During establishing of the electrochemical equilibrium, the boundary layer inside the metal near the metal/electrolyte interface is charged with positive or negative charges (compare Section 2.1.1). At the electrolyte side of the interface ions with opposite charge are enriched. The electrochemical double layer has formed. It is possible to increase, decrease or change the nature of the double layer by applying an external potential to the electrode and thus change the electrode charge.

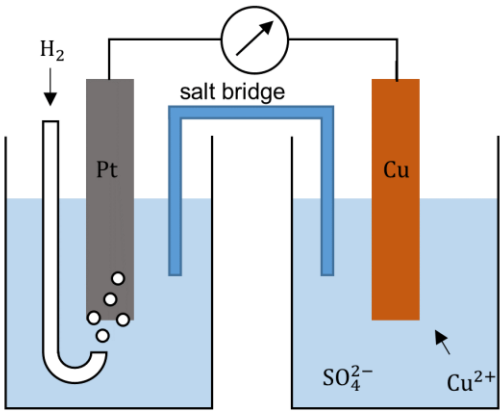

Figure 2-3: Electrochemical cell to define cell-potentials. The left half-cell is the standard hydrogen electrode which marks the potential reference point at 0 V.

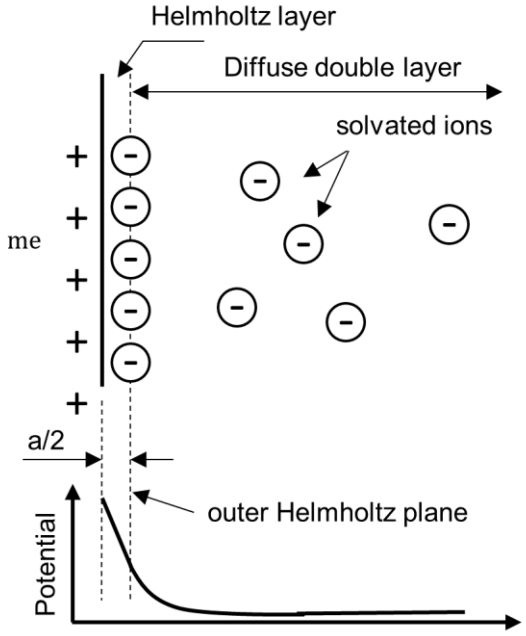

Figure 2-4: Schematic drawing of the electrochemical double layer and the resulting potential course. Negative charged solvated ions attach at the positive charged electrode and form the Helmholtz layer.

The simplest model of an electrochemical double layer is the so-called Helmholtz layer and can be compared to a plate capacity. One plate is the metal surface at which charge is enriched and at the opposite plate there are adhered ions at the electrolyte side (Figure 2-4). The charge free space between the metal surface and the outer Helmholtz plane (the center of the solvated adhered ions) has the length $a/2$, where a is the diameter of the solvated ions. A diffuse boundary layer extends into the electrolyte behind the outer Helmholtz plane.

The electrode potential decreases linearly within the Helmholtz plane and exponentially within the diffuse layer. The potential course can be calculated by the Poisson equation which is:

$$\frac{\mathrm{d}^2\varphi}{\mathrm{d}x} = -\frac{4\pi\rho}{\varepsilon} \qquad 2\text{-}14$$

for a flat electrode surface and an orthogonal x coordinate. In this case ρ is the charge density and ε the dielectric constant of the medium. (Chapter 3 [18] and Chapter 2 [23])

2.1.5 Electrochemical Kinetics

In 2.1.3 the relationship between Gibbs energy and the electrode potential was given in Equation 2-11:

$$\Delta G = -nFE_{\mathrm{rev}}. \qquad 2\text{-}11$$

This relationship also describes the possible electrical work $W_{\mathrm{E}} = -nFU$ (with U the cell voltage) that can be generated by a cell. This is based on the assumption of minimal mass transfer and minimal current ($i \to 0; U \to E_{\mathrm{rev}}$). If $U < E_{\mathrm{rev}}$ a current is flowing. At the half-cell with the lower cell potential ions are dissolving and electrons are transferred to the half-cell with the higher potential. This is called a galvanic cell.
Figure 2-5a shows a schematic drawing of a galvanic cell. In this case the two half cells $\mathrm{Zn|Zn^{2+}}(1\,\frac{\mathrm{mol}}{\mathrm{l}})$ (zinc in 1 M zinc sulfate solution) and $\mathrm{Cu|Cu^{2+}}(1\,\frac{\mathrm{mol}}{\mathrm{l}})$ (copper in 1 M copper sulfate solution) are combined. The galvanic cell can be written as:

$$\mathrm{Zn}\left|\mathrm{Zn^{2+}}\left(1\,\frac{\mathrm{mol}}{\mathrm{l}}\right)\right|\left|\mathrm{Cu^{2+}}\left(1\,\frac{\mathrm{mol}}{\mathrm{l}}\right)\right|\mathrm{Cu}. \qquad 2\text{-}15$$

Whereas the anodic cell is always written on the left-hand side. This specific galvanic cell is called the Daniell element. The potential of the zinc half-cell is -0.76 V and the potential of the copper half-cell is $+0.34$ V (considering standard conditions). Since the potential of the copper half-cell is higher (more noble) compared to the zinc half-cell, electrons are flowing from the zinc half-cell to the copper half-cell. Zinc ions dissolve into the solution and produce electrons. At the other half-cell $\mathrm{Cu^{2+}}$ ions are reduced to copper by these electrons and deposit at the copper electrode. If both half-cells are connected with an infinitely high resistance, the cell potential E can be measured as 1.1 V. If a current is flowing between both half cells the cell potential E_{rev} differs from E.

If $E_{\mathrm{rev}} > U$ an external potential forces the reaction in the opposite direction, this set up is called electrolysis cell. Figure 2-5b shows the schematic drawing of an electrolysis cell for the electrolysis of hydrochloride acid to hydrogen and chlorine. If the potential at the cathode ($\mathrm{H|H^{+}}\left(1\,\frac{\mathrm{mol}}{\mathrm{l}}\right)$) is more negative than the equilibrium potential of the cathode, $\mathrm{H^{+}}$ is reduced to $\mathrm{H_2}$. If the potential at the anodic half-cell ($\mathrm{Cl|Cl^{-}}\ \left(1\,\frac{\mathrm{mol}}{\mathrm{l}}\right)$) is more anodic (positive) than the equilibrium potential $\mathrm{Cl^{-}}$ is oxidized to $\frac{1}{2}\mathrm{Cl_2}$. The current flowing during the electrolysis depends on the external potential.

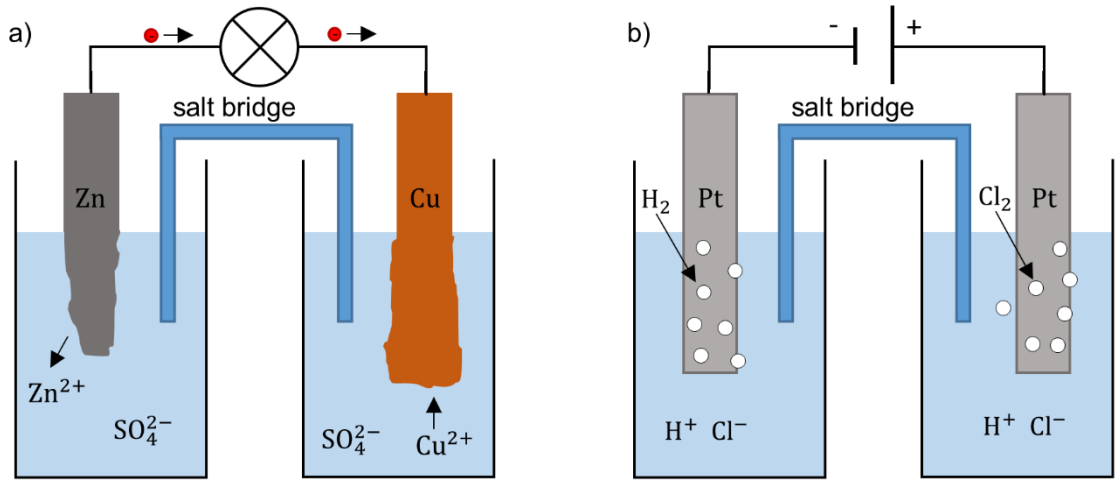

Figure 2-5: Different types of electrochemical cells; **a)** galvanic cell; **b)** electrolyse cell.

Electrochemical kinetic describes the relationship between potential and current. For the electrochemical kinetic it is important how much the electrode potential differs from the equilibrium potential at a given current. This relationship between current and potential is not linear and depends on several factors. The deviation of the cell potential from the equilibrium potential E_{rev} is called the overpotential η:

$$\eta = E - E_{\mathrm{rev}}. \qquad 2\text{-}16$$

The most common factors that affect the overpotential are diffusion limitation (diffusion overpotential; the mass transport to the electrode is a rate limiting step), reaction limitation (reaction overpotential; a reaction mechanism is rate limiting) and charge transfer limitations. First of all, the overpotential due to charge transfer at the electrode will be addressed.

Whether an electrochemical reaction occurs, depends on the difference between the potential energy of the electron in the reduced state and in the oxidized state. If the potential energy in the oxidized state is lower, oxidation occurs and vice versa.

Considering an adsorbed ion at the electrode surface. Increasing the electrode potential measured with respect to a given reference ($E = \varphi + \mathrm{const}$) from E_1 about ΔE up to a more anodic potential E_2 results in a change of energy of the oxidized state relatively to the reduced state by $nF\Delta E$ (Figure 2-6, reduced state is sketched at the same level). Furthermore, the Gibbs free energy of activation for the anodic reaction (oxidizing) $\Delta G_{\mathrm{a}}^{\#}$ is reduced by:

$$\Delta G_{\mathrm{a}}^{\#}(E_2) = \Delta G_{\mathrm{a}}^{\#}(E_1) - \alpha nF\Delta E. \qquad 2\text{-}17$$

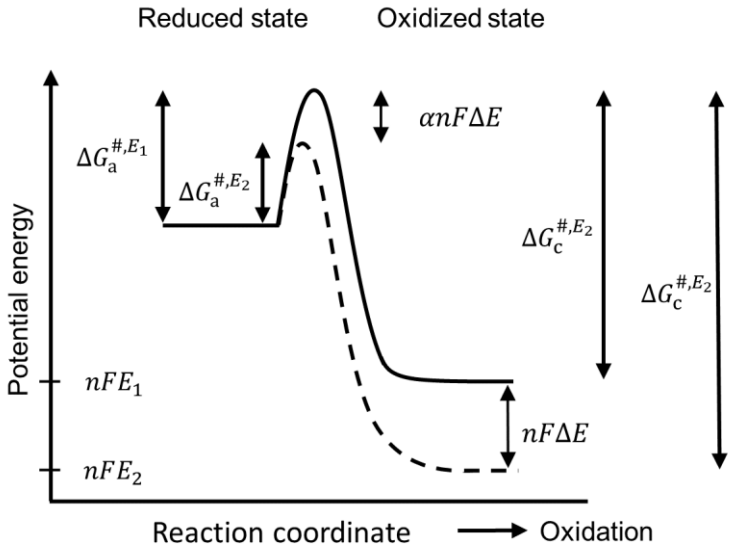

Figure 2-6: Potential energy of electrons for elementary charge transfer steps (reproduced from [20]). Change of energy due to increasing the potential from $\boldsymbol{E_1}$ to $\boldsymbol{E_2}$; The potential energy of the reduced state is sketched at the same level for simplification.

The change of activation energy with a given potential change is determined by the charge transfer coefficient α. The higher α, the lower the activation energy for the oxidation with increasing potential. Thus, increasing the potential drives the reaction anodically. In contrast to a lower activation energy for the anodic reaction with increasing potential, the activation energy for the cathodic reaction $\Delta G_c^{\#}$ increases with increasing potential [23]:

$$\Delta G_c^{\#}(E_2) = \Delta G_c^{\#}(E_1) + (1-\alpha)nF\Delta E. \qquad 2\text{-}18$$

Increasing the potential to a more positive (anodic) potential accelerates the oxidation reaction and slows down the reduction reaction. The standard rate constant k_a^0 for the anodic reaction depends on the activation energy and is given by:

$$k_a^0 = k_a^{0\prime} \exp\left(-\frac{\Delta G_a^{\#}}{RT}\right). \qquad 2\text{-}19$$

The particle flux density resulting from the anodic reaction at a given potential can be expressed as:

$$J_a(E_1) = c_{red} k_a^{0\prime} \exp\left(-\frac{\Delta G_a^{\#}(E_1)}{RT}\right), \qquad 2\text{-}20$$

and thus, the current density of the anodic reaction at E_1 can be expressed as:

$$j_{\mathrm{a}}(E_1) = nFc_{\mathrm{red}}k_{\mathrm{a}}^{0\prime}\exp\left(-\frac{E_{\mathrm{a}}(E_1)}{RT}\right), \tag{2-21}$$

whereas c_{red} is the concentration of reduced species at the electrode surface. Increasing the potential about ΔE up to E_2 results in:

$$j_{\mathrm{a}}(E_2) = nFc_{\mathrm{red}}k_{\mathrm{a}}^{0\prime}\exp\left(-\frac{\Delta G_{\mathrm{a}}^{\#}(E_1) - \alpha nF\Delta E}{RT}\right). \tag{2-22}$$

If E_1 is defined as the reference point of the experiment (e.g. the standard potential of the reference electrode) ΔE is always related to the reference point and the fixed value $\exp(-\Delta G_a^{\#}(E_1)/RT)$ can be summarized with $k_{\mathrm{a}}^{0\prime}$ to yield:

$$j_{\mathrm{a}}(E) = nFc_{\mathrm{red}}k_{\mathrm{a}}^{0}\exp\left(\frac{\alpha nF}{RT}\Delta E\right); \text{ with } k_a^0 = k_a^{0\prime}\exp\left(-\frac{\Delta G_{\mathrm{a}}^{\#}(E_1)}{RT}\right). \tag{2-23}$$

This must also be true for the equilibrium potential E_{rev}. At equilibrium potential the absolute current is zero and the absolute anodic and cathodic current are equal ($j_{\mathrm{a}}(E_{\mathrm{rev}}) = -j_{\mathrm{c}}(E_{\mathrm{rev}})$):

$$j_{\mathrm{a}}(E_0) = j_0 = nFc_{\mathrm{red}}k_{\mathrm{a}}^{0}\exp\left(\frac{\alpha nF}{RT}E_{\mathrm{rev}}\right). \tag{2-24}$$

For the cathodic current density, we receive:

$$j_{\mathrm{c}}(E_0) = -j_0 = -nFc_{\mathrm{ox}}k_{\mathrm{c}}^{0}\exp\left(-\frac{(1-\alpha)nF}{RT}E_{\mathrm{rev}}\right), \tag{2-25}$$

which is introduced as the exchange current density j_0.

Referring to Equation (2-16) ($E = E_{\mathrm{rev}} + \eta$) the definition of the overpotential of the anodic current density at a given over potential η can be expressed as:

$$j(\eta) = j_0\exp\left(\frac{\alpha nF}{RT}\eta\right), \tag{2-26}$$

whereas the cathodic current density at the same over potential η is:

$$j_{\mathrm{c}}(\eta) = -j_0\exp\left(-\frac{(1-\alpha)nF}{RT}\eta\right) \tag{2-27}$$

and the overall current density, the sum of anodic and cathodic current densities yields to:

$$j = j_0 \left(\exp\left(\frac{\alpha n F}{RT}\eta\right) - \exp\left(-\frac{(1-\alpha) n F}{RT}\eta\right)\right), \qquad 2\text{-}28$$

which is known as the Butler-Volmer equation and describes the kinetic of electrochemical reactions due to charge transfer. A similar kinetic can be found in the growth kinetic of oxide films describe by the Point Defect Model (Section 3.5). The Butler-Volmer equation is also used to determine the corrosion current during Linear Sweep Voltammetry (compare Section 2.2.3). (Chapter 4 [18] and chapter 3 [23])

2.2 Measurements Techniques

In the previous section the basics of electrochemical principles and phenomena are given. These basics are necessary to understand the measurement techniques that are used in this thesis. The statements about the influence of material treatments and microstructure on the electrochemical behavior are all (directly or indirectly) derived by observations made from electrochemical measurements.

In this section only the measurement techniques used during the research work of this thesis are presented. Numerous other measurement methods are used in the research fields of electrochemistry and corrosion science. A very detailed overview into (electrochemical) analytical methods in corrosion science can be found in [24] for example.

2.2.1 Three Electrode Cell

The basic electrochemical measurement cell is a three-electrode cell (Figure 2-7). It consists of a working electrode (WE), a counter electrode (CE), a reference electrode (RE), all three electrodes are immersed in an electrolyte and connected via a potentiostat. The working electrode is the electrode at which the investigated reactions occur. It is either an inert electrode at which redox reactions of species in the electrolyte take place or the working electrode itself is the sample and reacts at the given conditions. The second case, the working electrode itself is the sample which reacts, applies for the corrosion studies in this thesis.

A potential is applied between the counter electrode and the working electrode and the current at the working electrode is measured. The potential of the counter electrode depends on the given conditions (for example electrolyte concentration) and can change with the flowing current [25].

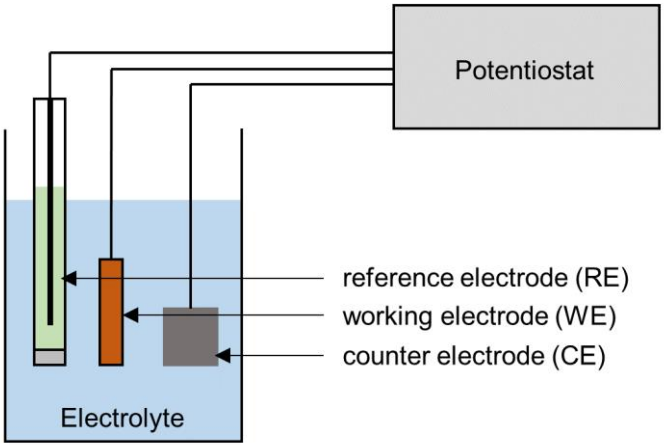

Figure 2-7: Three electrode cell.

For this reason, a third electrode is used as potential reference. The potential between the working electrode and the reference electrode is measured and if necessary, adjusted by the counter electrode. The reference electrode is usually a metal ion electrode in equilibrium with metal ions in solution, which is separated from the cell by a fritted glass. The activity of the salt anions in solution determines the equilibrium potential. Thus, it is important to ensure a constant anion activity, which can be achieved by adding an easily soluble salt of the same kind. An example for a reference electrode is a Ag/AgCl electrode in KCl solution.

2.2.2 CHRONO METHODS

During electrochemical chrono method measurements, the current or potential at the working electrode is measured over time.

2.2.2.1 Open circuit potential

The simplest measurement might be the measurement of the equilibrium potential. The sample is immersed into the electrolyte and connected to a reference electrode via a voltameter. After immersing the electrode, ions dissolve from the sample to the electrolyte or deposit at the electrode surface to establish an equilibrium (compare 2.1.1). A very high equilibrium potential can indicate a high protection against corrosion but in some cases a lower equilibrium potential can correlate with an early passivation and better corrosion protection [22]. Since electrochemical corrosion is an oxidation reaction, the potential of the material at which corrosion occurs must be higher compared to the potential at which the cathodic reaction occurs (for example another part of the material at which hydrogen is produced in case of acid corrosion). Thus, the higher the equilibrium potential of the material, the less likely the corrosion process.

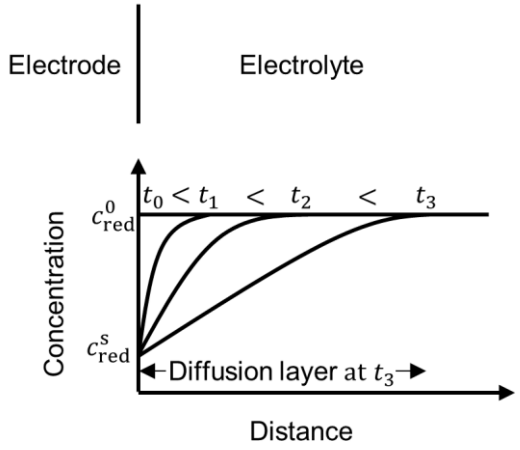

Figure 2-8: Spatial **c**oncentration profiles during oxidation at the electrode surface depending on time *t*.

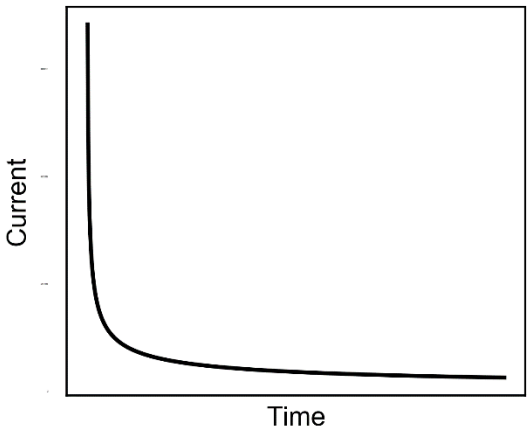

Figure 2-9: Current course resulting from mass transfer limited reactions during chrono amperometry.

2.2.2.2 Chrono amperometry

In chrono amperometry, a constant potential is applied between the sample and the counter electrode while the current is measured versus time.

Considering the redox reaction $0x + e^- \rightarrow Red$ with uninhibited charge transfer and a flat electrode in an (unstirred) electrolyte solution containing the concentration c^0_{red} of a reduced species Red and the concentration $c^0_{ox} = 0$ of the oxidized species 0x. By applying a potential E at the working electrode, a new concentration c^s_{red} will establish at the electrode surface according to the Nernst equation: $c^s_{red} = c^s_{ox} \exp\left(\frac{(E-E_{rev})nF}{RT}\right)$. With the assumption of equal diffusion coefficients for both species one yields $c^s_{ox} = c^0_{red} - c^s_{red}$ and the surface concentration of the reduced species c^s_{red}(for a reversible reaction) is:

$$c^s_{red} = \frac{c^0_{red}}{1 + \exp\left(\frac{(E - E_{rev})nF}{RT}\right)}. \qquad 2\text{-}29$$

Based on the assumption of a fast charge transfer, the rate limiting step of the ongoing reaction is the mass transport towards the electrode surface. As the reaction progresses, the concentration at the surface remains constant, but a concentration gradient spreads into the electrolyte (Figure 2-8). The flux towards the electrode j_{red} can be calculated by Ficks first law:

$$j_{red} = -D_{red}\frac{\partial c}{\partial x}, \qquad 2\text{-}30$$

and Ficks second law:

$$\frac{\partial c_{\mathrm{red}}}{\partial t} = D_{\mathrm{red}} \frac{\partial^2 c_{\mathrm{red}}}{\partial x^2}. \qquad 2\text{-}31$$

Under the given boundary conditions:

$$\begin{array}{lll} t = 0 & x \geq 0 & c_{\mathrm{red}} = c_{\mathrm{red}}^0 \\ t > 0 & x \to \infty & c_{\mathrm{red}} = c_{\mathrm{red}}^0 \\ & x = 0 & c_{\mathrm{red}} = c_{\mathrm{red}}^{\mathrm{s}} \end{array}$$

the solution of the differential equation can be found as:

$$c(x,t) = (c^0 - c^{\mathrm{s}})\mathrm{erf}\left(\frac{x}{\sqrt{4Dt}}\right). \qquad 2\text{-}32$$

The resulting current density can be expressed as:

$$j = \frac{nF\sqrt{\frac{D}{\pi}}(c^0 - c^{\mathrm{s}})}{\sqrt{t}}. \qquad 2\text{-}33$$

Equation 2-33 is known as the Cottrell equation and describes the current as a function of mass transport under the assumption of uninhibited charge transfer.

2.2.3 Linear Sweep Voltammetry

When investigating materials or solutions these can show very different electrochemical behavior depending on the applied potential. In a solution that contains several redox species, different reactions can take place at different potentials. Chain reactions can occur when a given species reacts at one potential and the product further reacts at a higher/lower potential. Or material samples can be composed from different materials that react on different potentials or form oxide layer at anodic potentials that dissolve at cathodic potentials.

In order to investigate the electrochemical behavior of a material over a potential range it is possible to apply a varying potential between the counter electrode and the sample/working electrode. Thus, it is possible to observe the current at a given potential regarding the potential history. This measurement technique is called Linear Sweep Voltammetry (LSV). The change of potential versus time is called scan rate (v [Vs^{-1}]).

A LSV measurement of a redox couple $\mathrm{Ox} + \mathrm{e}^- \rightarrow \mathrm{Red}$ is shown in Figure 2-10a. The current depends on the potential, is determined by the Butler-Volmer equation, and can possibly affected by mass transport and reaction limitations. The overall current is zero at $\eta = 0$ ($E = E_{\mathrm{eq}}$) by definition of η. The overall current is the sum of the anodic and the cathodic current,

both currents are equal at $\eta = 0$ with $j_a = -j_c \neq 0$. (Chapter 5 [18])

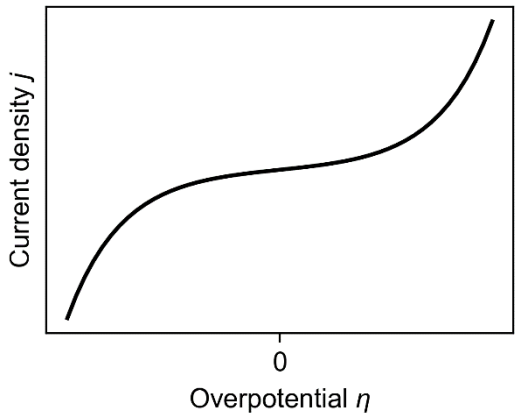

Figure 2-10: Exemplary course of a LSV measurement. The measured current is plotted over the overpotential, which is equal to the applied potential minus the equilibrium potential.

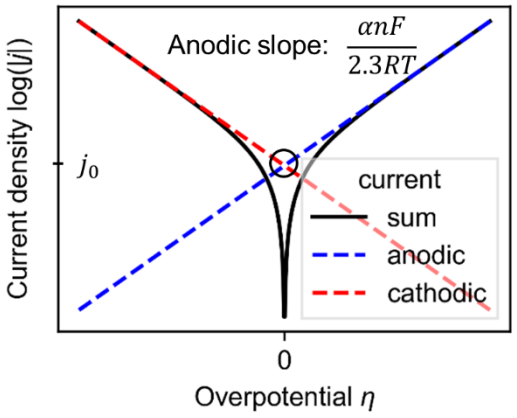

Figure 2-11: Logarithmic presentation of the absolute value of the current resulting from the LSV measurement presented in Figure 2-10.

The determination of the exchange current density (or corrosion current) j_0 can be done by LSV measurements using the Tafel method. For this purpose, the logarithm of the absolute current is plotted against the overpotential. Log of Equation 2-26 for anodic overpotentials (or Equation 2-27 for a cathodic overpotentials) yields:

$$\log(j_a) = \log(j_0) + \frac{\alpha nF}{2.3RT}\eta, \qquad 2\text{-}34$$

and

$$\log(j_c) = \log(j_0) - \frac{(1-\alpha)nF}{2.3RT}\eta. \qquad 2\text{-}35$$

The cathodic (anodic) part of the current density can be neglected if the overpotential is anodic (cathodic) enough. This way one gets a linear equation of the form $y = b + mx$. The slope of the linear part of the LSV measurement is $\alpha nF/RT$ and it is possible to determine the charge transfer coefficient. The intersection current of both partial current densities ($\eta = 0$) is the exchange current density j_0 (Figure 2-11).

LSV measurements of metals, as presented in Chapter 3, can show a different behavior. An oxide layer can form at the surface of the metal if the anodic potential is high enough to oxidize the metal. This oxide layer can slow down further reactions of the sample surface. Due to this protection, the current decreases drastically and does remain constant over a

broad potential range. This behavior is called passivity and will be discussed in Chapter 3. Linear Sweep Voltammetry only consist of a potential change in one direction. But sometimes one is interested in the forward and back reaction. For this purpose, it is possible to change the potential to one direction and at a given vortex potential change the scan direction. This way it is possible to investigate oxidation and reduction processes followed by each other. This technique is called cyclic voltammetry.

2.2.4 CYCLIC VOLTAMMETRY

Cyclic voltammetry (CV) measurements are an extension to LSV measurements. While the potential between the working electrode and the counter electrode is changed in one direction with a given scan rate in Vs^{-1} during LSV measurements, the potential is changed cyclic between two potentials (the anodic and cathodic return potentials E_a and E_c) during CV measurements (Figure 2-12).

The measured current is determined by the transport of the reacting species towards the electrode and, in the case of an additional inhibition due to charge transfer, by the Butler-Volmer kinetic. The two cases, limited by mass transfer only and limited by mass and charge transfer will be described separately.

The reaction $\mathrm{Red} \rightarrow \mathrm{0x} + n\mathrm{e}^-$ is considered as an illustration. At the beginning of the measurement the concentrations are $c_\mathrm{ox} = 0$ and $c_\mathrm{red} = c_\mathrm{red}^0$. Ficks 2nd law determines the mass transport towards the electrode:

$$\frac{\partial c_i}{\partial t} = D_i \frac{\partial^2 c_i}{\partial x^2}; i = \mathrm{red/ox.} \qquad 2\text{-}36$$

The current is determined by the flux of the reacting species:

$$j = -nFJ = nFD_\mathrm{red} \frac{\partial c_\mathrm{red}}{\partial x}. \qquad 2\text{-}37$$

The boundary conditions are given by:

$t = 0$	$x \geq 0$	$c_\mathrm{red} = c_\mathrm{red}^0$
$t > 0$	$x \rightarrow \infty$	$c_\mathrm{red} = c_\mathrm{red}^0$
$t = 0$	$x \geq 0$	$c_\mathrm{ox} = 0$
$t > 0$	$x \rightarrow \infty$	$c_\mathrm{ox} = 0$

Comparable to the amperometry measurement a potential dependent concentration will establish at the electrode surface and a concentration gradient will extend into the electrolyte during CV measurements. In contrast to amperometry, the potential is not fixed but changes with time. Thus, the surface concentration is not fix and the mass transport also depends on

potential change.

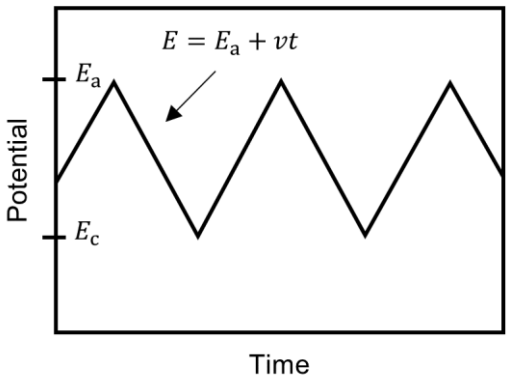

Figure 2-12: Potential course during CV experiments with multiple cycles.

2.2.4.1 Uninhibited charge transfer (only mass transfer limitation)

If the charge transfer is uninhibited the Nernst equation determines the concentration at the electrode surface. At low potentials only a very low anodic current is measurable due to the reaction $\mathrm{Red} \rightarrow \mathrm{Ox} + \mathrm{e}^-$ and the surface concentration $c_{\mathrm{red}}^{\mathrm{s}}$ remains high (Figure 2-13 point 1). If the potential further increases, the surface concentration shrinks and $\partial c/\partial x$ increases which leads to a higher mass transport (and higher current). The maximum current is reached when the concentration gradient shows its maximum (Figure 2-13 point 2). The anodic peak current for a single electron reaction is 28.5 mV higher compared to the standard potential of the redox couple. Further increase of the potential shows nearly no effect on the surface concentration but the diffusion layer growth further into the electrolyte. Thus, $\partial c/\partial x$ decreases and the current decreases as well (Figure 2-13 point 3).

Since the Nernst equation determines the concentration at the metal/electrolyte interface it can be used as an additional boundary condition:

$$\frac{c_{\mathrm{ox}}}{c_{\mathrm{red}}} = \exp\left(\frac{nF(E_r + vt - E_0)}{RT}\right), \qquad 2\text{-}38$$

where $E_{\mathrm{r}} = E_{\mathrm{c}}$ for anodic scan direction and $E_{\mathrm{r}} = E_{\mathrm{a}}$ for cathodic scan direction, v is the scan rate (compare Figure 2-12) and the t time. Applying all boundary conditions, it is possible to solve the differential equation for mass transport by diffusion. Thus, the resulting current density can be calculated as:

$$j = nF\left(\frac{nF}{RT}\right)^{\frac{1}{2}} D_{\mathrm{red}}^{\frac{1}{2}} c_{\mathrm{red}}^{0} v^{\frac{1}{2}} P[(E - E_0)n], \qquad 2\text{-}39$$

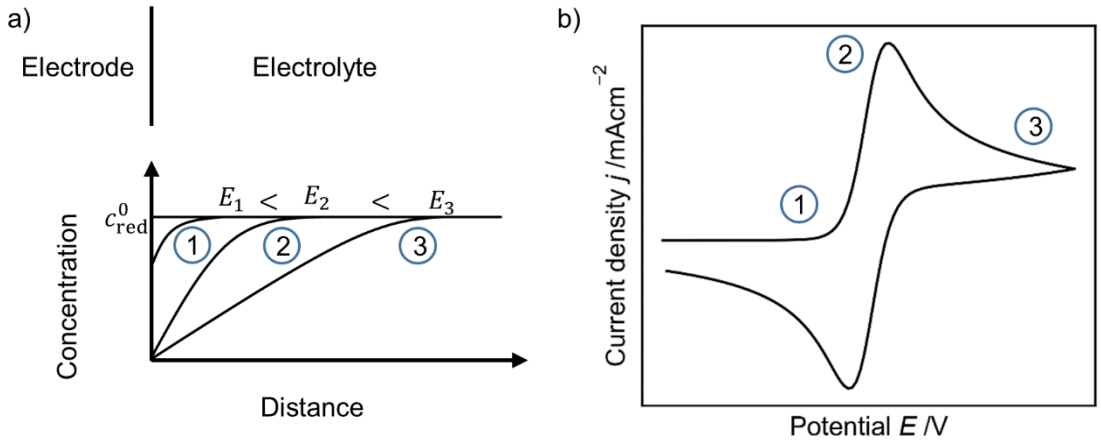

Figure 2-13: a) Spatial concentration profile during cyclic voltammetry experiments and b) resulting current density potential curve.

with the scan and redox species independent function P as the course of a current wave under the assumption of inhibited charge transfer. Derived from the expression of current density versus time, the so called Randles-Sevcik equation, which describes the maximum peak current j_p, results as:

$$j_p = 2.69 \times 10^5 n^{3/2} D_{red}^{1/2} c_{red}^0 v^{1/2}. \qquad 2\text{-}40$$

2.2.4.2 Inhibited charge transfer (charge transfer limitation)

In case of inhibited charge transfer the concentration at the electrode surface will not immediately change with respect to the Nernst equation and it cannot be used as a boundary condition at the electrode/solution interface. However, Butler-Volmer kinetics apply for electrode kinetics determined by charge transfer. For an anodic scan and thus the reaction of reduced species $Red \rightarrow Ox + e^-$, the consumption and thus the flux of the reduced species equals the reaction rate. The reaction rate for charge transfer determined oxidation is described by Equation 2-24 and the flux $J_{red} = -D_{red}\, \partial c_{red}/\partial x = j_a/(nF)$ can be expressed as:

$$D_{red} \frac{\partial c_{red}}{\partial x} = c_{red} k_a^0 \exp\left(\frac{\alpha n F}{RT}(E_r + vt)\right). \qquad 2\text{-}41$$

With this boundary condition, the diffusion equation can be solved. Finally, the mass transport leads to the current density:

$$j = \pi^{\frac{1}{2}} nF \left(-\frac{\alpha n F}{RT}\right)^{\frac{1}{2}} D_{red}^{\frac{1}{2}} c_{red}^0 Q\left(\frac{\alpha n F}{RT} vt\right), \qquad 2\text{-}42$$

whereas the function Q is similar to P, the course of the current wave for inhibited charge

transfer. If a reaction is limited by the reaction kinetics (irreversible) or the mass transfer (reversible) depends on the reaction constant and the scan rate. Fast and slow electrodes kinetics are always relative regarding the mass transport to the electrode (which depends on the scan rate).

2.2.4.3 Cyclic scan

The phenomena described above apply to a single sweep in one direction (in this above case in anodic direction). In a cyclic sweep, a distinction must also be made between reversible and irreversible reaction. In the case of a reversible reaction (fast electrode kinetics compared to mass transport) the back scan will show the same behavior as the forward scan but on a new base line and with another sign (negative current for a scan in cathodic direction) (Figure 2-14a). If the diffusion coefficient of the oxidized and the reduced species are equal ($D_{\mathrm{red}} = D_{\mathrm{ox}}$) the absolute value of the peak currents are also equal. If the reaction is not reversible (shows slow electrode kinetics compared to the mass transport), the peak potentials can differ more compared to reversible reactions (Figure 2-14b). If an electrochemical reaction during CV measurements is considered to be reversible or irreversible depends on the reaction rate, the diffusion coefficient and the scan rate. (Chapter 5 [18], chapter 3 and 4 [26])

2.2.5 Electrochemical Impedance Spectroscopy

The methods described above are all based on (slowly varying) DC potentials. In contrast, the electrochemical impedance spectroscopy (EIS) is an AC potential method. This means an AC potential is applied between the working electrode and the counter electrode. This AC potential has (usually) a fixed amplitude and a varying frequency (Figure 2-15a). Often the AC potential is overlaid by an additional DC potential. Thereby it is possible to analyze the impedance of the system at various potentials.

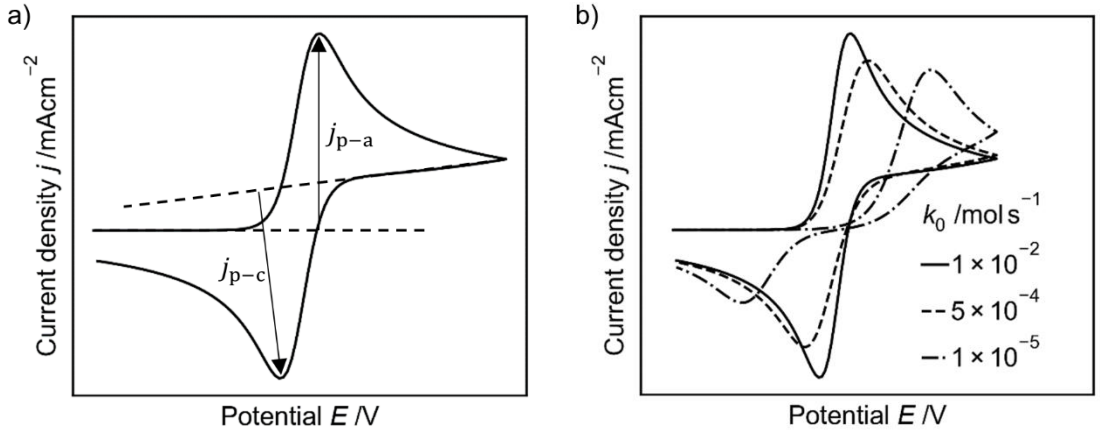

Figure 2-14: Cyclic voltammetry of a a) reversible and b) irreversible electrochemical reaction. With decreasing reaction coefficient the CV shows more irreversible behavior.

During EIS measurements the current is measured. The impedance Z of the system can be calculated as:

$$Z(\omega) = \frac{\tilde{E}(\omega)}{\tilde{j}(\omega)}, \qquad 2\text{-}43$$

Whereas a sinusoidal signal, such as the input potential and the output current, can be written as a steady state value and the magnitude of the oscillating part of the signal:

$$X(t) = \bar{X} + |\Delta X| \cos(\omega t) = \bar{X} + \mathrm{Re}\{\tilde{X} \exp(\mathrm{i}\omega t)\}, \qquad 2\text{-}44$$

with the frequency dependent complex quantities for the potential $\tilde{U}$, the current density $\tilde{j}$, and the radial frequency ω.

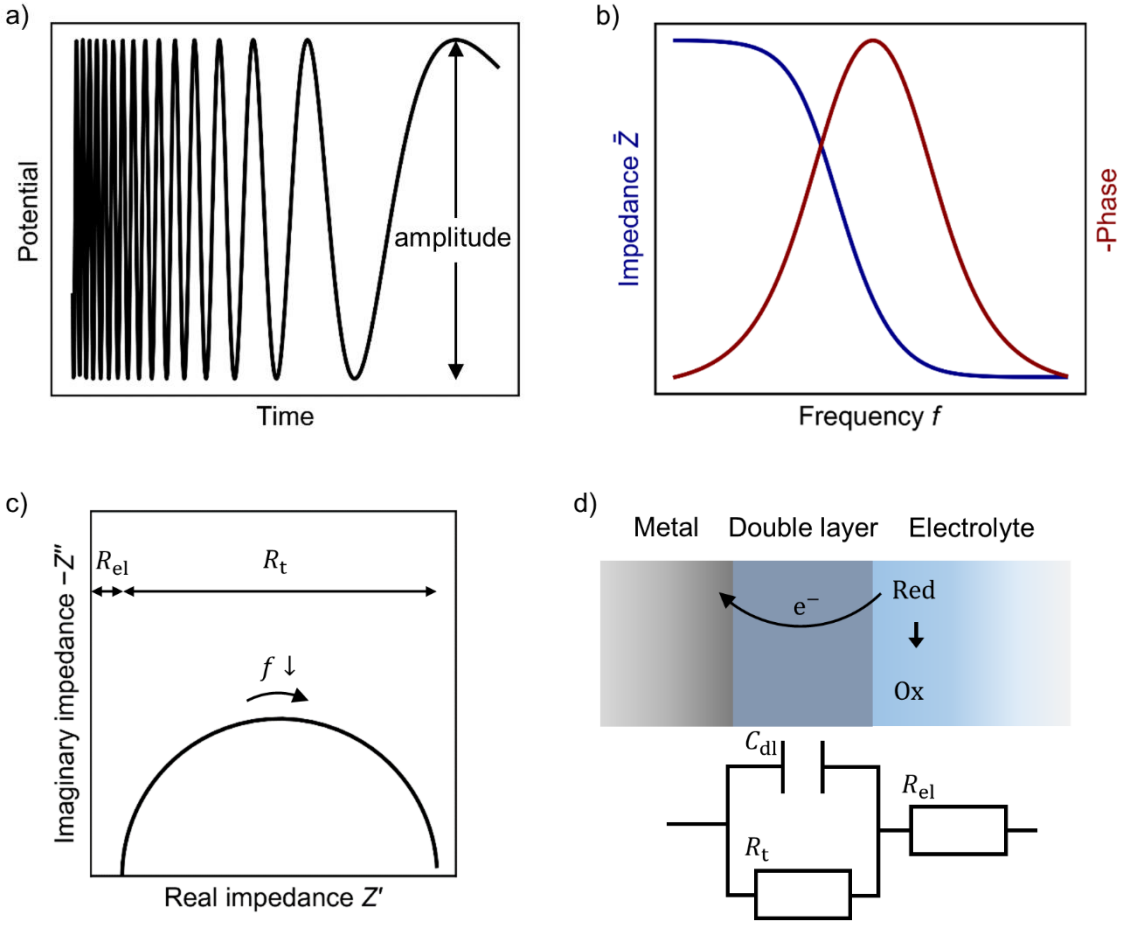

Figure 2-15: a) Frequency change over time during EIS measurements; **b)** Bode plot of impedance data obtained from a system represented in Figure 2-15d; **c)** Nyquist plot of impedance data obtained from a system represented in Figure 2-15d; **d)** electrochemical system during reduction reaction at a metal electrode surface and the representation as an EEC

The impedance is often visualized by either Bode (Figure 2-15b) or Nyquist (Figure 2-15c) plots. Bode plots are frequency-dependent plots of the phase and the absolute impedance. Nyquist plots show the imaginary part of the impedance versus the real part.

2.2.5.1 Equivalent Electrical Circuits

Analogous to electrical circuits it is possible to construct an equivalent electrical circuit (EEC) for the electrochemical system. Figure 2-15d represents an EEC for the electrochemical reaction $\mathrm{Red} \rightarrow \mathrm{0x} + \mathrm{e}^-$, which is in this case independent of mass transfer. R_{el} represents the electrolyte resistance which is necessary since the electrolyte is no perfect conductor. The electrolyte resistance can be minimized by decreasing the distance between the electrodes and/or increasing the conducting salt concentration. The second resistance in the presented EEC is the charge transfer resistance R_{ct} depending on the kinetic of the electrochemical reaction. If the reaction is more inhibited the charge transfer resistance increases.
The capacity C_{dl} represents the double layer. The double layer behaves similar to a plate capacity (compare 2.1.4) and acts as a frequency depending complex resistor. The impedance of a plate capacity can be expressed as:

$$Z_{\mathrm{cap}} = -\frac{1}{i\omega C}. \qquad 2\text{-}45$$

The impedance depends on the capacity of the layer C, the radial frequency and the imaginary number i.

The total impedance of the presented EEC can be summarized (sum of impedances in a row and sum of admittances in parallel) as:

$$Z_{\mathrm{tot}} = R_{\mathrm{el}} + \frac{R_{\mathrm{t}}}{1 + i\omega C_{\mathrm{dl}} R_{\mathrm{t}}}. \qquad 2\text{-}46$$

Often the capacitive behavior of electrochemical components (double layer, oxide layer, porous corrosion products on metal surfaces) do not behave like perfect capacities. Due to inhomogeneous surfaces and defects the capacity behavior must be adjusted [27]. The EEC component constant phase element (CPE) can represent this imperfect behavior. The impedance of a CPE is similar to a capacity:

$$Z_{\mathrm{cap}} = -\frac{1}{(i\omega)^N Q}. \qquad 2\text{-}47$$

The dimensionless parameter N determines the character of the CPE. If $N = 1$ the CPE behaves as a perfect capacity, the lower N the more the behavior differs from a capacity. If $N =$

0 the CPE behaves like a resistor and $N = -1$ like an inductivity.

A further electrical component that can also be found in EECs is the inductivity. Active dissolution by corrosion [28], surface relaxation processes of species in oxide films or the buildup of surface charges can be represented by inductivities [29,30]. The impedance of an inductivity L can be calculated as:

$$Z_{\mathrm{ind}} = i\omega L. \tag{2-48}$$

Many electrochemical reactions are (partially) determined by mass transfer. The Warburg impedance was introduced as an EEC component that can describe diffusion processes. The diffusion impedance Z_{w} of a Warburg impedance is:

$$Z_{\mathrm{w}} = \frac{\sigma}{\sqrt{\omega}} - i\frac{\sigma}{\sqrt{\omega}}, \tag{2-49}$$

σ is determined by the observed system and depends on the diffusion coefficient [27].

EECs are a powerful tool to analyze electrochemical systems. By fitting the impedance data to an EEC it is possible to obtain information about the electrochemical system and the components that affect the behavior. A DC analysis of the system represented by the EEC in Figure 2-15d would only bring information about the total real resistance:

$$\frac{\bar{E}}{\bar{J}} = R_{\mathrm{e}} + R_{\mathrm{t}}, \tag{2-50}$$

thereby both resistances are not distinguishable from each other. The analysis by an EEC leads to distinguished information about each component in an EEC. For this purpose, it is important to reduce the number of components as low as possible and to extend the frequency range as far as possible.

2.2.5.2 Kinetic models

An EEC analysis will not provide information about the actual physio-chemical processes that happen at the electrode surface. In order to describe these, it is necessary to set up a kinetic model of the electrochemical reaction system. To show the analogies between EEC analysis and kinetic models of impedance data, a kinetic impedance model for the reaction above is determined in the following section. More detailed mathematically derivation and kinetic models for more complex systems can be found in [31]. The relationship between kinetic models and EECs will be used in the following chapters during the discussion of the Point Defect Model (Chapter 3.5) and during the discussion of impedance data and kinetic modeling via the Point Defect Model (Section 6.3, 7.3 and 8.3).

The current density of a chemical reaction is a function of potential E, the educt concentration c and adsorption and surface coverage γ:

$$j_{\mathrm{F}} = f(E, c, \gamma). \tag{2-51}$$

According to Equation 2-44 the complex expression of the current density can be written as:

$$j_{\mathrm{F}} = \overline{j_{\mathrm{F}}} + \mathrm{Re}(\tilde{j}_{\mathrm{F}} \exp(i\omega t)). \tag{2-52}$$

It is possible to rewrite the complex quantity $\tilde{j}_{\mathrm{F}}$ as a Taylor series expression about the steady state value $\overline{j_{\mathrm{F}}}$ as the total derivative:

$$\tilde{j}_{\mathrm{F}} = \left(\frac{\partial f}{\partial E}\right)_{c,\gamma} \tilde{E} + \left(\frac{\partial f}{\partial c}\right)_{E,\gamma} \tilde{c} + \left(\frac{\partial f}{\partial \gamma}\right)_{E,c} \tilde{\gamma}. \tag{2-53}$$

Assuming the reaction $\mathrm{Red} \rightarrow \mathrm{Ox} + \mathrm{e}^-$ with a constant concentration c_{red} without any adsorption or surface coverage. In this reaction, the potential dependent current can be described by the Butler-Volmer equation:

$$j = j_0 \exp(bE)\,;\; b = \frac{\alpha n F}{RT}. \tag{2-54}$$

The total derivative of j is:

$$\tilde{j} = j_0 \exp(b\bar{E})\, b\tilde{E} \tag{2-55}$$

and thus we can calculate the faradaic impedance of the system as:

$$Z_{\mathrm{F}} = \frac{\tilde{E}}{\tilde{j}} = \frac{\tilde{E}}{j_0 \exp(b\bar{E})\, b\tilde{E}} = \frac{1}{j_0 \exp(b\bar{E})\, b}. \tag{2-56}$$

By adding a plate capacity and an electrolyte resistance we can achieve the same EEC as discussed in section 2.2.5.1 but the charge transfer resistance consists of kinetic parameters of the electrochemical reaction [31]:

$$Z_{\mathrm{tot}} = R_{\mathrm{el}} \frac{R_{\mathrm{t}}}{1 + i\omega C_{\mathrm{dl}} R_{\mathrm{t}}}; R_{\mathrm{t}} = \frac{1}{j_0 \exp(b\bar{E})\, b}. \tag{2-57}$$

2.3 CORROSION

Since this thesis addresses the influence of material treatment on the corrosion behavior, typical (electrochemical) corrosion phenomena are described in the following section. Usually electrochemical corrosion reactions of metals are redox reactions whereas an oxidizing agent in the environment oxidizes a metal. The oxidation of the metal and the reduction of the oxidizing agent are spatially separated but inseparably coupled. The corrosion of iron in acidic environment can proceed according to this reaction scheme:

$$\mathrm{Fe} + 2\mathrm{H}^{+} \rightarrow \mathrm{Fe}^{2+} + \mathrm{H}_2. \qquad 2\text{-}58$$

Both reactions can occur at different places of the metal, but an electron transfer between both reaction places must be ensured. The redox reaction 2-58 can be rewritten as one oxidation reaction and one reduction reaction. The oxidation of iron (the anodic reaction):

$$\mathrm{Fe} \rightarrow \mathrm{Fe}^{2+} + 2\mathrm{e}^{-} \qquad 2\text{-}59$$

and the reduction of H^{+} (the cathodic reaction):

$$\mathrm{H}^{+} + 2\mathrm{e}^{-} \rightarrow \mathrm{H}_2. \qquad 2\text{-}60$$

In order for the reactions to take place, there must be a potential difference between the two reaction places. The potential difference can arise if two different metals are connected to each other or two areas of the same material with different potential (for example through different metal phases) are connected. Furthermore, the corrosion reaction can be driven by fluctuations in the electrolyte (thermal or concentration fluctuations) which can lead to potential differences and thus to corrosion attacks at metals with the same phase. The combination of two places with different potentials leading to corrosion reactions is called corrosion element.

The metal part with the higher potential acts as the cathode and the place with the lower potential acts as the anode and is dissolved by oxidation (Figure 2-16a). An equilibrium establishes between the anode and the cathode and both partial currents are equal (compare 2.1). The more noble a metal the lower the anodic partial current at a given potential (Figure 2-16b). The same cathodic reaction leads to a lower exchange current density if the metal is more noble (Figure 2-16c). If the metals equilibrium potential is high enough it can be protected against the present form of corrosion. If corrosion occurs does not only depend on the material but on the environment as well. In a more acidic electrolyte the reduction of H^{+} is

accelerated and the equilibrium potential shifts to a more anodic potential with higher exchange current (Figure 2-16d). The exchange current of a corrosion element at equilibrium is called corrosion current j_{cor}, and the equilibrium potential of the corrosion element corrosion potential is called E_{cor}.

Corrosion current and corrosion potential can be determined by LSV measurements (compare 2.2) as the exchange current and the equilibrium potential. For the determination of both values it is import to note that depending on the scan rate of the measurements the faradaic current can be overlaid by a capacitive current due to the charging of the double layer (compare Section 2.1) [32]. [22,33]

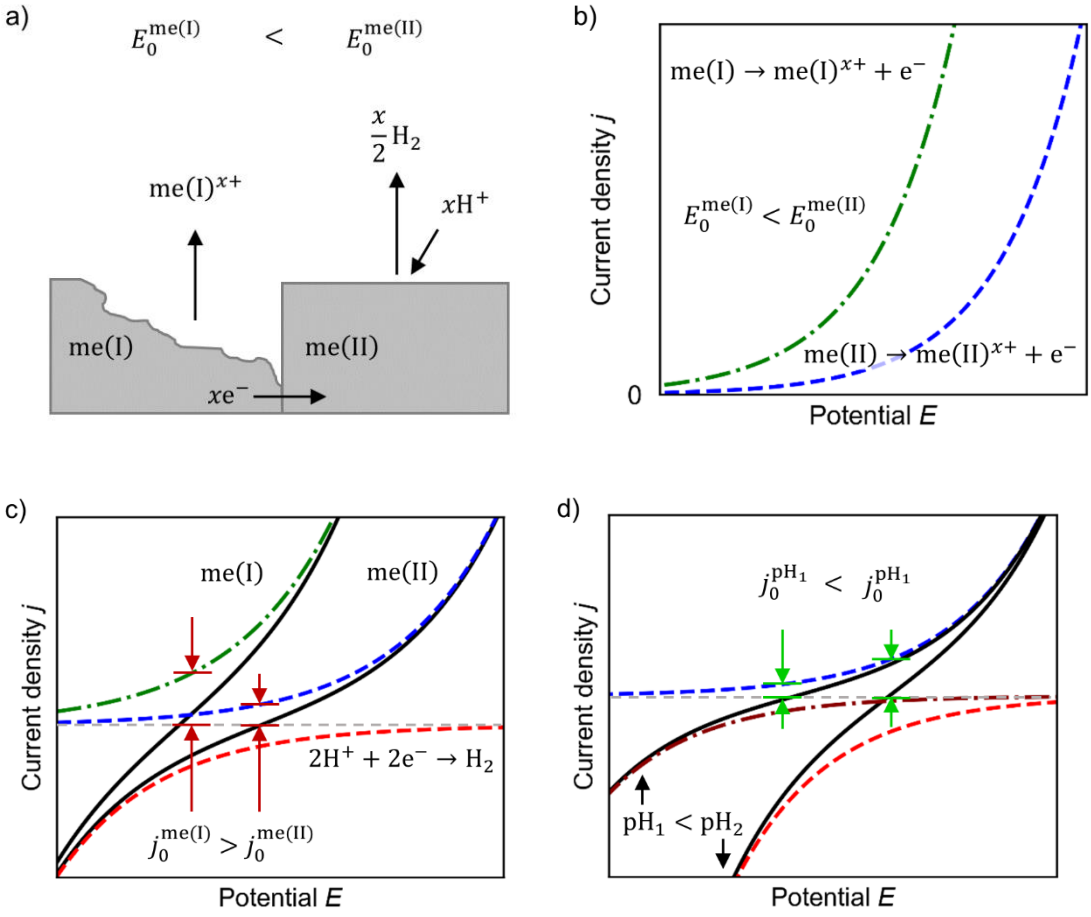

Figure 2-16: Electrochemical corrosion; a) the formation of a corrosion element, due to contact of two metals with different potentials in acidic environment, leads the dissolution of the metal with the lower potential; b) anodic current due to metal dissolution; a higher equilibrium potential (blue, dashed) leads to a lower current density at the same potential compared to a lower equilibrium potential (green, dash-dotted); c) sum current (black) and exchange current densities $\boldsymbol{j_0}$ resulting from metal dissolution in acidic environment; for a metal with a low equilibrium potential (green, dash-dotted, $\boldsymbol{j_0^{me(I)}}$) and high equilibrium potential (blue, dashed, $\boldsymbol{j_0^{me(II)}}$); d) influence of low (darkred, dash-dotted) and high (red, dashed) pH on the sum current in acidic environment.

2.3.1.1 Types of corrosion

Uniform corrosion

Uniform corrosion is the most common form of corrosion. This corrosion attack occurs evenly over the whole metal surface or large parts of the surface. It is relatively easy to detect as the attack spreads over the entire surface. During progressive attack single parts of the metal surface acts alternately as cathode and anode [22].

Galvanic corrosion

If two metals with different equilibrium potentials are in contact with each other in an aggressive environment, a corrosion element is formed. This corrosion element leads to the faster dissolution of the metal with the lower equilibrium potential and to slower dissolution of the metal with the higher equilibrium potential. This form of corrosion is called galvanic corrosion [22].

Intergranular corrosion

Intergranular corrosion appears due to depletion of chromium at the grain boundaries and is most commonly observed in acidic environment. The formation of chromium carbides at the grain boundaries (for example because of heat treatments that favor carbide growth) leads to local weakening of the passive film. The corrosion attack can start at this depletion regions and proceed along the chromium depletions at the grain boundaries. This form of corrosion can lead to corrosion cracks that result in component failure under mechanical load [33].

Crevice corrosion

Crevice corrosion can occur in small crevices due to local concentration differences due to stagnant solution in the crevice. A lower concentration of oxygen in the crevice leads to a lower potential of the cathodic partial reaction. If the potential is to low it is not sufficient for passivation and the metal surface is hold at the active state with metal dissolution (Figure 2-17) [34].

Pitting corrosion

Pitting corrosion is a localized corrosion attack that often occurs at passivated surfaces (compare Chapter 3). Pitting results in small holes at the metal surface that can grow beneath the surface and result in serious material failure. This form of corrosion is especially dangerous since it is hard to discover and even a threat for so called “stainless” steels.

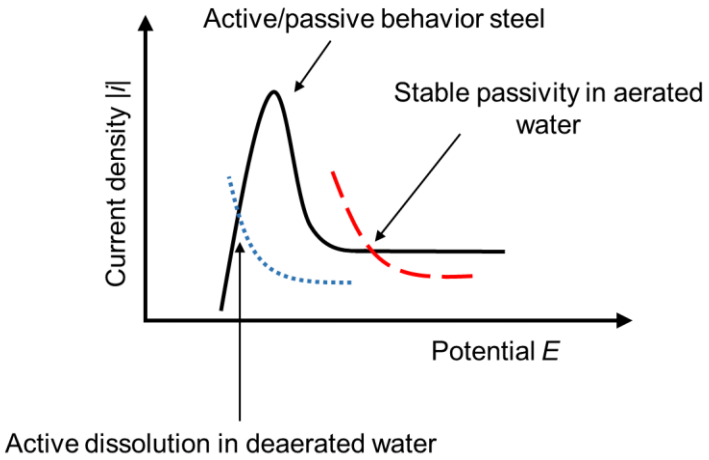

Figure 2-17: Mechanism of crevice corrosion. (—): Active/passive behavior steel; (····): Reduction of water; (– –): Reduction of oxygen. If the cathodic reaction is the reduction of water (in solution with no/a low content of oxygen, blue dotted) the potential difference between cathode and anode is too low to establish passivity of the metal anode. If the cathodic reaction is the reduction of oxygen (red dashed), the potential difference is high enough to establish passivity and the metal dissolution is slowed down. Reproduced from [34].

Pitting arises in the present of halide ions (for example Cl^- in salt water) and can occur as an autocatalytic process [35]. Three different reaction mechanism that lead to the start of pitting corrosion are discussed in literature and every mechanism can occur at given circumstances [36]: The penetration mechanism, film breakdown mechanism and the adsorption mechanism.

The penetration mechanism involves the adsorption and penetration of halides at the oxide film. Due to the high field strength the ions can penetrate the passive film and reach the metal surface. The breakdown potential is the potential at which the potential reaches the value sufficient for the halide ions to penetrate the film [37]. Impurities or defects can favor this process. According to the Point Defect Model a high number of oxygen vacancies leads to an accelerated penetration mechanism since the halide anions can bond at the defect places [38].

The film breakdown mechanism assumes microscopic breaks within the film, which give the anions the possibility to reach the metal surface. This breaks can occur due to electrostriction stress and accumulation of vacancies [36] or due to the increased number of adsorbed halide ions [39].

The adsorption mechanism is based on the enhanced transfer of metal cations, due to the formation of transient complexes, from the oxide to the electrolyte. This leads to the localized thinning of the oxide film and finally to its breakdown.

The autocatalytic pitting process starts with the formation of an aquo complex:

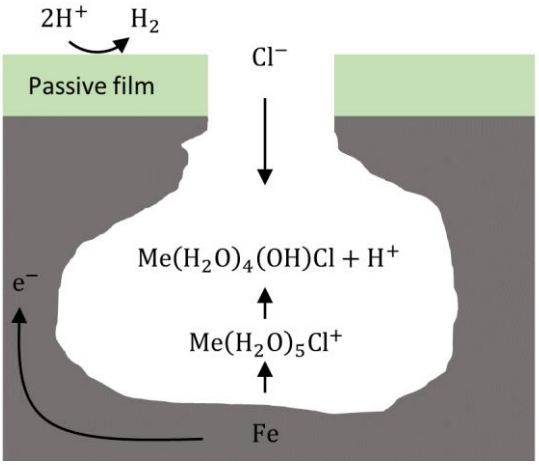

Figure 2-18: Pit form (small pit at the surface and an increasing pit beneath the metal surface) and autocatalytic mechanism; reproduced from [40].

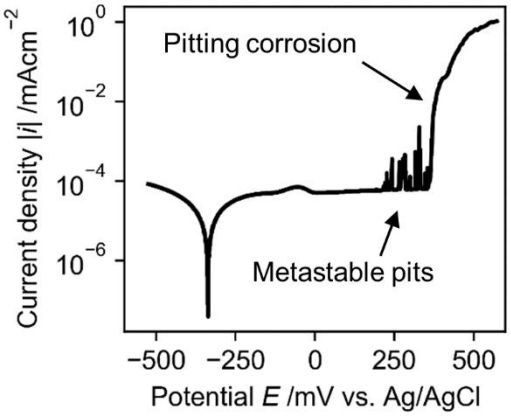

Figure 2-19: LSV measurement of stainless steel in a sodium chloride containing electrolyte.

$$Me^{2+} + 6H_2O \rightarrow Me(H_2O)_6^{2+}. \qquad 2\text{-}61$$

To balance the charge inside the pit, Cl^- ions (or other present halides) have to migrate into the pit and a chloro complex forms:

$$Me(H_2O)_6^{2+} + Cl^- \rightarrow Me(H_2O)_5Cl^+ + H_2 \leftrightarrow Me(H_2O)_4(OH)Cl + H^+. \qquad 2\text{-}62$$

The equilibrium lies usually strongly on the right hand side of the reaction [35]. The decreasing pH and the further increasing Cl^- concentration accelerate metal dissolution and hinder repassivation.

A typical LSV of stainless steel recorded in sodium chloride containing electrolyte is shown in Figure 2-19. The measurements starts with a cathodic current. After changing to an anodic current (ca. -300 mV) a clear pronounced passive region is visible. At ca. 200 mV metastable pits occur. Pitting starts but the potential is still low enough to enable repassivation of the surface. At ca. 350 mv stable pitting corrosion occurs visible by a steep increase of the current.

3

PASSIVITY[1]

Nothing is too wonderful to be true,
if it be consistent with the laws of nature.
Michael Faraday

In the previous chapter, the mechanism of corrosion due to metal oxidation was discussed. Since most metals are thermodynamically instable in contact with air or water, the oxidation of metals happens spontaneous in most environments. If these oxidation processes always resulted in aggressive corrosion attacks, the civilization as we know it would not be possible. Buildings would have to be renewed regularly, semiconductor chips would change their properties and steel constructions in the near of the sea would only outlast for a few years. Fortunately, nature has come up with a mechanism that counteracts decay through corrosion. This is due to the oxidation processes not necessarily leading to aggressive corro-

[1] Parts of this chapter have been published verbatim in *Corros. Mater. Degrad.*1 (2020) [15]

sion attacks and material failure. The oxidation products – metal oxides and metal hydroxides – can form stable layer on the surface of the metal instead of porous corrosion products or metal dissolution. This protective oxide layer can slow down further oxidation by several orders of magnitude even though they are only a few nanometers thick. A stable and protective oxide layer on the metal surface is called passive layer or passive film and the protected metal surface is called passivated [35,41].

In this chapter a short overview about the history of passivity research is given. Subsequently the chemical mechanism, thermodynamic requirements and passive film growth kinetics are presented. The second half of the chapter is about the Point Defect Model, a model of passive film growth determined by interfacial reactions and defect transport through the passive film.

3.1 History of Passivity Researches

The first works about passivity and its perception in science were carried out in the 18th century during experiments with iron in concentrated acid. The paradox behavior observed was a high reaction of iron in diluted nitric acid and a very low reaction rate in concentrated nitric acid. The first researcher who reported these phenomena was Lomonosov of Russia in 1738, followed by the German scientist Wenzel in 1782. But Keir was the first who studied this phenomena more in detail in 1790 [42]. He called the iron "altered" and he suggested the cause of the reduced activity of the iron was a change of its surface properties. He also discovered the resistance could be disrupted by scratching the iron, which underlines his statement of changed surface properties, or by touching it with fresh iron. In 1807 Hirsinger and Berzelius stated, the same altering of the iron surface could be achieved by anodic polarization of an iron electrode.

The name "passivity" for the observed phenomena appeared in correspondences between Schönbein and Faraday for the first time. Schönbein, who suggested this term, could achieve passivity of iron in different diluted acids by anodic polarization but failed in the presence of halide ions. In further experiments, Schönbein could prove that active iron in diluted HNO_3 becames passive if it is coupled in galvanic contact with Fe_3O_4 [43]. Faraday confirmed the experiments of Schönbein, invented experiments to investigate the surface film on iron, of which he believed was the reason of passivity, and could prove that it was no insulator. Faraday and Schönbein brought the phenomena of passivity to the forefront of electrochemistry at their time and were mainly responsible for the following scientific progress in this field [44].

3.2 FUNDAMENTALS OF PASSIVITY

The presence of a corroding, passivated or unaltered blank metal surface is a question of thermodynamics and kinetics. As stated before most metals are thermodynamic instable in aqueous solution. That is by their equilibrium potential being lower than the oxidation potential of the surrounding environment. By applying an external potential it is possible to adjust the potential at a metal electrode surface and thus change between inactive, active and passive state.

In Figure 3-1 a LSV measurement of a stainless steel electrode in 0.5 M sulfuric acid is shown to illustrate the phenomena of passivity. Due to the cathodic potential at the beginning of the measurement, a cathodic current is measurable and the H_2 evolution takes place at the metal surface. With increasing potential, the current changes its sign and an anodic current is measurable due to the oxidation of the metal electrode. At ca. 0.25 V, the current does not increase further but decreases sharply. The passive layer has formed and inhibits the further dissolution of the metal beneath. The range of increasing and subsequently decreasing current is called active/passive range. Following the active/passive range, the passive range begins. The current is very low and nearly constant over a broad potential range. The passive film growth with increasing potential further inside the metal. If the potential is high enough to decompose the metal oxides, the transpassive range begins. The metal dissolves and the oxygen evolution reaction can take place [35,41,45].

LSV measurements can reveal the passive nature of metals. The same measurement, as discussed with stainless steel carried out with an iron electrode shows a higher current during the active/passive area and is passivated at higher potentials, due to the worse passivation (Figure 3-2).

3.2.1 THERMODYNAMICS

The stability of metals at different pH and potential and the reaction products under the given conditions are often illustrated by Pourbaix diagrams. A Pourbaix diagram of iron in an aqueous electrolyte is presented in Figure 3-4. It presents the pH and potential conditions at which iron corrodes (orange), iron forms oxides that can passivate the surface (green) and at which iron shows immunity and does not react (grey). A LSV measurement at a constant pH can be interpreted as a vertical line through the Pourbaix diagram.

It is important to note that the Pourbaix diagram only provides information about the thermodynamics but passivity results from interaction of thermodynamics and kinetics. If an oxide film is forming at the surface of the metal is a necessary condition for passivity, but if the film is protective is a kinetic consideration and not only a question of thermodynamics [41].

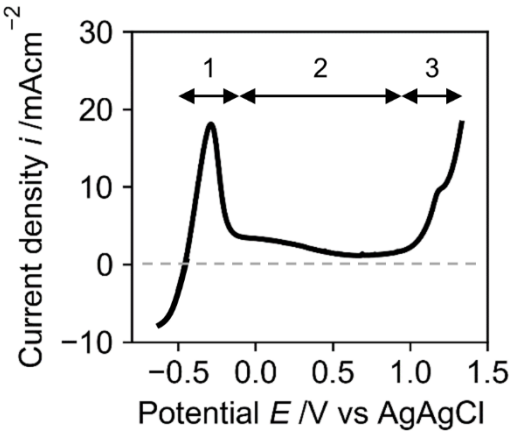

Figure 3-1: LSV measurement of stainless steel in 0.5 M sulfuric acid. 1: active/passive area; 2: passive area; 3: transpassive area.

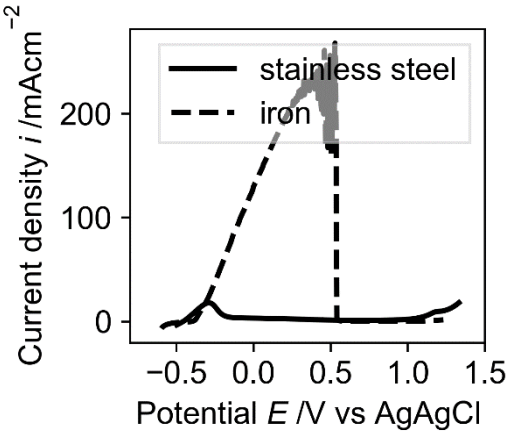

Figure 3-2: LSV measurements of stainless steel and iron in 0.5 M sulfuric acid.

Another reason why Pourbaix diagrams alone are not sufficient to predict passivity can be seen in the LSV measurement of iron in 0.5 M sulfuric acid, presented in Figure 3-2. The pH of the solution is between 0 and 1. A vertical line across the Pourbaix diagram at a pH in this range only crosses the regions of metal immunity and corrosion. But if the dissolution of iron reaches a point at which the concentration near the surface is high enough to exceed saturation, corrosion products in the form of iron sulfates deposit as porous film at the surface. Inside this porous film different pH and potential conditions can arise that favor iron oxide growth at the metal surface [46]. That is why one can observe passive behavior of iron in Figure 3-2.

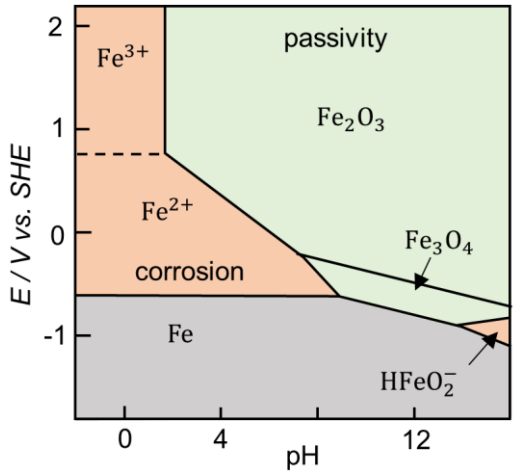

Figure 3-3: Simplified Pourbaix diagram of the iron-water system at 25 °C after [40].

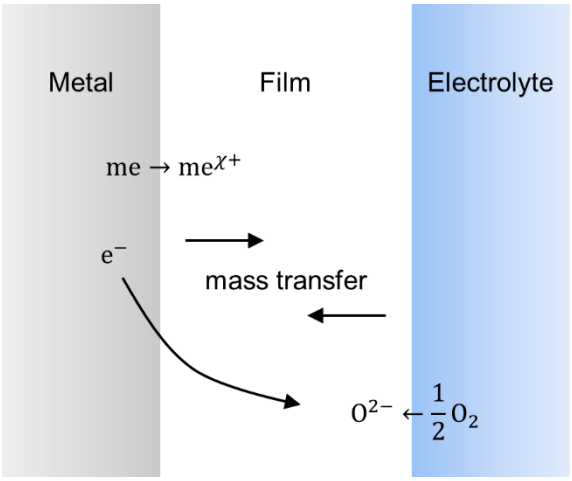

Figure 3-4: Schematic growth of an oxide film due to interfacial reactions and ion transport across the film.

3.2.2 KINETICS

A passive film is protective due to its slow growth and dissolution [45]. The growth kinetics of a passive film are determined by the reaction of metals at the metal/film interface (Figure 3-4). At the metal/film interface, the metal reacts to form metal ions and at the film/solution interface, oxygen reacts to form oxygen anions. Transport of one or both of these species through the film allows both ions to form metal oxides. Since the electrons need to be transferred through the layer, the electronic properties of the film play a significant role during film growth. The transport of charged species through the film is dictated by migration and thus can be calculated via the Nernst-Planck equation:

$$J = -D\frac{\partial c}{\partial x} + \frac{nF}{RT}E_{\mathrm{F}}c. \qquad 3\text{-}1$$

J is the flux of charged species, c the concentration of the species, D the diffusion coefficient, n the charge number and E_{F} is the electric field strength. Different film growth models will be discussed in section 3.4. The models differ in terms of the rate determining step. Either the transport of ions through the film, the reaction at the metal/film interface or the reaction at the film/solution interface are predicted to be the rate determining step [35]. Despite the differences most models can be approximated by an inverse logarithmic growth law:

$$\frac{1}{L} = A - B\log(t), \qquad 3\text{-}2$$

which describes the oxide film thickness L as a function of time t and model specific constants A and B.

Over the past few years, one model in particular has become increasingly popular, the so-called Point Defect Model (PDM). The PDM describes oxide growth by interfacial reactions, transport of point defects through the film, and is the basis for much further work in the fields of passivity. The PDM is described in detail in Section 3.5.

3.3 PASSIVE FILM PROPERTIES ON CARBON STEEL

In this thesis, the corrosion and passive film properties of different types of carbon steel are studied. Both corrosion and passive film properties are closely related because passivity determines the corrosion, and the properties of the passive film itself determine its stability and protective effect. Thus, knowledge about the passive film properties provides knowledge about the corrosion behavior.

The corrosion behavior of steel alloys depends strongly on the alloying elements. Especially chromium shows an important role in terms of protectiveness of the passive film. Iron-chromium alloys with a Cr content below 10 % show similar active/passive behavior to iron, while iron-chromium alloys with a Cr content above 15 % show active/passive behavior similar to chromium. Chromium oxides are significantly more stable and thus form a more protective passive film [47]. The content of chromium is the criterion to distinguish between steel and stainless steel.

In order to predict passivity of iron chromium alloys, the percolation model has been developed. In this model, a simple atomic lattice is considered where each atom has eight neighbors. If 1/8 (12.5 %) of all atoms are chromium, at least 50 % of the Cr atoms have at least one Cr atom as neighbor [48]. Thus, a protective network of chromium can be formed throughout the steel. An iron-chromium composition with at least 12.5 % chromium is-called stainless steel. In 1990 Newman *et al.* could confirm this assumption by Monte Carlo simulations. They could show an onset of passivity by percolation at 12 % and full passivity at 17 % chromium [49,50].

3.3.1 Composition

As mentioned before, the passive film consists of metal oxides and hydroxides. The passive film on iron-chromium alloys with very low content of alloying elements (next to iron and carbon) is similar to the passive film on pure iron. The film on stainless steels with a high amount of chromium differs significantly to those.

3.3.1.1 Iron

Since the first experiments regarding passivity were performed with iron the composition of the surface layer has been discussed for a long time. However, extensive studies on the composition of the passive film on iron have been performed since the early 1960s. It has often been concluded to be a bilayer passive film with either Fe_3O_4 or $\gamma - Fe_2O_3$ as the inner layer and a mix of iron oxides/hydroxides or $\gamma - Fe_2O_3$ as the outer layer [51].

In 2010, using surface enhanced Raman spectroscopy Herrington *et al.* could prove the passive film being a bilayer film consisting of an inner layer of Fe_3O_4 or $\gamma - Fe_2O_3$ and an outer layer composed of Fe(III) oxide/hydroxide [52].

3.3.1.2 Stainless Steel

A bilayer structure can also be found in stainless steel passive films. The composition of these passive films on stainless steel is determined by the alloy composition. Based on the assumption of high dissolution of iron and iron oxides (and some other alloying elements) and the slow dissolution of chromium and its oxides, one can assume that the composition

of oxides in the passive films are not equal to the element distribution in the metal. Indeed the inner resistive passive films on stainless steel are highly enriched with chromium (mainly Cr(III) in $Cr(OH)_3$ and Cr_2O_3) compared to the bulk material. The inner layer further consists of a smaller part of FeOOH and Fe_2O_3. These species (FeOOH and Fe_2O_3) are enriched in the outer layer while the contents of chromium species are very low in the outer layer [53].

The distribution of Cr and Fe oxides/hydroxides shows how the role of the different layers differ. The inner layer clearly shows a higher protection due to the chromium oxide enrichments.

3.3.2 Electronic Properties

Oxide films on iron and iron-chromium alloys show semiconductor behavior [35]. The barrier layer of a passive film can be seen as a highly defective semiconductor in which the defects (vacancies and interstitials) act as the electronic dopants [54]. The nature of the defects determines the electronic properties of the passive film. A film with mainly oxygen vacancies and metal interstitials shows the behavior of an n-type doped semiconductor while an oxide film with mainly metal vacancies shows the behavior of a p-type doped semiconductor.

The study of the electronic nature of passive films is often done via Mott-Schottky analysis. The capacity of the passive film (more precisely: the capacity of the space charge region C_{sc} of the passive film) at different potentials is measured during Mott-Schottky analysis. The value $1/C_{sc}^2$ is plotted versus the potential. The electronic type of the passive film is visible from the slope of $1/C_{sc}^2$. A positive slope means n-type behavior while a negative slope indicates p-type behavior.

For a linear dependency of $1/C_{sc}$ and the applied voltage E the defect density N_D and the flat band potential E_{fb} can be calculated by the Mott-Schottky equation

$$\frac{1}{C_{cs}^2} = \frac{2}{\varepsilon\varepsilon_0 e N_D}\left(E - E_{fb} - \frac{kT}{e}\right), \qquad 3\text{-}3$$

in which ε describes the permittivity of the oxide (that can be assumed as 12 for oxide layers on stainless steel [55]), ε_0 the permittivity of the vacuum (8.85×10^{-12} C/(Vm)), e the elementary charge of an electron (1.902×10^{-19} C), E_{fb} the flatband potential, i.e. the potential at which no band bending occurs in the electrolyte and the redox potential equals the Fermi potential, k the Boltzmann constant (1.38×10^{-23} J/K), T the temperature, and N_D describes the concentration of dopants. The capacity of the double layer remains nearly constant during the Mott-Schottky analysis and can be neglected [56].

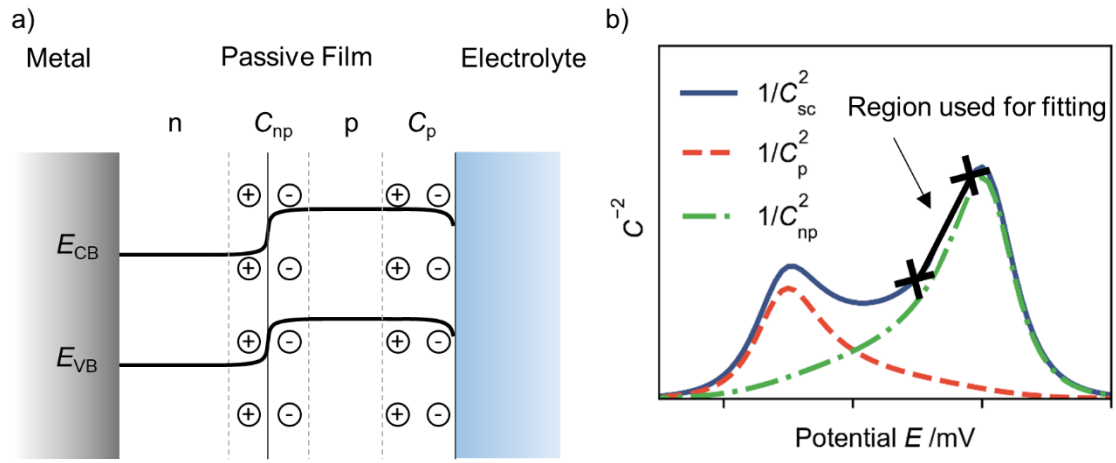

Figure 3-5: a) Electronic structure of bipolar passive film with n-type inner layer and p-type outer layer on a metal surface in contact with an electrolyte b) sketch of the space charge capacity as the sum of the capacity of the np-junction and the p-type layer; the passive region used for fitting is marked.

Since many metal oxides form bipolar films, with either an inner n-type and an outer p-type layer separated by a np-junction (Figure 3-5a) or an inner p-type layer and an outer n-type layer separated by a pn-junction, the Mott-Schottky plots of those bipolar passive films show superpositions of the capacities of the junction and the outer layer (Figure 3-5b) [57].

As stated above, the passive film on carbon steel shows bilayer structure. Mott-Schottky plots of passive films on stainless steel reveal this structure by a more complex slope of $1/C_{sc}^2$. The space charge capacity of such an oxide film can be interpreted as a series connection of the space charge capacity of the outer layer and the space charge capacity of the junction. In the case of an outer p-type layer and an inner n-type layer one yields:

$$\frac{1}{C_{sc}} = \frac{1}{C_p} + \frac{1}{C_{np}} \qquad 3\text{-}4$$

Jiang *et al.* developed a nonlinear fitting method for this type of Mott-Schottky plots and could prove the passive film on stainless steel as a combination of an inner n-type layer and an outer p-type layer [57]. For the purpose of this thesis, the potential range of MS-analysis is restricted to the passive range. In this range $1/C_{sc}^2$ shows nearly linear behavior.

3.4 Film Growth Models

Not only are the properties of passive films under intensive investigation, but the kinetics of oxide film growth as well. One of the earliest models for oxide film growth on metals was given by Cabrera and Mott in 1948 [58]. The model describes oxide film growth by transport

of metal cations through the film and by the reaction of those cations at the film electrolyte interface. A few years later, in 1964, Sato and Cohen explained the passive film growth on iron in neutral electrolyte by a place-exchange mechanism of oxygen and metal. A layer of oxygen adsorbs at the metal surface and changes places with the underlying metal. If the metal ions form the top layer, an additional layer of oxygen adsorbs and the procedure repeats [59]. In 1970 Fehlner and Mott adapted the Cabrera and Mott model but made the assumption that the film growth is controlled by the transport of anions through the oxide film, and the rate limiting step is the emission of anions to the oxide film. The activation energy of this step increases linearly with film thickness [60]. This approach assumes the electric field strength grows with increasing applied potential while the growth is limited by the high field ion conductivity through the oxide. Battaglia and Newman predicted a similar mechanism. They presented a model consisting of electrochemical reactions and transport mechanisms based on the assumption of high electric fields inside the passive film. The electric field strength inside the film should depend on the applied potential and increase with increase of external potential. It then decreases with growth of the oxide film (Figure 3-6). Kinetic models based on these assumptions can be summarized as high field models (HFM).

In 1981, Chao and Macdonald published the first version of the Point Defect Model. In its first form, the Point Defect Model describes the oxide film growth by transport of anion vacancies through the film [61]. The PDM is steadily developed and a set of interfacial reactions for film growth, formation of interstitials and vacancies as well as film dissolution were added. The rate limiting step for film growth is the formation of anion vacancies at the metal/oxide interface, which is driven by the potential drop at this interface [62]. The film growth is limited by interfacial potentials which grow with increasing applied potential, and the electric field strength is assumed to be independent from the applied potential (Figure 3-6). These types of models are summarized as the interfacial models (IFM). In 2002 Olsson et al. could show, by a combination of electrochemical quartz crystal micro balance (EQCM) and electrochemical measurements, that oxide growth on stainless steel follows the kinetics described by IFM rather than HFM [63].

The PDM has led to several models and further work based on it. In 2001, Krishnamurthy et al. published a time dependence model based on the PDM, which also describes the film growth, by a set of interfacial reactions. The rate limiting step is the transport of cation vacancies through the film and the reaction of these vacancies at the metal/film interface [64]. In 2006, Venkeerberghen used finite element simulations for modeling of the oxide growth. He followed the PDM assumptions but calculated the field strength via the Poisson equation [65]. The research group of Phillipe Marcus published a generalized growth model (GGM) for the growth of oxides on metals in 2013. The model is taking into account the metal/alloy compositions and the variation of electric field during oxide film growth [66,67]. Modeling of corrosion processes based on the PDM could also be successfully done [68,69].

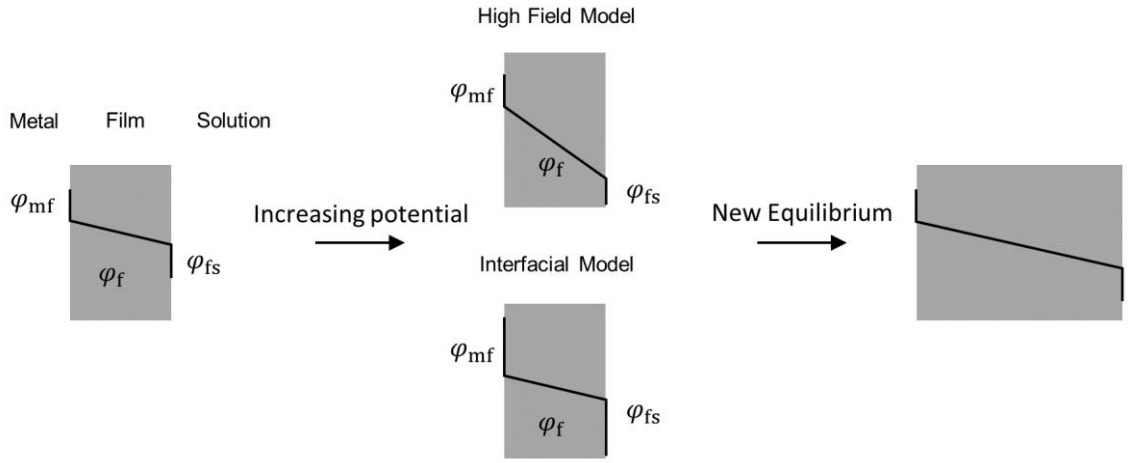

Figure 3-6: Schematic potential change due to applied external passivation potential for high field models and interfacial models; $\boldsymbol{\varphi_{mf}}$: Potential drop at metal/film interface, $\boldsymbol{\varphi_f}$: Potential drop over the film, $\boldsymbol{\varphi_{fs}}$: Potential drop at the film/solution interface; An external potential leads to increased field strength inside the passive film in case of the high field model or to increased potential drops at the interfaces in case of the interfacial models. After establishing a new steady state with increasing film thickness, the interfacial potentials are equal to the first equilibrium with a lower external passive potential. Reproduced from [62].

3.5 The Point Defect Model

The Point Defect Model (PDM) describes oxide film growth by a set of interfacial reactions and transport of defects, namely oxygen vacancies, metal vacancies and metal interstitials, which lead to the growth and decomposition of the passive layer. Chao et. al developed the PDM in the early 1980s in Macdonalds work group at Ohio State University [70]. The original PDM was the first model that took the potential drops at the metal film interfaces into consideration. The potential drops are assumed to be functions of the external potential V_{ext} and the pH of the solution. The defect transport can be described by diffusion and migration via the Nernst-Planck equation. Since the beginnings in the early 1980s, work on the model has been ongoing and Macdonald et al. extended the model by consideration of interfacial reactions which lead to film growth and dissolution [2].

In the present work, the PDM II is used to describe the film growth and vacancies of the barrier layer. It is assumed that only the barrier layer contributes significantly to the corrosion resistance [62]. The PDM III is developed for metals with a bi-layer passive film, at which the outer layer contributes significantly to the corrosion resistance [71]. This is the case with aluminum, for example, where the outer porous layer can be in the range of micrometers [72].

3.5.1 PDM Reaction Scheme

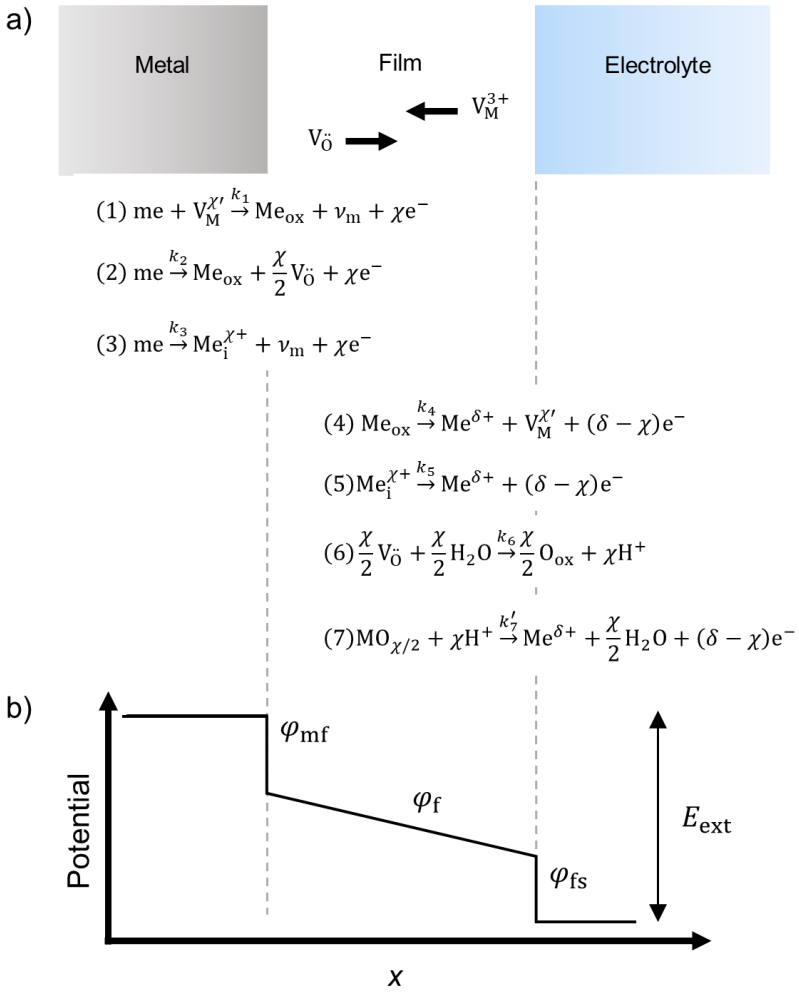

Figure 3-7: (a) Reaction mechanism at the metal–film and film-solution interface; at the metal–film interface the following reactions occur: the consumption of cation vacancies by metal atoms from the metal (Reaction 1); the formation of metal ions and oxygen vacancies inside the passive layer (Reaction 2); the formation of metal interstitials (Reaction 3); at the film-solution interface, the following reactions occur: Dissolution of metal ions from the passive layer and generation of cation vacancies (Reaction 4); metal interstitials inside the passive layer react to metal ions and dissolve to the electrolyte (Reaction 5); oxygen vacancies react with water to form oxide ions in the passive film (Reaction 6) and the dissolution of the oxide film to metal ions in the electrolyte (Reaction 7). Following the Kröger–Vink notation: me: Metal atoms inside the metal, Me_{ox}: Metal ions inside the oxide, $V_{\ddot{O}}$: Oxygen vacancies (two positive charges indicated by two dots),$V_M^{\chi+}$: metal vacancies, 0_{ox}: Oxygen ions inside the oxide;χ and δ are the charge numbers of the metal in the oxide and in solution, repectively **(b)** Electrostatic potential as a function of distance from the metal surface. Potential drop at the interfaces: φ_{mf}: potential drop at the metal–film interface; φ_f: potential drop inside the passive layer; φ_{fs}: potential drop at the film/solution interface; E_{ext}: external potential.

According to the PDM, interfacial reactions and the transport of vacancies determine the passive film growth (Figure 3-7a). The reaction rate of each electrochemical reaction depends on the potential drop at the interface at which the reaction is taking place. The potential drop over the passive film determines the transport of the vacancies (Figure 3-7b).

The reactions at the metal/film interface are the consumption of metal vacancies to form metal ions in the oxide and metal vacancies in the metal (Reaction 1), the formation of metal ions in the oxide and oxygen vacancies (Reaction 2) and the formation of metal interstitials in the film and metal vacancies in the metal (Reaction 3).

The reactions at the film/solution (outer-layer) interface are the dissolution of metals ions from the oxide to the solution and thus the formation of metal vacancies in the film (Reaction 4), the dissolution of metal interstitials to the solution (Reaction 5), the consumption of oxygen vacancies to oxygen in the oxide place of the film (reaction 6) and the dissolution of the oxide film by H^+ ions (Reaction 7). All reactions are assumed to be irreversible.

The rate constant of the electrochemical reactions can be written as a function of the corresponding interfacial potential drop:

$$k_i = k_i^{0\prime} \exp\left(\frac{\alpha_i \chi F}{RT} \varphi_{\mathrm{mf}}\right), i = 1,2,3 \qquad 3\text{-}5$$

$$k_i = k_i^{0\prime} \exp\left(\frac{\alpha_i (\delta - \chi) F}{RT} \varphi_{\mathrm{fs}}\right), i = 4,5 \qquad 3\text{-}6$$

$$k_7 = k_7^{0} \exp\left(\frac{a_7 (\delta - \chi) F}{RT} \varphi_{\mathrm{fs}}\right) c_{\mathrm{H}^+}^{m}, \qquad 3\text{-}7$$

with the reaction order of the film dissolution m, the charge transfer α_i and the base rate constant $k_i^{0\prime}$. The potential drop at the film/solution interface φ_{fs} is assumed to be a linear function of external potential E_{ext} and pH [73]:

$$\varphi_{\mathrm{fs}} = \alpha E_{\mathrm{ext}} + \beta \mathrm{pH} + \varphi_{\mathrm{fs}}^{0}, \qquad 3\text{-}8$$

whereas α is a constant describing the polarizability of the film/solution interface and β is describing the depend of the film/solution potential drop to pH. The potential drop at the metal/film interface can be (according to Equation 3-8) written as:

$$\varphi_{\mathrm{mf}} = E_{\mathrm{ext}} - \varphi_{\mathrm{f}} - \varphi_{\mathrm{fs}} = (1 - \alpha) E_{\mathrm{ext}} - E_{\mathrm{F}} L - \beta \mathrm{pH} - \varphi_{\mathrm{fs}}^{0}, \qquad 3\text{-}9$$

with the electric field strength E_{f} inside the film, the film thickness L and thus the relation for the potential drop across the film $\varphi_{\mathrm{f}} = E_{\mathrm{F}} L$. Following Equations 3-8 and Equation 3-9, the rate constant of the electrochemical reactions can be written as:

$$k_i = k_i^{0\prime} \exp\left(\frac{\alpha_i \chi F}{RT}\left((1-\alpha)E_{\text{ext}} - E_{\text{F}}L - \beta\text{pH} - \varphi_{fs}^0\right)\right), i = 1,2,3 \quad 3\text{-}10$$

$$k_i = k_i^0 \exp\left(\frac{\alpha_i(\delta-\chi)F}{RT}(\alpha E_{\text{ext}} + \beta\text{pH} + \varphi_{\text{fs}}^0)\right), i = 4,5 \quad 3\text{-}11$$

$$k_7 = k_7^0 \exp\left(\frac{\alpha_7(\delta-\chi)F}{RT}(\alpha E_{\text{ext}} + \beta\text{pH} + \varphi_{\text{fs}}^0)\right) c_{\text{H}^+}. \quad 3\text{-}12$$

As can be seen, the reaction rates of Reaction 1, 2 and 3 depend on the film thickness and the reaction rates decrease with ongoing film formation. On the other hand, Reaction 4, 5, 6 and 7 are independent of film thickness L and the reaction rates are constant during film growth (considering a constant pH and a constant external potential E_{ext}).

To study the growth and dissolution of the passive film it is necessary to separate the reactions regarding their impact on the boundary positions of the film (metal/film interface and film/solution interface). Reactions that do not affect the position of the boundary are called lattice conservative. This is the case for Reaction 1, 3, 4, 5 and 6. Whereas reactions that move the boundary are called nonconservative [62]. Reaction 2 describes the growth of the passive film inside the metal. With ongoing reaction, the metal/film interface moves in the direction of the metal, thus Reaction 2 is a nonconservative reaction. Reaction 7 describes the dissolution of the film. The film dissolution moves the film/solution boundary and is therefore a nonconservative reaction. The rate of change of the passive film thickness $\mathrm{d}L/\mathrm{d}t$ can be expressed by the nonconservative reactions:

$$\frac{\mathrm{d}L}{\mathrm{d}t} = \Omega(k_2 - k_7) = \Omega\left(k_2^0 \exp\left(\frac{\alpha_2 \chi F}{RT}((1-\alpha)E_{ext} - E_F L - \beta pH)\right) - k_7\right). \quad 3\text{-}13$$

The concentrations at the interfaces result from the steady state conditions:

$$\bar{c}_{\text{I}}^0 = \frac{k_3}{k_5} \quad 3\text{-}14$$

$$\bar{c}_{\text{M}}^L = \frac{k_4}{k_1} \quad 3\text{-}15$$

$$\bar{c}_{\text{O}}^0 = \frac{k_2}{k_6}. \quad 3\text{-}16$$

The bar $\bar{c}$ marks steady state values, the indices are I: interstitials, M: metal vacancies, O: oxygen vacancies, whereas the indices L and 0 mark the metal/film interface and the film/solution interface, respectively.

3.5.2 IMPEDANCE MODEL

In the following section, I will give an overview about the derivation of the impedance model resulting from the complete PDM. I will follow the derivation given by Macdonald and coworkers in different publications [74,75] sometimes with slightly different names, order and additional information which, in my opinion, make it more comprehensible.

For the purpose of this thesis, a reduced model is being used, and it is not necessary to follow the complete derivation. The discussion of the reduced model is given in Chapter 4 and for the understanding of this thesis, it is sufficient to jump to this chapter. If you want to follow the entire derivation, be it out of interest or out of the desire to work with a more comprehensive model, it is handy to keep the following quote in mind: *"Wir schaffen das."* (Angela Merkel, Acting Chancellor Germany, 2016).

The impedance model for passive film growth by the interfacial reactions and vacancies transport described by the PDM can be derived by the current flowing according to the model. The complex quantity of a current can be written as (compare 2.2.5.2):

$$\tilde{j}_{\mathrm{F}} = \sum \left(\frac{\partial f(x_i)}{\partial x_i}\right)_{x_j, j\neq i} \widetilde{x_i}. \qquad 3\text{-}17$$

The current, due to the electrochemical reactions at the metal/film and metal/solution interface, can be written as the sum of the current densities of reactions 1, 2, 3, 4, 5 and 7:

$$j_{\mathrm{PDM}} = \chi F(c_{\mathrm{M}} k_1 + k_2 + k_3) + (\delta - \chi) F(k_4 + c_{\mathrm{I}} k_5 + k_7). \qquad 3\text{-}18$$

The complex conjugate (described by the Taylor expansion) of the current density is:

$$\tilde{j}_{\mathrm{PDM}} = j_{\mathrm{E}} \tilde{E} + j_L \tilde{L} + j_{c\mathrm{M}} \widetilde{c_{\mathrm{M}}} + j_{c\mathrm{I}} \widetilde{c_{\mathrm{I}}}. \qquad 3\text{-}19$$

Here j_E, j_L, $j_{c\mathrm{M}}$ and $j_{c\mathrm{I}}$ are the partial derivatives of the current over the individual variables potential E, length L, and defect concentrations c_{M} and c_{I}. The impedance is calculated by the complex conjugate of the current and the voltage as:

$$Y_{\mathrm{PDM}} = \frac{\tilde{j}}{\tilde{E}} = j_E \frac{\widetilde{E}}{\widetilde{E}} + j_L \frac{\widetilde{L}}{\widetilde{E}} + j_{c_{\mathrm{M}}} \frac{\widetilde{c_{\mathrm{M}}}}{\widetilde{E}} + j_{c_{\mathrm{I}}} \frac{\widetilde{c_{\mathrm{I}}}}{\widetilde{E}} \qquad 3\text{-}20$$

The partial derivative of the current over potential is:

$$j_E = \chi F(a_1 c_{\mathrm{M}} k_1 + a_2 k_2 + a_3 k_3) + (\delta - \chi) F(a_4 k_4 + a_5 c_{\mathrm{I}} k_5 + a_7 k_7), \qquad 3\text{-}21$$

Table 3-1: Coefficients of the rate constants of the interfacial reactions. The rate constants can be calculated by: $\boldsymbol{k_i = k_i^0 \exp\left(a_i E_{\mathrm{ext}} + b_i L\right)}$.

Reaction	a_i	b_i
(1) $\mathrm{me} + \mathrm{V_M^{\chi'}} \overset{k_1}{\rightarrow} \mathrm{Me_{ox}} + \nu_\mathrm{m} + \chi \mathrm{e^-}$	$\frac{\chi\alpha_1 F(1-\alpha)}{RT}$	$-\frac{\alpha_1 \chi F}{RT} E_\mathrm{F}$
(2) $\mathrm{me} \overset{k_2}{\rightarrow} \mathrm{Me_{ox}} + \frac{\chi}{2}\mathrm{V_{\ddot{O}}} + \chi \mathrm{e^-}$	$\frac{\chi\alpha_2 F(1-\alpha)}{RT}$	$-\frac{\alpha_1 \chi F}{RT} E_\mathrm{F}$
(3) $\mathrm{me} \overset{k_3}{\rightarrow} \mathrm{Me_i^{\chi+}} + \nu_\mathrm{m} + \chi \mathrm{e^-}$	$\frac{\chi\alpha_3 F(1-\alpha)}{RT}$	$-\frac{\alpha_1 \chi F}{RT} E_\mathrm{F}$
(4) $\mathrm{Me_{ox}} \overset{k_4}{\rightarrow} \mathrm{Me^{\delta+}} + \mathrm{V_M^{\chi'}} + (\delta-\chi)\mathrm{e^-}$	$\frac{(\delta-\chi)\alpha_4 F\alpha}{RT}$	
(5) $\mathrm{Me_i^{\chi+}} \overset{k_5}{\rightarrow} \mathrm{Me^{\delta+}} + (\delta-\chi)\mathrm{e^-}$	$\frac{(\delta-\chi)\alpha_5 F\alpha}{RT}$	
(6) $\frac{\chi}{2}\mathrm{V_{\ddot{O}}} + \frac{\chi}{2}\mathrm{H_2O} \overset{k_6}{\rightarrow} \frac{\chi}{2}\mathrm{O_{ox}} + \chi \mathrm{H^+}$	$\frac{\alpha_6 F\alpha}{RT}$	
(7) $\mathrm{MO_{\chi/2}} + \chi \mathrm{H^+} \overset{k_7}{\rightarrow} \mathrm{Me^{\delta+}} + \frac{\chi}{2}\mathrm{H_2O} + (\delta-\chi)\mathrm{e^-}$	$\frac{(\delta-\chi)\alpha_7 F\alpha}{RT}$	

the partial derivative of the current over film thickness is:

$$j_L = -\chi F(b_1 c_\mathrm{M} k_1 + b_2 k_2 + b_3 k_3), \qquad 3\text{-}22$$

the partial derivative of the current over metal vacancies concentration is:

$$j_{c_\mathrm{M}} = F\chi k_1 \qquad 3\text{-}23$$

And the partial derivate of the current over the metal interstitials concentration is:

$$j_{c_\mathrm{I}} = F(\delta-\chi)k_5. \qquad 3\text{-}24$$

The constants a_i and b_i are summarized in Table 3-1.

For the complete impedance model the derivation of the expressions $\tilde{L}/\tilde{E}$, $\tilde{c}_\mathrm{M}/\tilde{E}$ and $\tilde{c_\mathrm{I}}/\tilde{E}$ is necessary.

3.5.2.1 Derivation $\tilde{L}/\tilde{E}$

The rate of change of the film thickness is given by Equation 3-13 as $\mathrm{d}L/\mathrm{d}t = \Omega(k_2 - k_7)$,

the rate constants can be expressed through the steady state value $\bar{k}_i$ via Taylor series expansion as [31]:

$$k_2 = \bar{k}_2 + a_2\bar{k}_2\tilde{E}\exp(j\omega t) + b_2\bar{k}_2\tilde{L}\exp(j\omega t) \quad 3\text{-}25$$

$$k_7 = \bar{k}_7 + a_7\bar{k}_7\tilde{E}\exp(j\omega t). \quad 3\text{-}26$$

Taking the time derivate and substituting the above expressions in Equation 3-13 yields:

$$i\omega\tilde{L}\exp(j\omega t) = \Omega(\bar{k}_2 + a_2\bar{k}_2\tilde{E}\exp(j\omega t) + b_2\bar{k}_2\tilde{L}\exp(j\omega t) - \bar{k}_7 - a_7\bar{k}_7\tilde{E}\exp(j\omega t)), \quad 3\text{-}27$$

which can be transformed to:

$$i\omega\tilde{L} = \Omega\big((\bar{k}_2 - k_7)\exp(-i\omega t) + a_2\bar{k}_2\tilde{E} + b_2\bar{k}_2\tilde{L} - a_7\bar{k}_7\tilde{E}\big). \quad 3\text{-}28$$

Taking the time average of the above equation it is possible to neglect the first term on the right hand side of the equation and yielding:

$$i\omega\tilde{L} = \Omega(a_2\bar{k}_2\tilde{E} + b_2\bar{k}_2\tilde{L} - a_7\bar{k}_7\tilde{E}) \quad 3\text{-}29$$

and finally:

$$\frac{\tilde{L}}{\tilde{E}} = \frac{\Omega\big(a_2\bar{k}_2 - a_7\bar{k}_7\big)}{i\omega - \bar{k}_2\bar{b}_2}. \quad 3\text{-}30$$

3.5.2.2 Derivation $\tilde{c_I}/\tilde{E}$

For the calculation of the defect concentration it is necessary to calculate the flux of interstitials and vacancies. The flux J of a charged species d in an electric field can be calculated by the Nernst-Planck equation:

$$J_d = -D_d\frac{\partial c_d}{\partial x} + \frac{z_d F D_d}{RT}E_{\mathrm{F}}c_d, \quad 3\text{-}31$$

with the diffusion coefficient D_d of species d. Accordingly, the continuum equation is:

$$\frac{\partial c_d}{\partial t} = -D_d\frac{\partial^2 c_d}{\partial x^2} + \frac{z_d F D_d}{RT}E_{\mathrm{F}}\frac{\partial c_d}{\partial x}. \quad 3\text{-}32$$

The boundary conditions at $x = 0$ (film/solution interface) and $x = L$ (metal/film interface) for metal interstitials are:

$$x = 0 \qquad -k_5 c_{\mathrm{I}}^0 = -D_{\mathrm{I}} \frac{\partial c_{\mathrm{I}}}{\partial x} - \frac{z_d F D_d}{RT} E_{\mathrm{F}} \frac{\partial c_d}{\partial x} \qquad 3\text{-}33$$

$$x = L \qquad -k_3 = -D_{\mathrm{I}} \frac{\partial c_{\mathrm{I}}}{\partial x} - \frac{z_d F D_d}{RT} E_{\mathrm{F}} \frac{\partial c_d}{\partial x}. \qquad 3\text{-}34$$

The interstitials concentration c_{I} is given by:

$$c_{\mathrm{I}} = \bar{c}_{\mathrm{I}} + c_{\mathrm{I}} \exp(i\omega t). \qquad 3\text{-}35$$

Substituting Equation 3-35 in Equation 3-32, multiplying both sides with $\exp(-i\omega t)$ and taking the time average we have:

$$i\omega \tilde{c}_{\mathrm{I}} = D_{\mathrm{I}} \frac{\partial^2 \tilde{c}_{\mathrm{I}}}{\partial x^2} + \frac{\chi F D_{\mathrm{I}}}{RT} E_{\mathrm{F}} \frac{\partial \tilde{c}_{\mathrm{I}}}{\partial x}. \qquad 3\text{-}36$$

The solution of this differential equation can be found as:

$$\tilde{c}_{\mathrm{I}} = A \exp(r_1 x) + B \exp(r_2 x), \qquad 3\text{-}37$$

where

$$r_{1,2} = \frac{-\chi K \pm \sqrt{\chi^2 K^2 - 4i\omega / D_{\mathrm{I}}}}{2} \qquad 3\text{-}38$$

and $K = FE_{\mathrm{F}}/RT$. To employ the boundary conditions and solve for A and B it is necessary to linearize Equation 3-33 and Equation 3-34. These yields:

$$k_5 c_{\mathrm{I}} = (\bar{k}_5 + a_5 \bar{k}_5 \tilde{E} \exp(i\omega t))(\bar{c}_{\mathrm{I}} + \tilde{c}_{\mathrm{I}} \exp(i\omega t)) \qquad 3\text{-}39$$

and:

$$k_3 = \bar{k}_3 (a_3 \tilde{E} + b_3 \tilde{L}) \exp(i\omega t)). \qquad 3\text{-}40$$

The substitution of the linearized forms into the boundary conditions leads to

$$-\left(\bar{k}_5 + a_5\bar{k}_5\tilde{E}\exp(i\omega t)\right)\left(\bar{c_{\mathrm{I}}} + \tilde{c_{\mathrm{I}}}\exp(i\omega t)\right) =$$

$$-D_{\mathrm{I}}\frac{\partial\bar{c_{\mathrm{I}}}}{\partial x}\Big|_{x=0} - D_{\mathrm{I}}\exp(i\omega t)\frac{\partial\tilde{c_{\mathrm{I}}}}{\partial x}\Big|_{x=0} - \chi D_{\mathrm{I}}K\bar{c_{\mathrm{I}}}^0 - \chi D_{\mathrm{I}}K\tilde{c_{\mathrm{I}}}^0\exp(i\omega t)\,, x = 0 \qquad 3\text{-}41$$

and

$$-\bar{k}_3(a_3\tilde{E} + b_3\tilde{L})\exp(i\omega t)) =$$

$$-D_{\mathrm{I}}\frac{\partial\bar{c_{\mathrm{I}}}}{\partial x}\Big|_{x=L} - D_{\mathrm{I}}\exp(i\omega t)\frac{\partial\tilde{c_{\mathrm{I}}}}{\partial x}\Big|_{x=L} - \chi D_{\mathrm{I}}K\bar{c_{\mathrm{I}}}^L - \chi D_{\mathrm{I}}K\tilde{c_{\mathrm{I}}}^L\exp(i\omega t)\,, x = L. \qquad 3\text{-}42$$

The multiplication of both equation with $\exp(-i\omega t)$ and calculating the time average leads to:

$$-\bar{k}_5(a_5\bar{c_{\mathrm{I}}}^0\tilde{E} + \tilde{c_{\mathrm{I}}}^0) = -D_{\mathrm{I}}\frac{\partial\tilde{c_{\mathrm{I}}}}{\partial x}\Big|_{x=0} - \chi D_{\mathrm{I}}K\tilde{c_{\mathrm{I}}}^0, x = 0 \qquad 3\text{-}43$$

$$-\bar{k}_3\left(a_3\tilde{E} + b_3\tilde{L}\right)0 - D_{\mathrm{I}}\frac{\partial\tilde{c_{\mathrm{I}}}}{\partial x}\Big|_{x=L} - \chi D_{\mathrm{I}}K\bar{c_{\mathrm{I}}}^L, x = L. \qquad 3\text{-}44$$

Combining the solution for $\tilde{c_{\mathrm{I}}}$ and the boundary conditions, the equations can be rewritten as:

$$\left\{(r_1 + \chi K)D_{\mathrm{I}} - \bar{k}_5)\right\}A + \left\{(r_2 + \chi K)D_{\mathrm{I}} + \bar{k}_5\right\}B = \bar{k}_5 a_5\bar{c_{\mathrm{I}}}^0\bar{E} \qquad 3\text{-}45$$

and

$$\left\{(r_1 + \chi K)D_{\mathrm{I}}\exp(r_1 L) - \bar{k}_5)\right\}A + \left\{(r_2 + \chi K)D_{\mathrm{I}}\exp(r_2 L) + \bar{k}_5\right\}B = \bar{k}_3(a_3\bar{E} + b_3\bar{L}. \qquad 3\text{-}46$$

Using both boundary conditions it is possible to solve the continuums equation. First, we rewrite the boundary conditions as:

$$a_{11}A + a_{12}B = \bar{k}_5 a_5\,\bar{c_i}^0\tilde{E} \qquad 3\text{-}47$$

and:

$$a_{21}A + a_{22}B = \bar{k}_3\left(a_3\tilde{E} + b_3\tilde{L}\right). \quad 3\text{-}48$$

Using the following definitions:

$$\begin{gathered} a_{11} = (r_1 - 3K)D_\mathrm{I}; a_{12}(r_2 - 3K)D_\mathrm{I}; \\ a_{21}[(r_1 - 3K)D_\mathrm{I} + k_1]\exp(r_1 L)\,; a_{22}[(r_2 - 3K)D_\mathrm{I} + k_1]\exp(r_2 L) \end{gathered} \quad 3\text{-}49$$

and

$$b_{1E} = \bar{k}_5 a_5 \bar{c}_\mathrm{I}, b_{2E} = \bar{k}_3 a_3, b_{2L} = \bar{k}_3 b_3. \quad 3\text{-}50$$

The system of equations can be solved using the Cramer's rule: $Ax = b;\ x_i = \det A_i / \det A$ and the solution at $x = 0$ is:

$$\tilde{c}_i(x = 0) = A + B \quad 3\text{-}51$$

leading to the concentration of interstitials at the film solution interface ($x = 0$) as:

$$\tilde{c}_\mathrm{I}^0 = \tilde{c}_{\mathrm{I}E}^0\tilde{E} + \tilde{c}_{\mathrm{I}L}^0\tilde{L}. \quad 3\text{-}52$$

With

$$\tilde{c}_{\mathrm{I}E}^0 = \frac{b_{1E}(a_{22} - a_{21}) + b_{2E}(a_{11} - a_{22})}{a_{11}a_{22} - a_{12}a_{21}}, \quad 3\text{-}53$$

$$\tilde{c}_{\mathrm{I}L}^0 = \frac{b_{2L}(a_{11} - a_{22})}{a_{11}a_{22} - a_{12}a_{21}}, \quad 3\text{-}54$$

the expression $\tilde{c}_\mathrm{I}^0/\tilde{E}$ we are looking for results as:

$$\frac{\tilde{c}_\mathrm{I}^0}{\tilde{E}} = \tilde{c}_{\mathrm{I}E}^0 + \tilde{c}_{\mathrm{I}L}^0\frac{\tilde{L}}{\tilde{E}} \quad 3\text{-}55$$

with the already known expression $\tilde{L}/\tilde{E}$.

3.5.2.3 Derivation $\tilde{c}_M/\tilde{E}$

The derivation of $\tilde{c}_\mathrm{M}/\tilde{E}$ can be done equivalent to the derivation of $\tilde{c}_\mathrm{I}/\tilde{E}$. It results in the

expression:

$$\frac{\tilde{c}_{\mathrm{M}}}{\tilde{E}} = \tilde{c}_{\mathrm{M}E}^{L} + \tilde{c}_{\mathrm{M}L}^{L}\frac{\tilde{L}}{\tilde{E}}. \tag{3-56}$$

With

$$\tilde{c}_{\mathrm{M}E}^{L} = \frac{(b_{1E}a_{22} - b_{2E}a_{12})\exp(r_1 L) + (b_{2E}a_{11} - b_{1E}a_{12})\exp(r_2 L)}{a_{11}a_{22} - a_{12}a_{21}}, \tag{3-57}$$

$$\tilde{c}_{\mathrm{M}L}^{L} = \frac{-a_{12}b_{2L}\exp(r_1 L) + a_{11}b_{2L}\exp(r_2 L)}{a_{11}a_{22} - a_{12}a_{21}} \tag{3-58}$$

and

$$r_{1,2} = \frac{3K \pm \sqrt{3^2K^2 + 4i\omega/D_E}}{2}, \tag{3-59}$$

$$a_{11} = (r_1 - 3K)D_{\mathrm{M}};\ a_{12}(r_2 - 3K)D_{\mathrm{M}};\\ a_{21}[(r_1 - 3K)D_{\mathrm{M}} + k_1]\exp(r_1 L)\,;\ a_{22}[(r_2 - 3K)D_{\mathrm{M}} + k_1]\exp(r_2 L), \tag{3-60}$$

$$b_{1E} = -k_4 a_4;\ b_{2E} = -k_1 a_1 C_{\mathrm{M}}^{L};\ b_{2L} = k_1 C_{\mathrm{M}}^{L} b_1. \tag{3-61}$$

With the above expressions the full impedance due to passive film growth, production and consumption of interstitials and vacancies and dissolution of passive film can be written as:

$$Y_{\mathrm{PDM}} = j_E\frac{\tilde{E}}{\tilde{E}} + j_L\frac{\tilde{L}}{\tilde{E}} + j_{c_{\mathrm{M}}}\frac{\tilde{c_{\mathrm{M}}}}{\tilde{E}} + j_{c_{\mathrm{I}}}\frac{\tilde{c_{\mathrm{I}}}}{\tilde{E}}. \tag{3-62}$$

This impedance model describes a huge set of possible reactions and transport phenomena regarding metal passivity. The advantages of such a comprehensive model, physical accuracy and detailed description, can also be a difficulty in case of working with the model. Impedance signals of passivated metal surfaces are often less complex in the measuring range and the model harbors the risk of being overdetermined. This difficulty and how it is possible to overcome for practical use of the PDM is described in the following chapter.

4

PARAMETRIZING THE PDM

With four parameters I can fit an elephant
and with five I can make him wiggle his trunk.
John von Neumann

The Point Defect Model, which is described in detail in Section 3.5, is used in this thesis to reveal the influences of microstructures and material treatments on observed electrochemical phenomena. As mentioned before, the fitting of the full PDM to impedance data of passivated metal surfaces can lead to overfitting because the EIS data is often less complex and can be described with amazing accuracy by equivalent electrical circuits consisting of one to two time constants and one to two real resistances plus one electrolyte resistance. In the work presented in this thesis, the PDM is used for the first time to compare different treated materials with each other. For this reason, it is particularly important to avoid overfitting and to guarantee comparability of the kinetic parameter of each sample. For this purpose, the PDM was reduced and the parameter relationships were clarified. How this has been achieved is presented in this chapter.

4.1 FITTING PASSIVATED METAL SURFACES BY EECS

To understand the fitting of the PDM to impedance data it is helpful to consider how passivated surface are usually fitted by equivalent electrical circuits (EECs). The three most common EECs used to describe passivated metals are presented in Figure 4-1. EEC1 consist, as every of the 3 circuits, of an electrolyte resistance R_{el} depending on the solutions resistance. The constant phase element (CPE) CPE_1 reflects the capacitive behavior of the film and the double layer. A CPE is used instead of a capacity because passive films often show inhomogeneity (resulting from roughness, dislocations, grain boundaries etc.) [76] and a CPE can reflect this behavior [21]. The polarization resistance R_1 reflects electron transfer due to electrochemical reactions at the film/solution interface. This EEC is used to simulate impedance data of passivated metal surfaces that can be modeled with one time constant [76–79]. Under given circumstances it can be necessary to add a Warburg impedance to this EEC to reflect diffusion processes at the surface or inside the film [79].

The equivalent electrical circuit EEC2 separates the double layer and the passive film. The capacity C_{dl} represents the double layer (it can sometimes be exchanged by a CPE) and R_{ct} is the charge transfer resistance at the double layer/film interface. The constant phase element CPE_{pl} represents the capacitive behavior of the passive layer and R_2 the electrochemical reactions at the film interfaces [53,80–83].

EEC3 is originally used to model the impedance behavior of a particularly blocked electrode [21]. In this case CPE_1 represents the film at the electrode surface while the parallel arranged elements model the impedance behavior in the pores of the film. This is done by the solution resistance of the pore R_1 (which differs to the solution outer resistance R_{el} due to the reduced area of the pores) and the capacity of the double layer CPE_2 and the charge transfer resistance between the double layer and the unblocked electrode surface inside the pores R_2 [55,84,85]. This interpretation can reflect porous oxide layer on metal electrodes but seems contrary to the model of a dense protecting passive film. Concerning this contradiction, different interpretations of the elements can be found in literature. Pan and Leygraf suggested CPE_1 and R_1 as the impedance response of the outer layer and CPE_2 and R_2 of the inner layer [85]. Considering the nature of the EEC this would mean the potential drop of the outer layer reaches from the outer surface of the oxide bilayer to the metal surface. This would be comparable to a porous barrier layer "filled" with outer layer. This seems contrary to findings about the structure of the passive layers. Bou-Saleh *et al.* interpreted CPE_1 and R_1 as the impedance response of the double layer and electrolyte and CPE_2 and R_2 as the impedance of the passive layer resulting in a somehow inversed structure of the partially blocked electrode [55]. It is not surprising that these models are able to fit the impedance data of passivated surfaces but the physical meaning seems questionable.

More complex EECs are also presented in literature [75,86,87], but they tend to risk over-fitting if the impedance data is not sufficiently complex and no additional knowledge about the system is included. To avoid over-determined systems it is good practice to reduce the EEC as far as possible without losing significant fit quality in order to reduce the set of fitting parameters since, how John von Neumann stated, "With four parameters I can fit an elephant and with five I can make him wiggle his trunk."

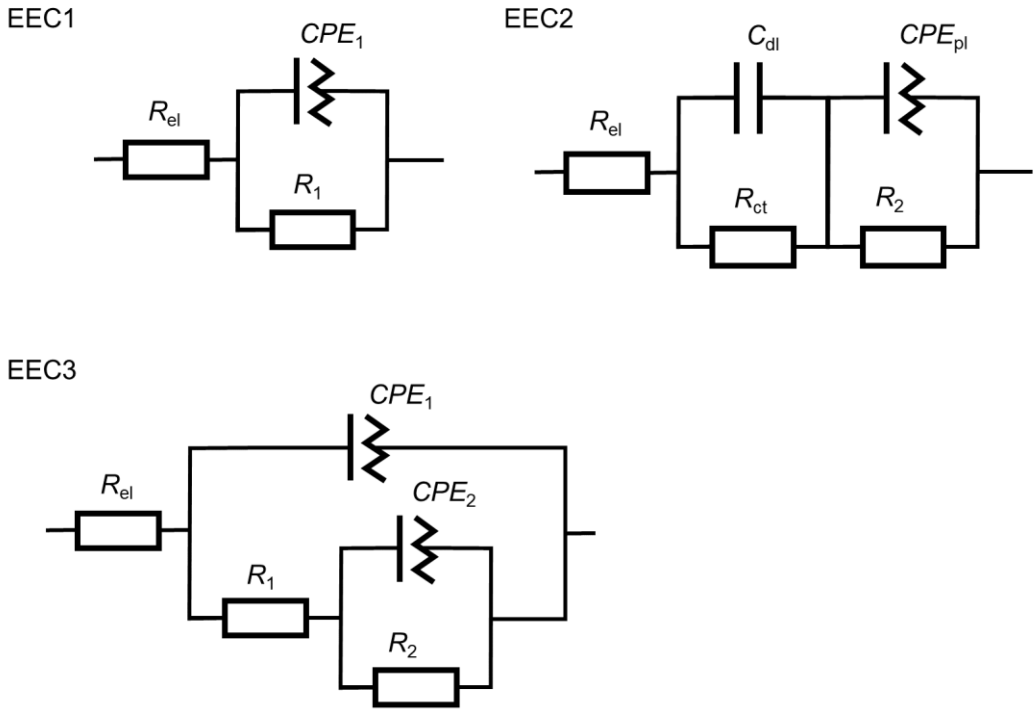

Figure 4-1: Commonly used equivalent electrical circuits (EECs) to model impedance data of passivated metal surfaces. EEC1 consists of an electrolyte resistance R_{el}, an constant phase element CPE_1 that reflects the capacitive behavior of the double layer and the passive film and a polarization resistance R_1, which reflects the electrochemical reactions at the film/solution interface; EEC2 seperates the passive film and the double layer, which is represented by one capacity for the double layer and a charge transfer resistance for electron transfer at the double layer/film interface and a CPE representing the capacitive behavior of the passive film as well as a resistance R_2 for the electrochemical reactions regarding passive film growth and dissolution. EEC3 also separates the double layer and the passive film. In this representation CPE_1 can be a porous, electrolyte-filled film without inherent reactions.

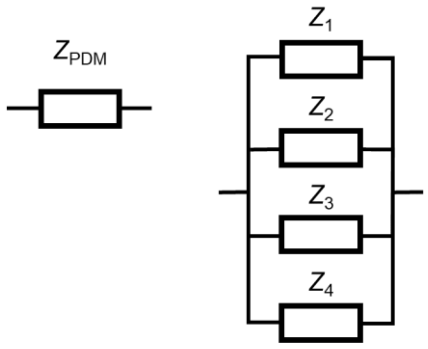

Figure 4-2: Seperation of the PDM impedance into single parallel impedance elements

Table 4-1: Admittances of the single impedance elements derived by the PDM

Element	Impedance
Z_1	$1/j_E$
Z_2	$1/(j_L \frac{\widetilde{L}}{\widetilde{E}})$
Z_3	$1/(j_{c_M} \frac{\widetilde{c_M}}{\widetilde{E}})$
Z_4	$1/(j_{c_I} \frac{\widetilde{c_I}}{\widetilde{E}})$

4.2 How does the PDM fit into EECs?

Every EEC shown in Figure 4-1 consists of a resistance that represents the electrochemical reactions in and at the passive layer. Sometimes a Warburg impedance is added to the resistance to reflect diffusion processes or an inductivity to model active dissolution [28] or surface relaxation processes of species in the passive film or the buildup of surface charges [29,30]. However, if these elements are added the impedance data must reflect this behavior, which is often not the case for metals in a passive state.

The impedance Z_{PDM} of the PDM is exactly at the place of the impedance elements representing electrochemical reactions and processes in the passive film and at its interfaces (R_1 in EEC1, R_2 in EEC2 and R_1 or R_2 in EEC3). A detailed look at the impedance Z_{PDM} reveals the scheme presented in Figure 4-2. It can be subdivided into four elements Z_1 to Z_4 which are, according to the admittance developed in section 3.5.2:

$$Y_{\mathrm{PDM}} = j_E \frac{\widetilde{E}}{\widetilde{E}} + j_L \frac{\widetilde{L}}{\widetilde{E}} + j_{c_M} \frac{\widetilde{c_M}}{\widetilde{E}} + j_{c_I} \frac{\widetilde{c_I}}{\widetilde{E}} \qquad 4\text{-}1$$

and the relationship:

$$\frac{1}{Z_{\mathrm{PDM}}} = Y_{\mathrm{PDM}} = \frac{1}{Z_1} + \frac{1}{Z_2} + \frac{1}{Z_3} + \frac{1}{Z_4} \qquad 4\text{-}2$$

presented in Table 4-1. The impedance Z_1 can be interpreted as resistance with

$$R_1 = \frac{1}{j_E}. \tag{4-3}$$

Z_2 has the form of a resistance and an inductivity in a row:

$$Z_2 = \frac{1}{j_L \frac{\Omega\left(a_2\bar{k}_2 - a_7\bar{k}_7\right)}{i\omega - \bar{k}_2\bar{b}_2}} = \frac{i\omega - \bar{k}_2\bar{b}_2}{\mathrm{j}_L\Omega\left(a_2\bar{k}_2 - a_7\bar{k}_7\right)} = R_2 + L_1 i\omega, \tag{4-4}$$

with

$$R_2 = \frac{-\bar{k}_2\bar{b}_2}{\mathrm{j}_L\Omega\left(a_2\bar{k}_2 - a_7\bar{k}_7\right)}, L_1 = \frac{1}{\mathrm{j}_L\Omega\left(a_2\bar{k}_2 - a_7\bar{k}_7\right)}. \tag{4-5}$$

The impedance elements Z_3 and Z_4 cannot interpreted that easily as circuit elements but the impedance behavior of the single elements can be calculated. The phase angle of the impedance elements Z_1, Z_2, Z_3 and Z_4 for an artificial material are presented in Figure 4-3a (kinetic constants see section A4, the constants are chosen with respect to various publications [62,74,75,88,89] to reflect physical reasonable behavior). As expected for a resistor Z_1 shows a phase angle of 0 ° over the complete frequency range and Z_2 shows the typical phase angle of an inductivity of 90 °. The phase of Z_3 begins with a phase angle of -135 ° and approaches -90 ° (phase angle of a capacity). The element Z_4 starts with a phase angle of approximate 45 ° and approaches 90 °. Both elements show diffusion-controlled behavior at high frequencies due to the transport of defects. The comparison of the absolute impedances in the typical frequency interval of EIS measurements show very differing behavior of the single elements (Figure 4-3b). The absolute value of the impedance differs in several orders of magnitude. The overall impedance of Z_1 is – as expected – independent of the frequency and for this artificial metal in the order of 10^4, while Z_2 is in the order of 10^8 and Z_3 and Z_4 of 10^{16} at low frequencies.

As already described all impedance elements are in a parallel connection. Thus, the very high impedances of Z_2, Z_3 and Z_4 should not contribute significantly to the overall impedance. The Nyquist plot of EEC1 with the Z_{PDM} as faradaic impedance is presented in Figure 4-4. The impedance of only $Z_1$is compared to the impedances resulting of the addition of the additional impedance elements. It is no change of impedance visible by adding the impedances due to response of film thickness to the voltage perturbations (Z_2) or the defect transport through the passive film (Z_3, Z_4).

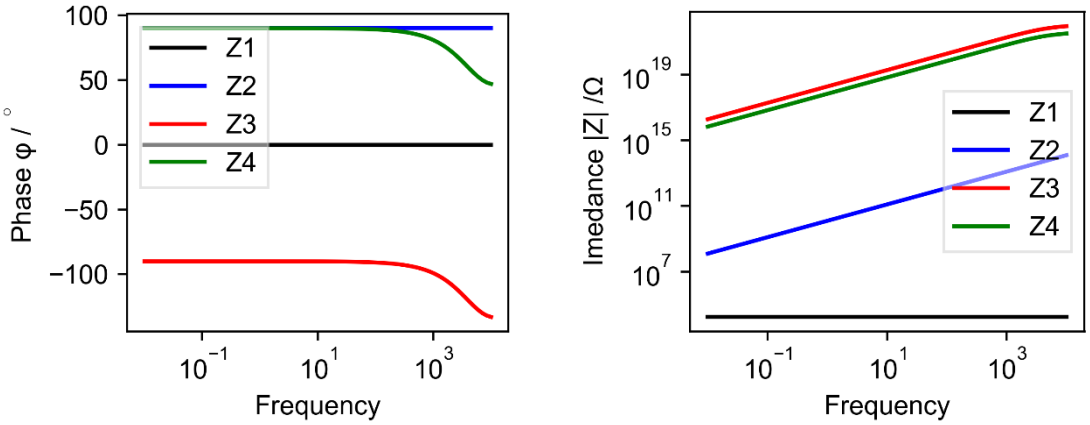

Figure 4-3: a) Phase angle, b) absolute impedance of the single impedance elements resulting from the current with respect to potential perturbations ($\boldsymbol{Z_1}$) film thickness perturbations ($\boldsymbol{Z_2}$), interstials ($\boldsymbol{Z_3}$) and metal vacanices transport ($\boldsymbol{Z_4}$).

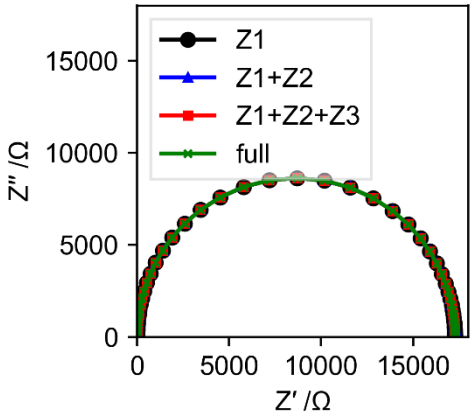

Figure 4-4: Nyquist plot of several combinations of impedance elements resulting from the impedance derivation regarding the PDM.

The question that arises from these observations is that of physical reasonableness. The change of passive layer thickness due to voltage perturbations (reflected by Z_2) is initially only a mathematical quantity. Physically meaning becomes important if the thickness change exceeds the range of the atomic diameter of the metal ions in the oxide. If this is not the case this impedance response can be neglected and completely removed from Z_{PDM}.

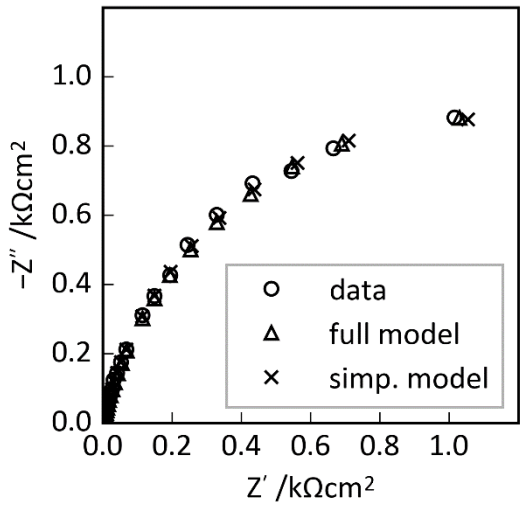

Figure 4-5: Nyquist plot of impedance data (of measurements shown in Chapter 6) of passivated martensitic steel in 0.5 M sulfuric acid (∘) and simulation via full (**Δ**) and simplified (×) PDM.

Table 4-2: Kinetic parameters obtained by fitting a full and simplified model to EIS data

Parameter	Full Model	Simplified Model
k_1^0	2.34×10^{-14}	–
α_1	0.13	–
k_2^0	7.25×10^{-11}	7.66×10^{-11}
α_2	0.028	0.028
k_4^0	2.56×10^{-14}	–
α_4	0.01	–
k_5'	2.93×10^{-10}	3.05×10^{-10}
E_F	1.12×10^{6}	1.0×10^{6}
φ_{fs}	0.1	0.1
D_v	7×10^{-16}	–
n	0.875	0.875
R^2	0.9974	0.9970

In the case of n-type oxide films, metal interstitials and oxygen vacancies are the main defects [54]. Considering this, Reaction 1:

$$\mathrm{me} + \mathrm{V}_\mathrm{M}^{\chi'} \overset{k_1}{\rightarrow} \mathrm{Me}_\mathrm{ox} + \nu_\mathrm{m} + \chi \mathrm{e}^- \tag{4-6}$$

and Reaction 4:

$$\mathrm{Me}_\mathrm{ox} \overset{k_4}{\rightarrow} \mathrm{Me}^{\delta+} + \mathrm{V}_\mathrm{M}^{\chi'} + (\delta - \chi)\mathrm{e}^-, \tag{4-7}$$

which produce and consume cation vacancies can be neglected.

Additional assumptions regarding the dissolution of the passive film components can lead to further simplifications. In the case of equal ion charge $\delta = \chi$ Reaction 4 and Reaction 5:

$$\mathrm{Me}_\mathrm{i}^{\chi+} \overset{k_5}{\rightarrow} \mathrm{Me}^{\delta+} + (\delta - \chi)\mathrm{e}^- \tag{4-8}$$

can be neglected.

These considerations lead to a simplification of Z_1 due to a reduction of the involved reactions. Furthermore Z_2 can be neglected if the change of film thickness $\tilde{L}/\tilde{E}$ does not exceed

the atomic diameter. In the case of n-type oxides (as the passive film on carbon steel) theiimpedance Z_3 resulting from concentration perturbations of metal vacancies (not present in decisive amounts) can be neglected.

A comparison of the kinetic parameters obtained via an impedance model that includes the metal vacancies transport (full model) and a model without this transport and the corresponding reactions (simp. modell) of a passivated stainless steel sample revealed nearly no loss of fit quality and almost identical fitting parameters (Figure 4-5 and Table 4-2). The sample shown in Figure 4-5 has been passivated in sulfuric acid for 1800 s at 0.6 V. The impedance data was obtained at a DC potential of 0.6 V in the frequency range of $10^{-2} - 10^{5}$ Hz.

4.3 Parameter Dependencies

The additional assumptions for the reduction of the impedance model discussed in the previous section are:

- The charge of the dissolved metal ions equals the charge of the metal ions inside the passive film; $\delta = \chi$.
- The defects inside the passive film are interstitials and oxygen vacancies; the formation of metal interstitials is neglected since the passive film shows n-type behavior.
- Neglecting the film perturbations due to top voltage perturbations because the change of film thickness does not exceed the radius of the metal atoms.

These assumptions lead to a drastically reduced model:

$$Z_{\mathrm{PDM}} = \frac{1}{j_E} = \frac{1}{\chi F(a_2 k_2 + a_3 k_3)}. \qquad 4\text{-}9$$

As discussed before, because this impedance is frequency independent, it can be interpreted as a resistor. Considering the EECs presented in Figure 4-1, which are in most cases sufficient to fit EIS data, this is a reasonable assumption. But we still end up with one scalar value (for example R_2 in EEC2) which is described by nine parameters: $k_2^{0\prime}, k_3^{0\prime}, \alpha, \alpha_2, \alpha_3, \beta_2, \beta_3, E_{\mathrm{F}}, \varphi_{\mathrm{fs}}^0$, resulting from the nature of the rate constant of Reaction i:

$$k_i = k_i^{0\prime} \exp\left(\frac{\alpha_i \chi F}{RT}\left((1-\alpha)E_{\mathrm{ext}} - E_{\mathrm{F}}L - \beta_i \mathrm{pH} - \varphi_{fs}^0\right)\right), i = 2{,}3. \qquad 4\text{-}10$$

Considering the huge number of parameters, which in the end describe one scalar value obtained by EIS measurements, an infinite combination of parameters can be found to satisfy the measured impedance data (Figure 4-6). This clarifies the need of parameter reductions or dependencies.

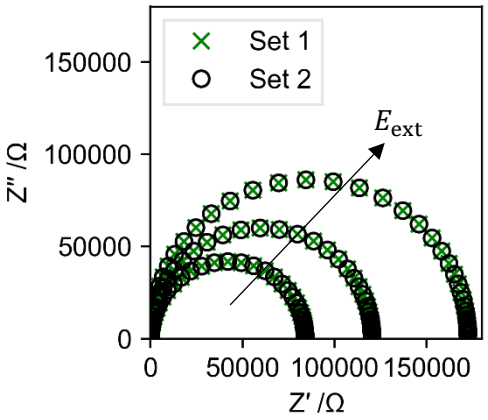

Figure 4-6: Nyquist plot resulting from a reduced PDM with differing parameters; an infinite combination of different parameters leading to the same impedance is possible.

Table 4-3: Parameter sets for the PDM used in Figure 4-6

Parameter	Set 1	Set 2
α	0.7	0.76
a_2	12	15
a_3	12	15
k_2^0	1×10^{-12}	8×10^{-13}
k_3^0	1×10^{-14}	8×10^{-15}
E_F	10×10^6	8×10^6

Variation of Potential and pH

The variation of the external potential E_{ext} changes the impedance response regarding the parameter α, while changing the pH leads to impedance changes regarding to β. Reshaping the equation of the impedance response due to one electrochemical reaction (Y_i) makes the dependency regarding the potential clear:

$$\begin{aligned} Y_i &= a_i k_i^{0'} \exp\left(\frac{\alpha_i \chi F}{RT}\left((1-\alpha)E_{ext} - E_F L - \beta_i \mathrm{pH} - \varphi_{fs}^0\right)\right) \\ &= \exp\left(a_i(1-\alpha)E_{ext} + \ln\left(a_i k_i^{0'}\right) - a_i E_F L - a_i \beta_i \mathrm{pH} - a_i \varphi_{fs}^0\right). \end{aligned} \quad 4\text{-}11$$

The expression inside the exponential function is a linear function over E_{ext} with the slope $a_i(1-\alpha)$. That means it is possible to simulate the impedance response of the system regarding the PDM with varying external potential E_{ext} with every parameter set that satisfies the linear function:

$$\ln\left(Y_i(E_{ext})\right) = a_i(1-\alpha)E_{ext} + \ln\left(k_i^{0'}\right) - a_i E_F L - a_i \beta \mathrm{pH} - a_i \varphi_{fs}^0. \quad 4\text{-}12$$

Obviously, this results in a lot parameter sets (to be exact: infinite). The dependency on pH can be expressed similar. Since the change of both external conditions does not explicitly describe the system, it is possible to keep both conditions constant. This leads to the loss of information about the polarizability of the film/solution interface, described by α and β, regarding the potential and the pH but not the kinetic parameters of passive film growth. By

doing this, the potential drop at the film/solution interface ($\varphi_{\mathrm{fs}} = \alpha E_{\mathrm{ext}} + \beta \mathrm{pH} + \varphi_{\mathrm{fs}}^{0}$) can be considered constant. Thus, under constant potential and pH conditions the rate constant can be rewritten as:

$$k_i = k_i^{0\prime} \exp\left(\frac{\alpha_i \chi F}{RT}(E_{\mathrm{ext}} - E_{\mathrm{F}} L - \varphi_{\mathrm{fs}})\right), i = 2{,}3. \qquad 4\text{-}13$$

Assuming a constant potential drop at the film/solution interface φ_{fs} this parameter can be emerged in the base rate constant $k_i^{0\prime}$ to form the standard rate constant:

$$k_i^0 = k_i^{0\prime} \exp(-\varphi_{\mathrm{fs}}). \qquad 4\text{-}14$$

These assumptions reduce the set of fitting parameter to five (in the case of two electron generating reactions).

Dependency of polarization current on kinetic parameters

With the help of parameter dependencies some more kinetic parameters can be determined. The passivation current during polarization can be measured and should approach a constant value and can be described by:

$$j_{\mathrm{pas}} = \chi F(k_2 + k_3). \qquad 4\text{-}15$$

Dependency of film thickness on kinetic parameters

The passive film thickness can be calculated by the EEC element describing the capacitive behavior of the passive film (for example CPE_{pl} in EEC2) and is determined by some kinetic parameter. Under the given conditions it can be calculated by:

$$L = \frac{E_{\mathrm{ext}}}{E_{\mathrm{F}}} - \frac{1}{E_{\mathrm{F}} a_2} \ln\left(\frac{k_7}{k_2^0}\right). \qquad 4\text{-}16$$

Following the approach of Hirschorn et al. the film thickness can be calculated by CPE parameter as [90]:

$$L = \frac{(\varepsilon_0 \varepsilon)^N}{g Y \rho_L^{(1-N)}}. \qquad 4\text{-}17$$

The necessary parameters are: the permittivity of the vacuum ε_0 (8.85×10^{-12} $\mathrm{AsV^{-1}m^{-1}}$), the dielectric constant of the oxide ε, the CPE parameters N and Y, g = $1+2.88(1-N)^{2.375}$ and

ρ_L= 450 Ωcm (for stainless steel).

A further helpful dependency is the equilibrium of film growth and dissolution at steady state, which leads to:

$$k_2^{ss} = k_7. \qquad 4\text{-}18$$

These assumptions and dependencies can help to find clearly assigned kinetic parameters, which allow comparing the passive film growth kinetics of differently treated materials among themselves. For the purpose of this thesis additional assumption were made. It is not possible to separate the currents regarding the single elements (mainly chromium and iron) and their reactions. The measured currents at the metal/film and film/solution interface are always a mixture of the reaction of both metals, chromium and iron, to oxides or interstitials in the film (Reaction 2 and 3). The dissolution of passive film at the film/solution interface is always a mixed dissolution of iron oxides and chromium oxides. That means the calculated reaction constants are combined of the reaction of all involved metal species and of the dissolution of all present oxides. Furthermore, it is assumed that the only present oxides in the film are Me_2O_3 oxides, namely Fe_2O_3 and Cr_2O_3.

Because the current assigned to film growth of the oxide (depending on Reaction 2) and the current assigned to the production of interstitials (depending on Reaction 3) cannot be distinguished, it is assumed the only defects present in the oxide film are oxygen vacancies and thus reaction 3 is neglected. This reduces the set of parameters to 3 depending kinetic parameters which enables successful fitting.

5

MICROSTRUCTURE AND CORROSION – A LOOK AT THE CURRENT STATE OF RESEARCH[2]

Seen from outside, and even more so from within,
the process of scientific research is disorderly and confusing.
It is tempting to deduce that scientists themselves are disorderly and confused.
In a way they are – that's what research involves.
If you knew what you were doing it wouldn't be research.
Terry Pratchett - The Science of Discworld

The previous chapters dealt extensively with the subject of corrosion and passivity. It became clear that corrosion and passivity is a material specific effect. Different materials show significantly different passive behavior and between iron-chrome alloys, there are big differences based on the alloy composition, especially the chromium content.

But not only does the alloy composition play an important role regarding the corrosion

[2] Parts of this chapter have been published verbatim in *Int. J. Electrochem. Sci.*, **15** (2020) [17]

resistance. Different material treatments can affect the durability of the material as well. Different heat treatments of the same material can make the difference between stainless behavior and material failure due to corrosion. These differences are due to microstructure changes as a result of material treatments. Varying phases, carbide concentrations and grain sizes can result in completely dissimilar corrosion behavior.

The following chapter presents a look into the microstructure of iron-carbon-chrome alloys. A general overview about the different possible phases, the effect of heat treatment and its effect on corrosion is given. The second part of the chapter focuses particularly on the effects of austenitizing on the microstructure and corrosion resistance. As we will see, the observed effects are sometimes completely contrary. This might seem somehow confusing, just like Terry Pratchett stated in the quote above. Nevertheless, I hope it will become clear that this is due to the complex mechanisms, first during heat treatment on the microstructure, and afterwards during the electrochemical measurements.

5.1 The Iron-Carbon System

Iron-carbon alloys are crystalline materials. The crystal structure depends on the temperature and the alloying elements. Figure 5-1 shows the phase diagram of iron-carbon alloys with 2 wt.-% chromium. The main phase at temperatures below ca. 700 °C is an α mixed crystal, also called ferrite. Ferrite has a cubic space centered crystal structure with embedded carbon atoms (Figure 5-2). With increasing temperature the crystal structure can change to a cubic face centered γ mixed crystal, called austenite. Depending on the amount of carbon and temperature several additional phases in form of carbides can form (Figure 5-1).

Rapid heating and quenching procedures can lead to behavior deviating from the phase diagram. The quenching of carbon steel from the austenite phase with high temperature gradient, for example, can lead to a distorted lattice structure. This resulting body centered tetragonal crystal structure is called martensite and is characterized by a particularly high hardness [33]. Different phases can have differing electrochemical potentials and thus enable corrosion reactions between two phases of the same sample (compare corrosion element Section 2.3).

The nature of carbides and their concentration also affects the mechanical properties. A high amount of carbides can decrease the ductility of the material. Furthermore, the formation of carbides leads to depletions of the involved metals. A high amount of chromium carbides reduces the chromium content that is available for passivation and significantly worsens the corrosion resistance [91].

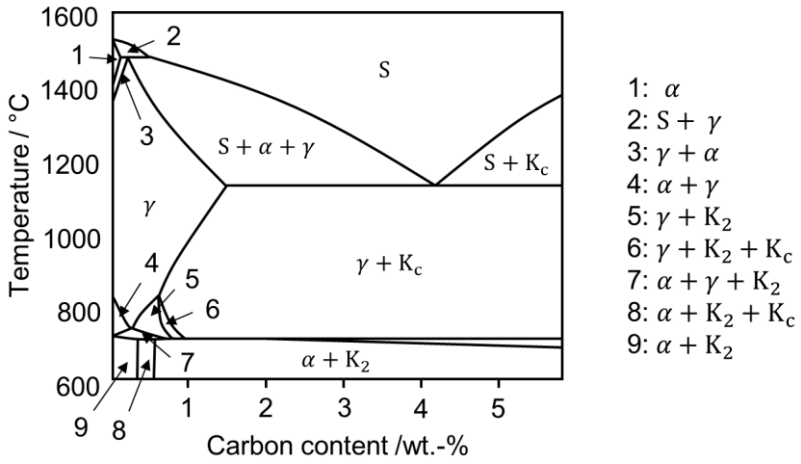

Figure 5-1: Ternary phase diagram of the Fe-Cr-C system at 2 wt.-% chromium; S: melting, $\boldsymbol{\gamma}$: $\boldsymbol{\gamma}$-austenite, $\boldsymbol{\alpha}$: $\boldsymbol{\alpha}$-ferrite, $\mathbf{K_2}$: $\mathbf{M_7C_3}$, $\mathbf{K_c}$: $\mathbf{M_3C}$; reproduced from [92].

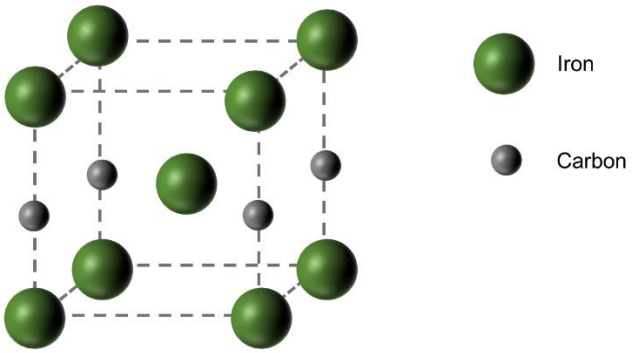

Figure 5-2: Cubic space centered crystal structure of $\boldsymbol{\alpha}$ – phase iron (ferrite) with embedded carbon atoms.

Usually the steel used for different applications does not consist of a single perfect crystal. The periodic crystal structure only exists in so called grains. These grains can be twisted and be offset to each other and can even consist of different crystal structures. For example, austenite-martensite mixed crystals are not uncommon for stainless steel. Additionally the crystal lattice can show several defects in form of atomic vacancies, interstitials or impurity atoms or the crystal can show dislocations (Figure 5-3) [93]. Those defects can show different electrochemical behavior compared to the surroundings due to different binding energies or potentials. For example, materials with a high density of grain boundaries can show an accelerated electrochemical activity. Depending on the material this can result in faster dissolution or faster passivity build up [94].

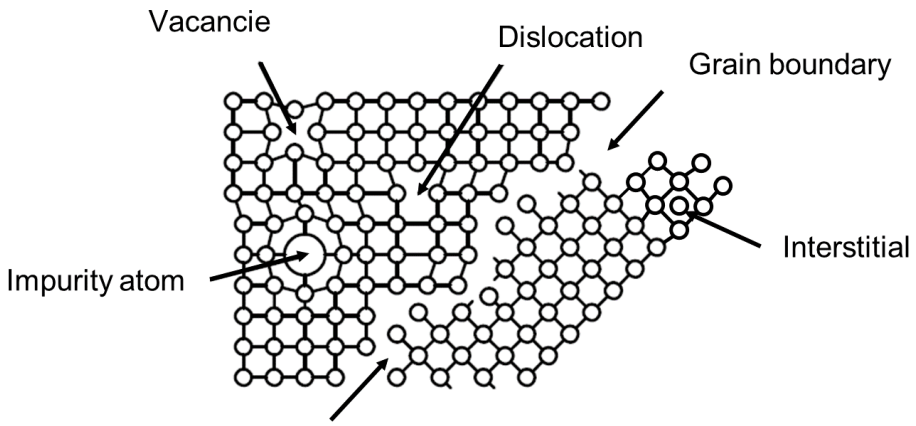

Figure 5-3: Example of common lattice defects reproduced from [93].

5.1.1 AUSTENITIZING OF STEEL

Austenitizing is a heat treatment process at which the material is heated above a critical temperature T_c. Above this temperature, the microstructure can transform from ferrite to an austenite structure. If the austenitizing is followed by quenching, martensitic phases can form and the material is hardened [33]. Not only the phase of the material changes during austenitizing but carbides can form or dissolute, the grain size can increase and the element distribution becomes more homogenous.

Hardening by austenitizing is very common for so called martensitic stainless steels with a chromium content of 13 %- 18 % and a carbon content of 0.1 % to 1.2 %, which are used as tool steels [95]. Due to the hardening, the ferritic phase structure transforms to a martensitic structure. The lattice distortions due to the transformation lead to enrichment of carbon atoms in the crystal structure which results in increased strain. This strain increases the hardness of martensitic carbon steels drastically. The complete hardening process consists of austenitizing at sufficient high temperatures (usually above 800 °C) followed by quenching at high cooling rates. If the cooling temperature is low enough (depending on the material and prior treatments) martensite is formed during lattice solidification [33].

5.1.1.1 Austenitizing of martensitic stainless steel

In 2003 Candelaria *et al.* published a short research letter regarding the corrosion resistance of martensitic stainless steel and how it was influenced by the hardening process at different austenitizing temperatures (900 °C – 1100 °C) [1]. As expected, they could observe an increasing hardness with increasing austenitizing temperature compared to the untreated sample. The increase of hardness compared to the untreated sample is due to the formation

of martensite by the quenching process, which follows the austenitizing as part of the hardening. The increase of hardness with increasing austenitizing temperature was addressed to the dissolution of $M_{23}C_6$ carbides. These carbides increase the carbon content in the martensite matrix and increase the lattice distortions and thus the hardness. Above an austenitizing temperature of 1100 °C the hardness decreases slightly, which Candelaria *et al.* addressed to the retained austenite fraction.

The corrosion resistance was measured by mass loss tests (unfortunately exact information regarding the experimental procedure are not given) and could reveal unexpected results. As mentioned above, the austenitizing process leads to the dissolution of iron and chromium carbides. Instead of decreasing mass loss with increasing austenitizing temperature due to increasing chromium content in the martensite lattice, Candelaria *et al.* observed increasing mass loss with increasing austenitizing temperature. They concluded not only the available chromium content but also a different mechanism must affect the corrosion resistance. In this research paper, they came to the conclusion that the higher amount of carbon, increasing the hardness due to the stronger lattice distortions might be the reason for higher mass loss as a result of corrosion.

A few years later, in 2007, Park *et al.* compared the effect of two different austenitizing temperatures on a martensitic stainless steel with a small Mo content [96]. In contrast to Candelaria's findings, they could observe an increased pitting resistance by increasing the austenitizing temperature from 1000 °C up to 1050 °C. However, this effect was attributed to undissolved carbides during the quenching of the 1000 °C species and it was argued – in contrast to Candelaria's findings that the lower chromium content would lead to a worse passivation. In addition, they could observe different retained austenite contents between both samples. Even though the phase distribution should have an effect on the corrosion behavior this observation was neither addressed nor discussed regarding the corrosion resistance.

In the same year – 2007 – Choi *et al.* also published a paper comparing the corrosion resistance of an martensitic stainless steel containing a small Mo content after differing heat treatments [6]. They austenitized three samples at 970 °C, 1000 °C and 1030 ° and could observe different trends for two electrochemical values. While the pitting potential, comparable to Park *et al.* (and contrary to Candelaria), increased with increasing austenitizing temperature the passive current first decreased and at 1030 °C increased again. Unfortunately, the sample set (with three different temperatures) was too small to recognize a trend but nevertheless this result was not how one would expect.

Isfahany *et al.* carried out a more comprehensive series of measurement on the effects of varying heat treatments on martensitic stainless steel in 2011 [7]. They compared the effects of three different austenitizing temperatures (980 °C, 1015 °C and 1050 °C) and for each tem-

perature three different austenitizing times (30 min, 60 min and 120 min). They could observe not only the hardness increases with increasing austenitizing temperature but that austenitizing time also affects the hardness. In this study, they only compared the corrosion behavior of two samples (980 °C and 1050 °C) via LSV measurements without information about the duration of austenitizing time or or further experimental details. Nevertheless, it was possible to observe a clear difference between the passive currents, with a drastically increased passive current for the sample with higher austenitizing temperature. Even though they did not address this in their manuscript the LSV measurements also suggest a lower breakthrough potential for the 1050 °C sample. These findings are contrary to the findings of Park and Choi but support the theory of Candelaria.

However, in 2015 Lu *et al.* and Rosemann *et al.* published, independently of each other, a series of tests on the corrosion resistance of martensitic stainless steel regarding the austenitizing temperature with a higher sample size. Lu could show an increasing pitting potential with increasing austenitizing temperature and also an increasing charge transfer resistance via EIS measurements [4]. The temperature range of the test series of Lu *et al.* was between 980 °C and 1130 °C and they compared their samples with an untreated sample.

Rosemann *et al.* measured the critical pitting potential (a potential at which the current reaches a critical value; in this study 10 μA) of an untreated sample and 4 samples austenitized at 900 °C up to 1200 °C. They could also observe increasing critical pitting potential up to 1100 °C and a constant critical pitting potential for 1200 °C compared to the 1100 °C sample [2].

Both researchers, Lu and Rosemann, attributed this behavior to the dissolution of $M_{23}C_6$ and M_7C_3 carbides, and thus the higher chromium content in the martensite lattice. In addition, a more homogeneous chromium distribution should also increase the corrosion resistance.

After the hardening, tempering reduces lattice distortions. This process can decrease the hardness and improves the deformability. Tempering at too high temperatures can lead to the new formation of chromium carbides (above 300 °C formation of Cr_3C carbides and above 550 °C formation of $Cr_{23}C_6$ carbides [97]). This formation results in chromium depletion and reduces the corrosion resistance noticeably [3,95,97–99].

5.1.1.2 Austenitizing of bearing steel

In the case of bearing steel, for example the common steel AISI 52100, austenitizing leads to enhanced hardness with increasing austenitizing time, while one can observe a hardness peak at an austenitizing temperature of ca. 900 °C. With further increase of temperature the hardness decreases again [100]. The hardness results from the retained austenite content, the carbides and the grain size. The retained austenite increases with increasing temperature, while the carbide content decreases [100,101]. A further decrease of carbides could be

achieved by cyclic austenitizing procedures [102]. Additional isothermal heat treatment, following the austenitizing, at lower temperatures (200 °C) for several hours can lead to a more uniform microstructure and further increase the hardness [103]. A systematical study on the influence of austenitizing of bearing steel on the electrochemical behavior seems not to exist.

5.1.2 Microstructure and Corrosion

As can be clearly seen, the heat treatment procedure influences different microstructure parameters. There are several studies, which address the influence of microstructure changes on the corrosion behavior. Because austenitizing affects the martensite content and the grain size, the current state of research regarding the influence of these two microstructure parameters is presented.

5.1.2.1 Influence of martensite on corrosion

The effect of martensite on the corrosion resistance is still a matter of debate: Xu and Hu showed that electrochemical activity increases with martensite content, causing a lower resistance against pitting corrosion. Further, they showed that passive films of cold deformed samples passivated in NaCl solution consist of a high amount of corrosion products like $CrCl_3$ and $Cr(OH)_3$ as well as $Fe(OH)_3$ instead of mainly Fe_2O_3 and Cr_2O_3 which forms in passive films of undeformed samples and show better protection [104]. Wang et al. also discovered a Cr_2O_3 rich passive film for untreated austenitic samples and a $Cr(OH)_3$ rich film for deformed, martensitic samples [105]. In the case of nitrogen stainless steel, Fu et al. observed an increase of hydrogen species in contrast to chromium oxides in the passive layer [106], which leads to a less protective passive film and can be at least partially attributed to the formation of martensite. While the effect of an increasing martensite phase on pitting corrosion was shown, its effect on the passive layer by crystal lattice distortion as well as its impact on general surface corrosion is still subject to debate.

In a recent study, Solomon et al. argued deformation-induced martensite transformation of stainless steel leads to flaws in the microstructure which cause the passive film to rupture [107]. Zhang et al. investigated the corrosion properties of differently treated low-alloyed steel and could show that tempered martensite showed a higher corrosion rate compared to ferrite-bainite steel. They attributed this behavior to the higher amount of carbides formed in the martensitic steel assuming that the carbides might act as cathodic sites and accelerate the overall reactions [108]. All these reports rely on single samples with multiple changes of material characteristics during treatment, rather than on systematic variations of crystalline structure alone.

Recently, He et al. produced steel with various martensite contents (0.6%, 6%, 12% and 20%) by hot rolling. They found that pitting potential and passive film resistance decreases

with martensite content up to 6%. With even higher martensite content the pitting potential and film resistance increases as well [109]. However, in addition to the phase transformation from austenite to martensite the hot rolling process leads to a change in grain size and dislocation density. Thus, the changes of electrochemical properties cannot be addressed to the martensite content alone.

Other studies on the impact of material deformation on the corrosion resistance also confirmed that these processes lead to several microstructure changes. Luo *et al.* observed decreasing grain size and changing grain boundary properties (disappearing twin boundaries and more low angle boundaries and increasing ΣCSL boundaries) next to increasing martensite content with increasing degree of deformation. They observed decreasing corrosion resistance with increasing degree of deformation but where not able to attribute this behavior to one microstructure parameter [110].

As explained above, it is absolutely necessary to take these additional microstructure changes into account. Grain size and grain boundary properties as well as dislocation densities can have a strong effect on the passive layer and might compensate each other. The underlying principles, however, of the martensite impact on the corrosion behaviour remain unclear.

5.1.2.2 Influence of grain size on corrosion

The effect of grain size of coarse grained material is also controversially discussed. Ralston discussed this topic extensively in his review on the effect of grainsize on corrosion. He concluded that a passivating environment supports the passivity of small grained material due to the enhanced electrochemical activity at the grain boundaries and a faster passive film growth. On the other hand, he stated that in a non-passivating environment the corrosion of coarse grained material is inhibited due to the slower dissolution at the grain interior surface [94]. The role of the environment seems to be a crucial factor regarding the effect of grain size on corrosion. Nevertheless, controversial results are found even in the same environment. While Abbasi *et al.* could not observe an effect on the pitting potential of stainless steel in chloride containing electrolyte [111] Jinlong *et al.* observed a clearly increased pitting potential for samples with ultra-fine grains [112]. In different environments completely contrary behavior can be observed: Fattah-Alhosseini et al. recognized worse passivation of fine grained material in 0.1 M HNO_3 solution due to a higher amount of defects [78] whereas Jinlong et al. came to the conclusion that grain refinement leads to a more protective passive film in 0.1 M NaCl solution [112]. Just like in case of the investigations on the influence of martensite on the corrosion behavior a difficult point in studies about the effect of grain size is to isolate the grain size effect from other microstructure changes that are caused by the material processing [94].

This selection of scientific publications illustrates the contradictions and difficulties of the

investigations of heat treatments on the corrosion resistance. Slightly different materials can show drastically different behavior. Small variations of the treatment can lead to completely new effects.

However, the greatest difficulty is the complexity of the effects of the material treatments. Not one single microstructure parameter is varied during austenitizing but several are affected in their own way. The variation of the austenitizing temperature leads to grain growth, phase changes and carbide dissolution, which all affect the corrosion behavior. Sometimes the explanations of the different effects on the corrosion behavior and the passive film formation are more of a speculative nature, as in the case of the influence of grain size on corrosion [94] or if and why the lattice distortion accelerates the corrosion attack.

To address these contradictions and to find a physical explanation for the observed phenomena comprehensive electrochemical studies of the effect of systematically changed heat treatments are combined with modeling of the passive film growth. The combination of electrochemical measurements and the kinetic model of oxide film growth allows to determine kinetic parameters of corrosion and passive film growth. These parameters are able to deliver a physical explanation for the influence of single microstructure changes on the corrosion behavior.

At first the extensive and yet contrary studied effects of austenitizing on martensitic stainless steel are investigated by this method. In the next step, the heat treatment is carried out on another material to verify the transferability of the method. In the last experimental and theoretical investigation series a single microstructure parameter, the martensite content, is changed to isolate the influence of the phase content.

6

AUSTENITIZING OF MARTENSITIC STAINLESS STEEL[3]

In the previous chapter, the contrary results of different publications on the effect of austenitizing temperature on the corrosion behavior of martensitic steel have been discussed. The authors of the cited publications addressed their observations on the dissolution of carbides, which lead to increasing lattice distortions and thus to accelerated mass loss due to corrosion, on the one hand [1] or which lead to increasing chromium content in the metal matrix which can enhance the passivation, on the other hand [2]. The experimental procedure cannot be compared conclusively and the physical cause of accelerated mass loss due to lattice distortions is not clear.

To overcome these contradictions and to clarify the effects of heat treatment, electrochemical corrosion tests are performed on similar heat treated martensitic stainless steel. These

[3] Parts of this chapter have been published verbatim in *AIP Advances* **9** (2019) [14] and *Corros. Mater. Degrad.*1 (2020) [15]

tests are evaluated with regard to different corrosion mechanisms and compared with extensive microstructure analyzes. Finally, the passive behavior of the material – ultimately responsible for the corrosion behavior – is investigated via EIS measurement based parameterization of the PDM. The constants determined in this way should give an insight into the physical process that lead to the altered corrosion behavior.

6.1 METHODS

The used Methods for material treatment, microstructure investigations and electrochemical measurements are described in the following section.

6.1.1 MATERIAL

The stainless steel X46Cr13 (material code number 1.4043 according to DIN EN 10088-3, AISI 420) is investigated. As the alloy has been manufactured by vacuum melting in a laboratory at the Max Planck Institute for Iron Research GmbH (Düsseldorf, Germany), its composition differs from commercial engineering alloys. The aim is to examine pure material science mechanisms in a ternary Fe-C-Cr alloy. Therefore, the mass fractions of the elements manganese (Mn), phosphorus (P), sulfur (S) and silicon (Si) are explicitly far below the upper limit according to DIN EN 10088-3. The wet chemical analysis of the element distribution is given in Table 6-1. The basic components of the ternary system (Fe, C, Cr) are in range. The value of the carbon content, being near the upper limit, has a positive effect on the hardenability.

6.1.2 HEAT TREATMENT

The heat treatments were done by the Leibniz-Institut für Werkstofforientierte Technologien – IWT (Leibniz-IWT) and applied in a two chamber Ipsen RVTC furnace under vacuum atmosphere. The austenitizing temperature T_A was varied from 1000 °C to 1200 °C to set different grain sizes in the cuboidal samples with a size of 25 x 37 x 6 mm³, while the austenitizing time was two hours in each case (Table 6-2). The gas quenching was performed with nitrogen at eight bars.

Table 6-1: Element distribution of investigated stainless steel samples in wt.-%

Alloying Element	C	Cr	Fe	Mn	O	P	S	Si
Laboratory alloy	0.497	13.70	bal.	0.372	0.0033	0.0022	0.0031	0.0075

Table 6-2: Heat treatment parameters.

T_A in °C	1000	1050	1100	1150	1200
t_A in h			2		
Quenching			8 bar N_2		

6.1.3 Material Properties

The material properties have been investigated by the Leibniz-Institut für Werkstofforientierte Technologien – IWT.

6.1.3.1 Grain size

Each metallographic analysis was prepared by embedding, grinding with SiC paper and polishing in four steps with a last grit of 0.02 µm. The grain boundaries were etched with a mixture of 1.5 % picric acid, 10 drops of HCl and 0.9 g Sodium dodecylbenzenesulfonate.

The grain sizes were determined by a surface analysis according to European standard ISO 643 (American standard ASTM E112). The grain size index G is defined as m = 16 grains per mm² for G = 1 in equation

$$G = \frac{\log(m)}{\log(2)} - 3 \qquad 6\text{-}1$$

6.1.3.2 Hardness and phase ratio

The hardness measurement was carried out by Vickers HV1 method at a testing period of 15 s. The software package ThermoCalc (Thermo-Calc Software Inc.) was used to calculate the ratio of the phases and the amount of dissolved chromium.

6.1.3.3 XRD measurements

Quantitative phase analysis [113] was performed using Cr-radiation ($K_{\alpha 1,\alpha 2}$), produced by a long fine focus tube 12×0.4 (Panalytical). Diffracted radiation was detected by a position sensitive detector "Miostar 2" (Photron-X, Ottobrunn, Germany), equipped with a vanadium filter. The measurements were performed on the outer surface of the sample, using a fox-mini-lens (IFG, Berlin, Germany), with an incident beam diameter of 200 µm. All the diffraction profiles were obtained by varying 2θ from 60° to 164° with a resolution of 0.05°.

The collected XRD data was refined by use of the Rietveld method [114], using the software TOPAS 4.2 (Bruker AXS, Karlsruhe, Germany). In this method, the whole measured pattern is refined with a calculated pattern, taking into account the instrumental contributions and the crystal structure of the present phases, including microstructural features like

crystallite size and microstrains. The calculated criterion residuals weighted profile (weighted R-factor; R_{wp}) gives a reliable information about the fit quality. Thereby, the smallest R_{wp} value represents the best refinement. It is calculated by:

$$R_{\mathrm{wp}} = \sqrt{\frac{\sum U_i (Y_i obs - Y_i calc)^2}{\sum (Y_i calc)^2}} \qquad 6\text{-}2$$

In this equation $Y_i obs$ is the measured and $Y_i calc$ the calculated intensity at each 2θ position i [114].

The goodness of the XRD measurement is determined by weighted R-factors R_{wp}. A low R_{wp} indicates a good agreement, while the value should aim against 1. However, a R_{wp} below 7 already indicates a good agreement between calculated and obtained data. Further, the precision of the quantitative analysis of the phase contents is estimated to be around ± 5 wt.-% in the present case.

6.1.4 ELECTROCHEMISTRY

All electrochemical measurements were carried out in a standard three electrode cell using a Metrohm Autolab potentiostat with the PGSTAT204 and the FRA32 modules. All experiments were performed at room temperature. A platin electrode served as counter electrode and an Ag/AgCl electrode as reference electrode, while the investigated material acts as the working electrode. The samples were embedded with two component adhesive in a PVC holder. All potentials in this chapter are referred to the Ag/AgCl electrode.

The LSV measurements were done in phosphate buffered saline (PBS) containing 0.1 M NaCl + 0.1 M phosphate buffer solution (pH = 7.5). This electrolyte allows the investigation of a broad passive range and leads to a broadening of corrosion potentials (compare Section A1) [115]. The polarization scans were performed with a scan rate of 1 mV/s. Each polarization scan started from -1100 mV and ended at 200 mV.

Characteristic values are derived from the potentiodynamic polarization scans: the corrosion current density i_{cor} via Tafel method by the intersection of the Tafel extrapolations and the corrosion potential E_{cor} at which anodic and cathodic (and capacitive) current densities are in equilibrium. The passive current density i_{pas} was measured in the passive region of the current-potential curve at -200 mV and the pitting potential E_{pit} was determined by the potential at which stable pit growth occurs. The critical potential E_{crit} can be observed at the potential at which the current density exceeds a given value (10 μAcm^{-2} comparable to [98]) (compare Section A2).

EIS measurements to parametrize the PDM were carried out in sulfuric acid due to a well-known passive behavior in this medium [116]. The impedance measurements are carried out

in a frequency range of $10^{-2} - 10^{5}$Hz at a DC potential of 0.6 V after polarization for 1800 s. The effect of the electrolyte is represented in the PDM by the influence of pH and an additional constant. This constant is summarized in the standard rate constant (compare Chapter 4). A change of electrolyte only leads to an even offset of this constant. The electrical field strength inside the passive film is assumed to be 10^{6} V/cm [89].

Before each measurement, the working electrodes were wet grinded with SiC grinding paper (60 grid), degreased in ethanol, and cleaned in an ultrasonic bath containing deionized water. A determination of the influence of sample pretreatment is presented in Section A3.

6.2 Experimental Results and Discussion

The results of the metallographic analysis done by Leibniz - IWT and of the electrochemical experiments are presented in the following chapter. Subsequently the results of the passive film growth kinetics fitting are given and discussed regarding the findings of the material scientific and electrochemical measurements.

6.2.1 Microstructure and Mechanical Properties

6.2.1.1 Grain size

An austenitizing temperature of 1000 °C caused a microstructure with a general grain size index of 10.9. At 1050 °C a mixed grain size microstructure with a ratio of 70 % coarse grains occurs. With increasing temperature, the grain size index of the coarse part of the microstructure is clearly decreasing, thus the grain size itself is rising from 6.7 µm at 1000 °C to 218.3 µm at 1200 °C. The grain size of the fine part, whose fraction is becoming less than 5 % at 1150 °C, is increasing from 3.5 µm at 1050 °C to 6.1 µm at 1150 °C. At an austenitizing temperature of 1200 °C fine grains are not existing anymore. The huge grains grew at the expense of the fine ones (Figure 6-1).

6.2.1.2 Hardness

The hardness values are characteristic for a martensitic microstructure. With increasing austenitizing temperature, the hardness is rising from 648 HV1 (for 1000 °) to 754 HV1 after an austenitization at 1100 °C due to the increasing amount of dissolved carbon and chromium in the lattice matrix. Thus, a higher ratio of dissolved carbides causes a higher effect of strengthening.

If T_A is increasing further, no more elements are dissolved and phase transformation into austenite has been completed. Therefore, the effect of grain growth is probably predominating and the hardness values for 1150 and 1200 °C sink slightly (Figure 6-2).

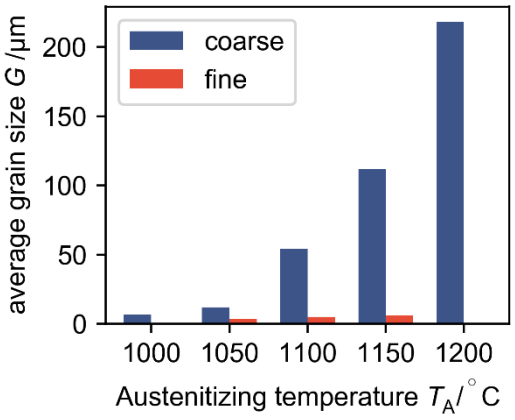

Figure 6-1: Increase of grain size depending on the austenitizing temperature.

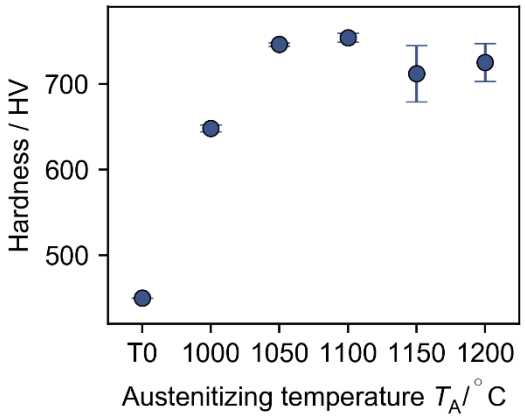

Figure 6-2: Hardness depending on the austenitizing temperature.

6.2.1.3 Phases/carbides/chromium content

As the present phases in high-alloy steels transform with varying austenitizing temperatures, the amount of chromium carbides must be considered for each T_A. It should be noted that ThermoCalc calculations are based on the assumption of equilibrium conditions. After 2 hours of austenitizing, all carbides that dissolve at the given temperature are dissolved. Considering this, the phases should be in equilibrium, but as the diffusion of chromium atoms is slow, a complete homogenization is not given, even after hours.

At austenitizing temperatures of 1000 °C to 1200 °C carbides of stoichiometric type $Cr_{23}C_6$ do not exist. $Cr_{23}C_6$ carbides are completely dissolved in the matrix above temperatures of approx. 930 °C. In contrast, Cr_7C_3 carbides are still present because they dissolve at higher temperatures [92]. This leads to a lower amount of dissolved chromium at lower austenitizing temperatures. At $T_A = 1150\,°C$ and $1200\,°C$ the microstructure is austenitized completely, so 13.7 % chromium is dissolved (Table 6-3).

The XRD results of the samples are shown in Figure 6-3. Based on the location, the $\alpha(011)$, $\alpha(002)$ and the $\alpha(211)$ peaks are the only visible diffraction peaks. All heat treated samples show a clear martensitic diffraction pattern and no significant austenite phase. The α phase of the untreated sample indicates ferritic crystal structure. Intensity variations are, among other reasons, attributable to the variation in the former austenite grain size.

6.2.2 Electrochemical Properties

Austenitizing of stainless steel results in different microstructure changes, namely the release of chromiuim from carbides to the alloy matrix, the release of carbon to the alloy matrix and the growth of grains. The right choice of cooling phase after austenitizing leads to martensite microstructure which shows significant improvements in hardness.

Table 6-3: Calculated amount of austenite phase and mass ratio of dissolved chromium for each austenitizing temperature.

T_A / °C	Amount of austenite phase / ma.-%	Mass amount of dissolved Cr / ma.-%
1000	97.46	11.94
1050	98.44	12.65
1100	99.60	13.45
1150	99.97	13.69
1200	99.97	13.69

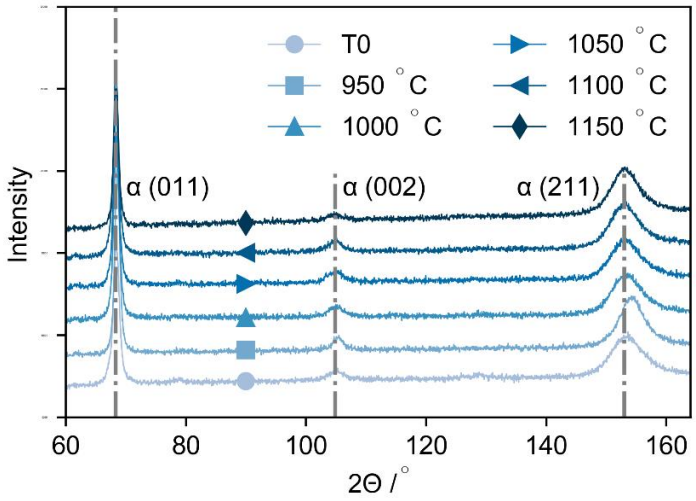

Figure 6-3: X-ray diffraction pattern for martensitic stainless steel samples with different heat treatment.

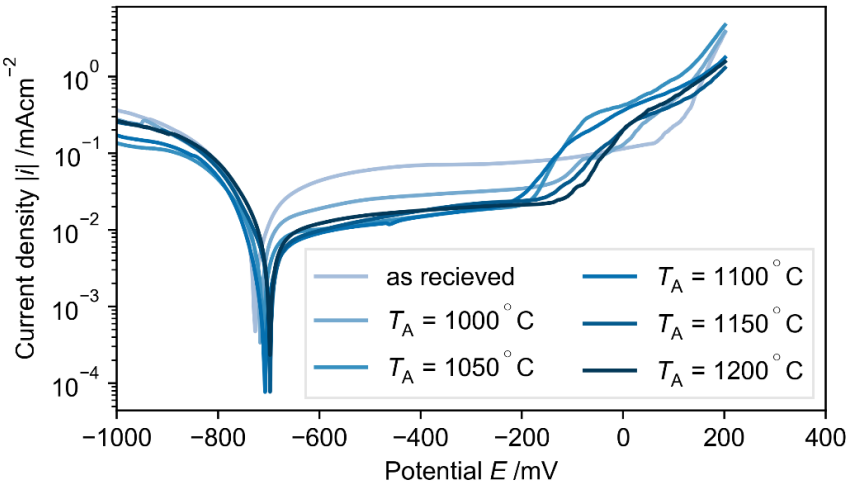

Figure 6-4: LSV measurements of martensitic stainless steel after austenitizing at different temperatures in 0.1 M phosphate buffered saline; Scan rate: 1 mVs^{-1}.

The release of chromium can also improve the passive behavior since there is more chromium available to form a chrome rich passive layer. The release of carbon can have negative effects on the passive behavior because a high carbon content can result in internal lattice stress. The effect of an increased grain size is currently intensively discussed: It was shown that nano crystalline grain size can improve the passive layer and corrosion resistance [112,117]. On the contrary, it was also observed that smaller grains can decrease the resistance against pitting corrosion [118] or lead to a defect richer passive film. However, the results depend strongly on the experimental conditions, like the choice of the electrolyte, the material compositions and especially on the investigated corrosion mechanisms.

To distinguish the different corrosion mechanisms and investigate the influence of the different microstructure changes on the single mechanism, potentiodynamic polarization scans in 0.1 M phosphate buffered saline have been performed. By choice of this electrolyte it is possible to observe the passive bahavior as well as the pitting corrosion and the steady state corrosion rate [115]. The polarization scans start with a cathodic current at -1100 mV followed by the corrosion potential between -740 mV and -680 mV. The subsequent passive region is characterized by a constant low current density, ending between -230 mV and 60 mV (depending on the austenitizing temperature), where stable pit growth starts (Figure 6-4).

The corrosion current density was evaluated via Tafel method (compare Section A2) and plotted over the austenitizing temperatures (Figure 6-5a). The corrosion current density i_{cor} decreases with increasing austenitizing temperatures and thus increasing chromium content. For austenitizing temperatures above 1100 °C the corrosion current density slightly decreases, which seems to be a result of the increasing grain size. The same course could be observed for the passive current density (Figure 6-5b). A decreasing corrosion current, as well as a decreasing passive current, indicate a better passivation against general corrosion. The increasing austenitizing temperature leads to an increasing chromium content in the alloy matrix and thus a better resistance against general corrosion.

The pitting potential E_{pit} – the potential at which stable pit growth occurs – decreases with increasing austenitizing temperatures (up to 1100°C), indicating a higher susceptibility to pitting corrosion (Figure 6-5c). With further increase of the austenitizing temperatures, the potential increases again.

In contrast to this observation, the critical potential E_{crit} – the potential at which a critical current density (10 µAcm^{-2} - comparable to [2]) is exceeded – increases with increasing austenitizing temperature (Figure 6-5d), indicating a higher corrosion rate if pitting occurs. At austenitizing temperatures over 1100 °C E_{crit} decreases again.

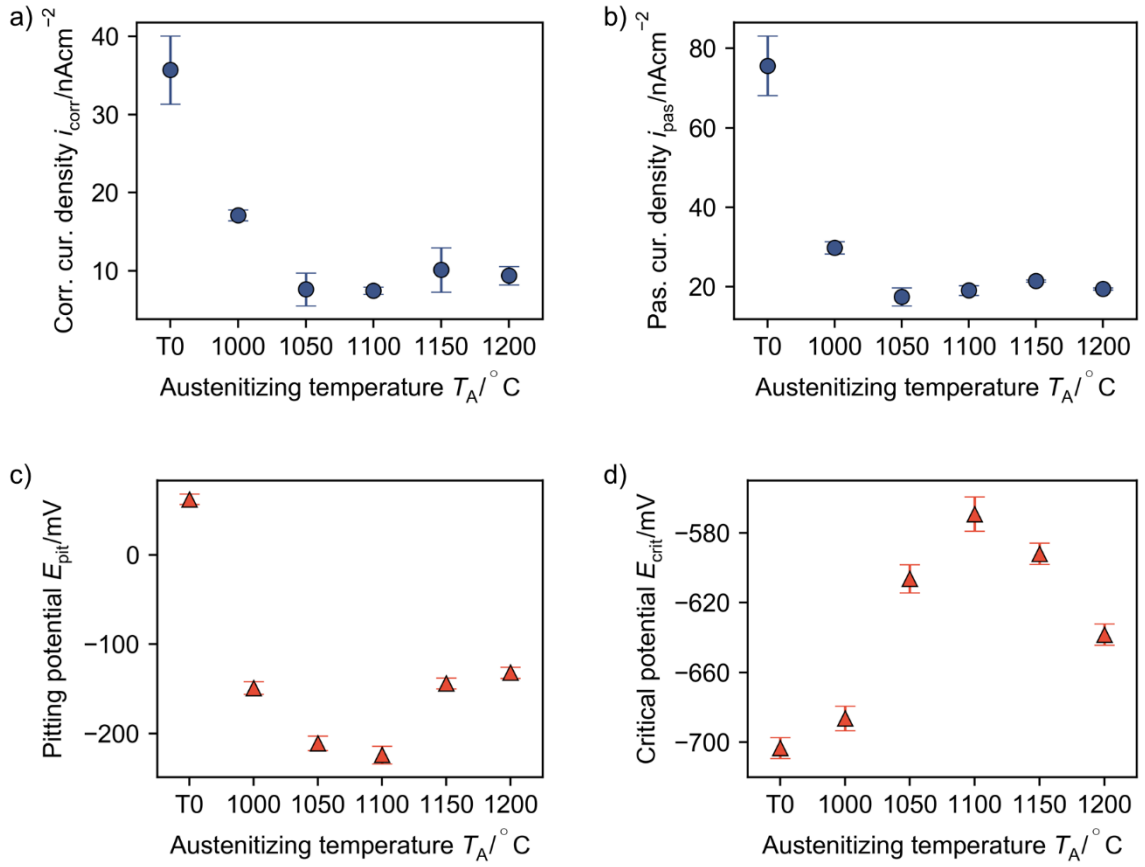

Figure 6-5: Dependencies of different corrosion parameters on the heat treatment. a) corrosion current densities b) passive current densities c) pitting potential d) critical potential. Standard deviations are in some cases smaller than the marker size. Each standard deviation is calculated by at least three independent measurements.

While corrosion current densities correlate with corrosion rates during general corrosion under steady state, the passive current density gives information about the passive layer stability. The general corrosion rate decreases with increasing austenitizing temperatures because more chromium is released in the alloy matrix and is available for the formation of the passive layer. The same effect is visible for the passive current density. A higher chrome content seems to improve the chromium rich passive layer on top of the bulk material.

An opposite trend is recognizable in case of the pitting corrosion resistance. The pitting potential decreases with increasing austenitizing temperatures (for sample T0 and T = 1000 °C – 1100 °C) because of an increase of internal lattice stress, due to higher carbon content. A further increase of the austenitizing temperatures (1150 °C and 1200 °C) does not increase the carbon content, since all carbides are dissolved; instead, it enhances the grain size. With increasing grain size, lattice defects due to grain boundaries decrease and the material shows less starting points for pitting corrosion and a higher E_{pit}.

So far, this investigations have confirmed both an increase of corrosion resistance regarding the steady state and the passivated state (lower i_{cor} and i_{pas}), and a decrease of corrosion resistance regarding the possibility of passive film failure due to pitting corrosion (lower E_{pit}). This leads to the conclusion that the phenomena described in literature address different corrosion mechanisms. This differing corrosion mechanism seems to be affected by different microstructure properties. In order to reveal the influence on passive film growth and to study the physical causes behind the observed phenomena, impedance measurements to fit the kinetic parameter of passive film growth are performed next.

6.3 Passive Film Growth Kinetics

The Nyquist plots of the impedance data of the 6 different samples (Figure 6-6) reveals clear differences between the samples. The lowest overall impedance can be seen in case of the untreated sample (T0) (Figure 6-6a). Up to a value of T_A = 1100°C, the overall impedance monotonically increases with austenitizing temperatures. For T_A = 1150 °C, the impedance decreases compared to the lower temperatures but a further increase in temperature increases the impedance again, so the maximum is reached at T_A = 1200 °C (Figure 6-6b).

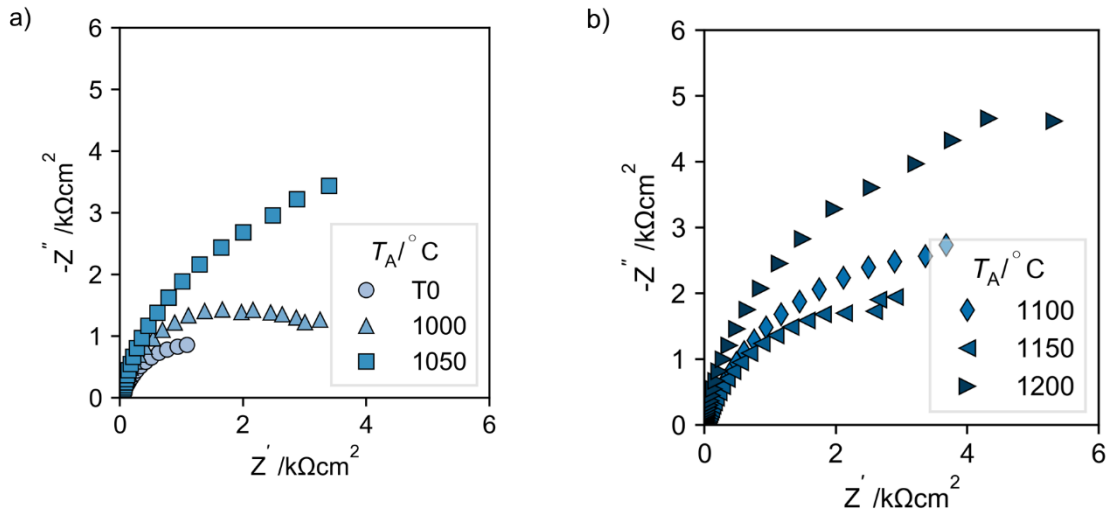

Figure 6-6: Nyquist plots of martensitic stainless steel; untreated sample (T0) and samples treated at different austenitizing temperatures T_A recorded in 0.5 M H2SO4. (a) T0, 1000 °C and 1050 °C (b) 1100 °C, 1150 °C and 1200 °C.

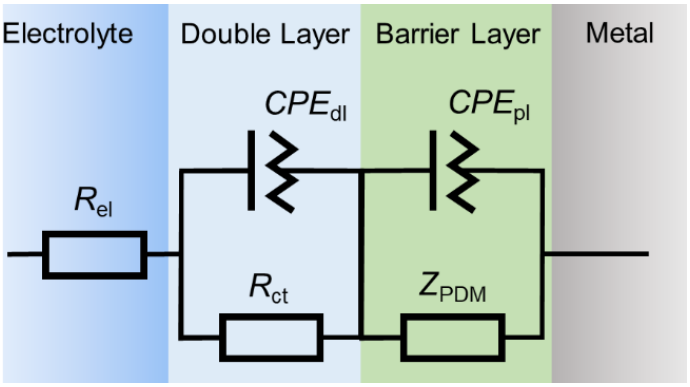

Figure 6-7: Equivalent electrical circuit to fit the impedance data. R_{el}: electrolyte resistance, CPE_{dl}: CPE representing the double layer, CPE_{pl}: CPE representing the passive layer, R_{ct}: charge transfer resistance, Z_{PDM}: faradaic impedance due to the reactions on the metal–film and film-solution interface described by the point defect model.

The fitting of the impedance data can be done by the equivalent electrical (EEC) circuit presented in Figure 6-7. The EEC consists of an electrolyte resistance R_{el}, a charge transfer resistance R_{ct}, a CPE for the double layer (and/or the outer layer) CPE_{dl}, a CPE representing the capacitive behavior of the passive layer CPE_{pl}, and an impedance element describing the interfacial reactions predicted by the PDM Z_{PDM}. The PDM calculations show good agreement with the measurements (Figure 6-8). The reaction coefficients for passive film growth (Reaction 2) and passive film dissolution (Reaction 7), as well as the charge transfer coefficient α_2 for the film growth reaction and the passive film thickness L_{ss} are shown in Table 6-4. The CPE parameters describing the double layer lie between 2.01×10^{-4} and $5.71 \times 10^{-4}\ \Omega^{-1}\mathrm{cm}^{-2}s^{N}$ for Y_{CPE} and 0.86 and 0.97 for N and are presented in Section A6.

The crucial factor for the steady state film thickness is the ratio k_2^0/k_7 The higher the ratio the thicker the passive film; whereas the same ratio, which is achieved at higher rate constants, leads to the same film thickness but accelerated dissolution (for similar α values) thereby approaching the steady state faster. An increasing α_2 value leads to thinning of the passive film at slightly less dissolution (assumed k_2^0 and k_7' remain constant).

Table 6-4: Fitted kinetic parameters for all martensitic stainless steel samples.

T_A/°C	k_2^0 / mol/(cm²s)	α_2	k_7' / mol/(cm²s)	L_{ss} / nm
T0	9.61×10⁻¹¹	0.0247	3.60×10⁻¹⁰	1.50
1000	5.91×10⁻¹¹	0.0298	3.09×10⁻¹⁰	1.32
1050	3.68×10⁻¹¹	0.0282	1.92×10⁻¹⁰	1.07
1100	1.80×10⁻¹¹	0.0353	1.38×10⁻¹⁰	1.16
1150	2.69×10⁻¹¹	0.0368	2.66×10⁻¹⁰	0.76
1200	9.46×10⁻¹²	0.0352	8.44×10⁻¹¹	0.77

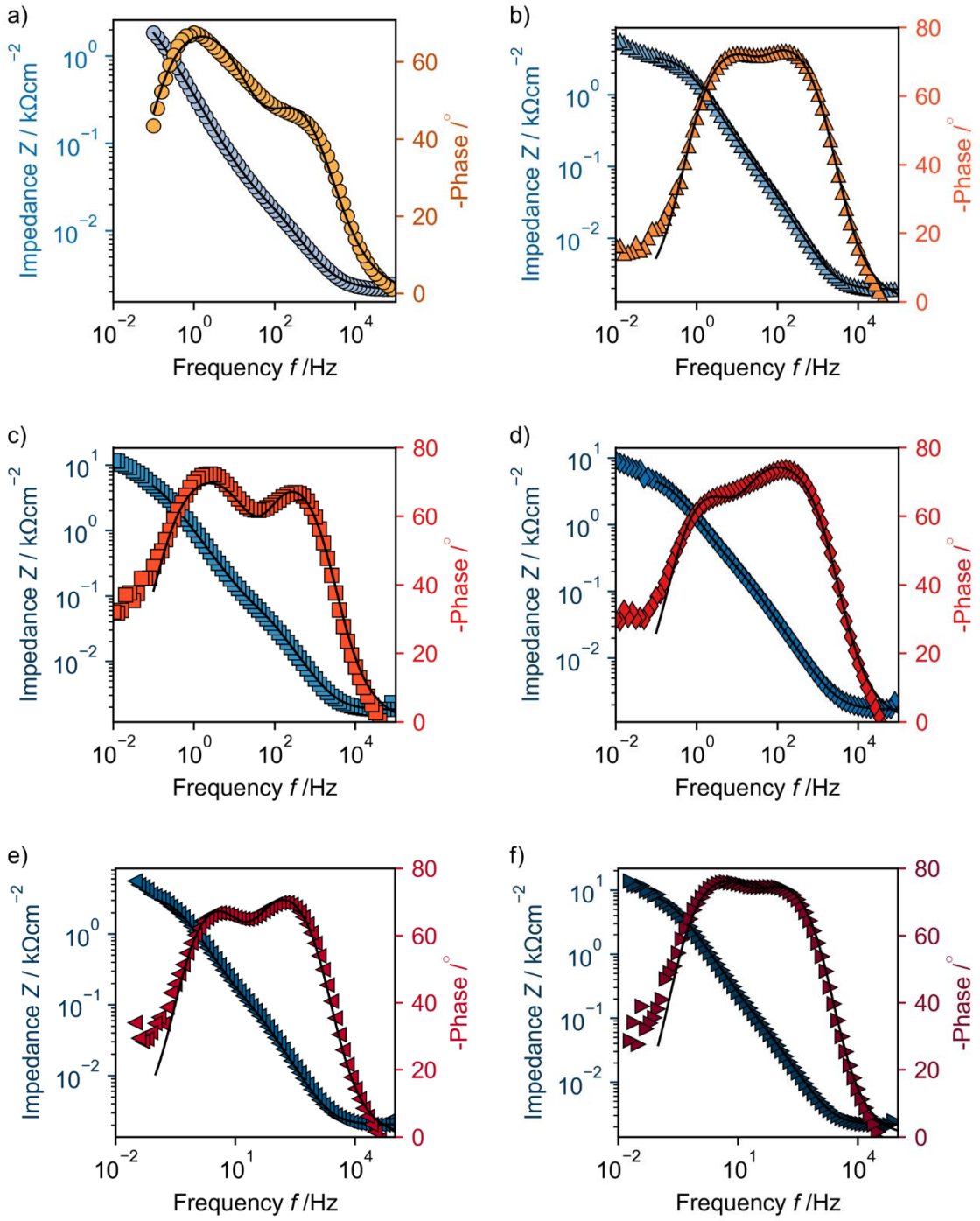

Figure 6-8: Bode plots of the impedance data of martensitic stainless steel recorded in 0.5 M H_2SO_4; untreated sample (T0) and samples treated at different austenitizing temperatures. Symbols show experimental data whereas black lines represent the calculation using the EEC and PDM. (a) T0 untreated sample (b) 1000 °C (c) 1050 °C (d) 1100 °C (e) 1150 °C (f) 1200 °C.

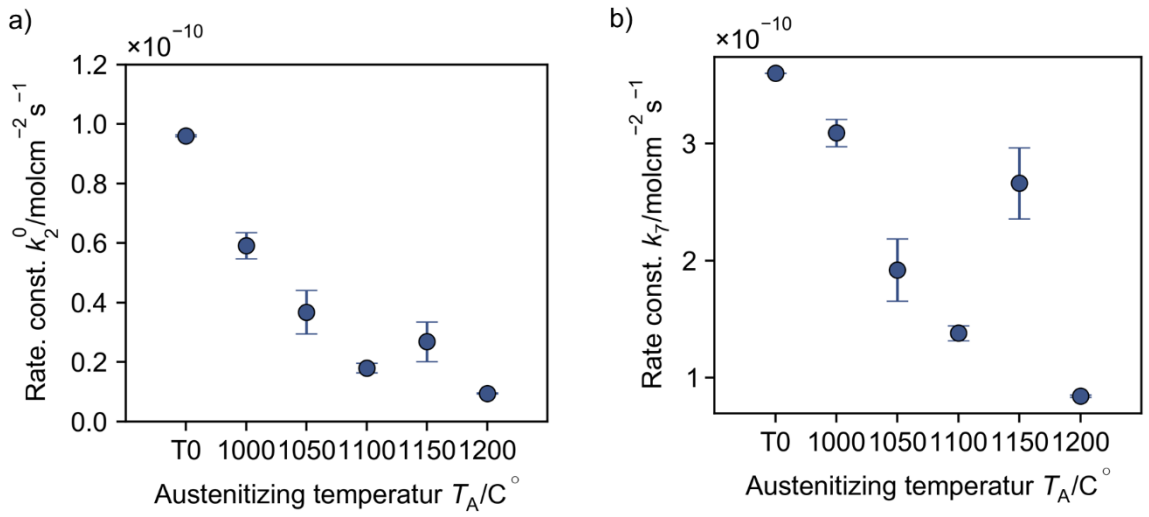

Figure 6-9: Rate constants of film formation k_2^0 and film dissolution k_7 calculated by fitting the impedance data via PDM and EEC presented in Figure 6-7. Error bars represent standard deviations of 3 independent measurements. (a) Rate constant for film formation (b) rate constant for film dissolution.

Generally, with increasing austenitizing temperature, the charge transfer coefficient α_2 increases, the standard rate constant k_2^0 for film formation (Figure 6-9a) decreases, and the rate constant k_7 for film dissolution (Figure 6-9b) decreases. A decrease of k_2^0, which means decreasing metal dissolution at the metal-passive film interface, indicates a slower corrosion rate. Thus, samples with lower k_2^0 show a better passivation and lower reaction rates at the metal surface due to a more protective passive layer.

A further indicator for a more stable and protective passive film is the decreasing rate constant for film dissolution k_7. This behavior can be attributed to the higher amount of chromium at higher austenitizing temperature and a more homogeneous chromium distribution due to the higher diffusion at higher temperatures.

The increase of the charge transfer coefficient α_2 for film formation means a reduction of the activation energy for oxidation with increasing potential. This behavior seems to be contrary to the decrease of the rate constants.

However, the sample T_A = 1150 °C shows deviations from this trend by a slightly increased rate constant for film formation and a drastically increased rate constant for film dissolution leading to the thinnest passive film. This might be connected to the dissolution of Cr_7C_3 carbides [92], which on the one hand brings more chromium to the matrix but on the other hand leads to further lattice distortion due to the dissolved carbon. Taking the different stoichiometry of the carbides into account ($Cr_{23}C_6$ dissolving at 930 °C and Cr_7C_3 dissolving at 1150 °C) the ratio of dissolved carbon to dissolved chromium is higher at 1150 °C (Cr_7C_3) compared to the $Cr_{23}C_6$ carbides. This leads to higher lattice stress for the same amount of chromium and explains this behavior.

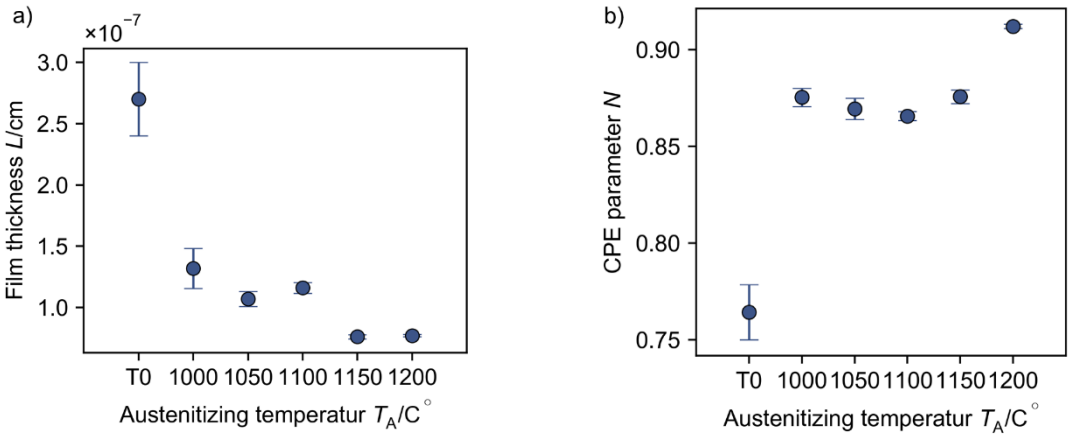

Figure 6-10: Passive layer characteristics obtained from impedance data analysis using the equivalent electrical circuit shown in Figure 8. (a) Passive film thickness *L*; (b) CPE parameter *N*.

One can further observe a thinning of the passive film with increasing austenitizing temperature (Figure 6-10a). The untreated sample shows the thickest passive film but also the lowest CPE parameter, $N = 0.76$ (Figure 6-10b), which indicates a less homogeneous layer [55]. Thus, the passive film thickness is not crucial for the protective effect of the passive layer in this case. Rather, a protective passive layer leads to a deceleration of metal dissolution at the metal–film interface and thus to a thinner but more protective film.

The simulation via the PDM shows a deviation from the impedance data for low frequencies (10^{-2} Hz). These differences could be because the model does not incorporate the transport of oxygen vacancies through the film. This vacancy transport from the metal/film interface towards the film/solution interface could be overcome by adding a Warburg impedance to the EEC [75] at the cost of at least one additional fitting parameter.

Fitting the passive film kinetics to the obtained impedance data provides a very good explanation for the observed dependency of corrosion resistance and austenitizing temperature [2]. Due to the higher chromium content and the more homogeneous chromium distribution, the passive film is more protective and thus slows down the dissolution of the metal (decreasing rate constant for film formation) and of the film itself (decreasing rate constant for film dissolution). The decrease of the standard rate constant of film formation k_2^0 (which is ca combination of the rate constant of the reactions $Fe \rightarrow Fe^{3+} + V_{\ddot{O}} + 3e^-$ and $Cr \rightarrow Cr^{3+} + V_{\ddot{O}} + 3e^-$ which are not distinguishable) indicates a lower potential energy of the non-oxidized metal for film formation. This is due to the more stable electrochemical behavior of the samples with a higher chromium content (due to higher carbide dissolution) (Figure 6-11a). The decreasing rate constant of film dissolution is due to the higher chromium content in the passive film itself and thus the slowed down dissolution. How the charge transfer coefficient influences the activation energy is presented in Figure 6-11.

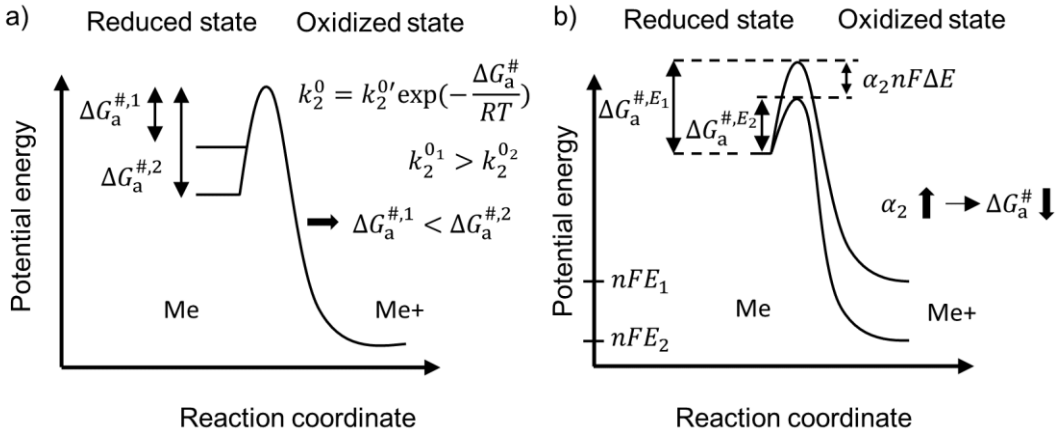

Figure 6-11: Potential energy of the redox system and influence of parameter changes. a) A lower potential energy of the reduced state leads to a higher activation energy, which finally results in a lower rate constant. b) A change of the potential from $\boldsymbol{E_1}$ to $\boldsymbol{E_2}$ about $\boldsymbol{\Delta E}$ leads to a change of activation energy $\boldsymbol{\Delta G_a^{\#}}$ about $\boldsymbol{\alpha_2 nF\Delta E}$. Thus, the higher $\boldsymbol{\alpha_2}$, the lower the activation energy $\boldsymbol{\Delta G_a^{\#}}$ regarding the potential change.

The results match with the findings of an increasing critical pitting potential, which indicates a slower dissolution by local corrosion attacks with increasing austenitizing temperature. Next to the increasing critical pitting potential the previous LSV measurements could reveal decreasing passive current densities and decreasing corrosion rates. The fitting delivers a clear explanation for this behavior due to the decreased film formation in the passive state.

On the other hand the above mentioned findings seem to be contradictory to the findings of Candelaria et al. [1] and the decreasing onset potential for pitting corrosion with increasing austenitizing temperature [14]. The presented fitting of the passive layer growth kinetics by the PDM provides detailed insight to the electrochemical behavior of the passivated samples. The phenomena investigated by Candelaria result from breakdown of passivity in the presence of halides. It is important to distinguish both mechanisms, the steady state metal loss due to growth of the passive film itself and the local corrosion attacks.

Nevertheless, it is possible to draw conclusions about the passive layer breakdown from the fitting parameter. The decreasing film thickness in combination with a decreasing film formation reaction (responsible for repassivation) can lead to earlier breakdown of the passive film through a film breakdown reaction. A detailed description of passive film breakdown is given in Chapter 9. Indeed, a combination of thin passive film and slow film formation can lead to an early breakdown of passivity, which is in accordance with Candelaria *et al.*

6.4 CONCLUSION

The effect of the austenitizing temperature on the corrosion resistance of martensitic stainless steel is a controversially discussed topic in material and corrosion science. To distinguish the effects of the different microstructure changes by different austenitizing temperatures on different corrosion mechanisms, polarization scans and impedance spectroscopy were performed. The results were correlated with microstructure changes and phase calculations.

The resistance against general corrosion increases with increasing austenitizing temperatures (up to 1100 °C) due to the dissolution of carbides and the related increase of chromium in the alloy matrix. Further increasing the austenitizing temperature does not increase the chromium content, since all carbides are dissolved and thus does not further increase the resistance against general corrosion.

On the other hand, an increasing austenitizing temperature not only leads to an increasing chromium content in the alloy matrix but an increasing carbon content. The additional amount of carbon results in internal lattice stress, which leads to a more defective passive layer. Thus increasing the austenitizing temperature (up to 1100 °C), decreases the resistance against pitting corrosion. Further increase of the austenitizing temperature has no effect on the carbon content but the grain size. With increasing grain size, the lattice defect density in the bulk material decreases, which leads to a less defective passive layer and thus a better resistance against pitting corrosion. By contrast, the critical potential shows a contradictory course and improves up to 1100 °C and decreases for lower temperatures.

The investigations could show that there is not one general corrosion resistance but several different corrosion mechanisms, which are influenced by different microstructure properties. Of special interest is the contrary trend of pitting potential E_{pit} and critical potential E_{crit}. In the previously discussed publications, no distinction was made in this regard – but a higher pitting potential means less susceptibility for pitting, while a higher critical pitting potential means slower pitting corrosion, if these occur (compare [1] and [98]). Additionally different alloyed steel has been compared to make generally statements but the amount of carbon is a critical factor for the pitting potential. It is not surprising that alloys with a lower carbon content show different pitting behavior (see also [4]). Taking this into account the apparently contradictory results just address different phenomena and are not a contradiction.

To investigate the physio-chemical mechanisms behind the observed phenomena, the PDM is fitted to impedance data of the samples. By modeling impedance data of high reproducibility by the PDM, it was possible to describe all data sets with good agreement and small standard deviations, which were clearly below 10 % in all cases. This agreement between calculation and data confirms that the PDM is sufficient to describe the kinetics of

these passive film growths and to compare the parameters of different materials regarding their passive behavior. Furthermore, it was found that austenitizing temperatures significantly influences all four kinetic parameters of passive film growth. More specifically, the standard rate constant for film formation and the rate constant for film dissolution decreases with increasing austenitizing temperatures indicating a lower potential energy of the metal phase. This leads to a better protection of the metal by slowing down the film growth and thus metal dissolution and a more stable passive film by reducing the dissolution rate of the film itself. Both phenomena can be addressed to an increasing amount of dissolved chromium and a more homogeneous chromium distribution.

On the other hand, the passive film is thinning with increasing austenitizing temperatures. This thinning of the passive film in combination with decreasing film formation constant, can lead to an earlier passivity breakdown due to pitting corrosion (compare Chapter 9).

The investigations could not only clarify the contradictions in literature but also address the different corrosion mechanisms to physio-chemical properties of the system. The next question is whether the findings can be transferred to another alloy system and are generally valid. In order to clarify this question, the same treatment was carried out on another alloy system and will be presented in the next chapter.

7

AUSTENITIZING OF BEARING STEEL

An experiment is a question which science poses to nature,
and a measurement is the recording of nature's answer
Max Planck

The influence of the austenitizing temperature on the corrosion mechanism of martensitic stainless steel was studied by electrochemical measurements and kinetic modeling of passive film growth in the previous chapter. It could be concluded that different microstructure changes result in contrary corrosion behavior. The dissolution of chromium carbides increased the chromium content in the metal, and thus, decreased the standard rate constant of film formation, lowering the potential energy of the metal phase and slowing down metal dissolution. Furthermore, increasing chromium content in the passive film decreases the dissolution of the protecting layer. On the other hand, the thinning passive layer could lead to a higher susceptibility for pitting corrosion. The search for a universal relation between the microstructure and passivity leads to our next experimental question: "Are the observed effects of microstructure on the growth kinetics transferable to different alloys?"

The austenitizing of bearing steel necessarily leads to some similar but also to different microstructure changes. The amount of chromium carbides is expected to be much lower compared to the martensitic stainless steel, whereas, the amount of carbon is significantly higher, leading to an enhanced formation of iron-carbides. A higher amount of carbon can also affect the phase distribution and results in mixed austenite-martensite phases.

To analyze the effects of austenitizing to this low alloyed steel comparable microstructure analysis and electrochemical measurements are performed. The results of the electrochemical measurements are interpreted regarding the microstructure analysis and, in a next step, the passive film kinetics are fitted to impedance measurements in sulfuric acid.

7.1 METHOD

The used methods for material treatment, microstructure investigations and electrochemical measurements are described in the following section.

7.1.1 MATERIAL

The investigated steel is the bearing steel AISI 52100. This steel is not classified as a stainless steel due to its low chromium content. This might be the reason why there are several studies on the impact of heat treatment on the mechanical properties [98-101] but not on the corrosion behavior. Hardening via austenitizing is a very common process to adjust the mechanical properties of a material in order to fulfil the requirements of a specific application [119]. The steel samples investigated in this chapter are cut from an industrial alloy with a composition listed in Table 7-1.

7.1.2 HEAT TREATMENT

The heat treatments were done by Leibniz - IWT and are similar to the treatment of the martensitic steel samples but for a shorter time. The treatments were applied in a two chamber Ipsen RVTC furnace in vacuum atmosphere. The austenitizing temperature T_A was varied from 800 °C to 1150 °C to control the grain sizes and martensite contents in the cuboidal samples with a size of 25 x 37 x 6 mm³. The austenitizing time was one hour in each case (Table 7-2). The gas quenching was performed with nitrogen at eight bars.

Table 7-1: Element distribution of investigated stainless steel samples in wt.-%

Element	C	Cr	Fe	Mn	Mo	P	S	Si
Min.	0.93	1.35	bal.	0.25	-	-	-	0.15
Max.	1.05	1.6		0.45	0.1	0.025	0.015	0.35

Table 7-2: Heat treatment parameters

T_A in °C	800	850	900	950	1050	1100	1150
t_A in h			1				
Quenching			8 bar N_2				

7.1.3 Material Properties

The analysis of material properties, specifically the determination of grain size, hardness and crystallite structure by XRD measurements, is done analogously to the procedure presented in Section 6.1.3.

7.1.4 Electrochemistry

All electrochemical measurements were carried out in a standard three electrode cell using a Metrohm Autolab potentiostat with PGSTAT204 and FRA32 modules. All experiments were performed at room temperature. As counter electrode served a platin electrode and as reference electrode an Ag/AgCl electrode, while the investigated material acted as the working electrode. The samples were embedded with two component adhesives in a PVC holder. All potentials in this chapter are referred to the Ag/AgCl electrode.

The LSV measurements were done in phosphate buffered saline (PBS) containing 0.1 M NaCl + 0.1 M phosphate buffer solution (pH = 7.5) (compare Section A1). The polarization scans were performed with a scan rate of 1 mV/s. Each polarization scan started at a potential of -800 mV and ended at 200 mV.

Two characteristic values were derived from the potentiodynamic polarization scans: The passive current density i_{pas}, which was measured in the passive region of the current-potential curve at -200 mV and the pitting potential E_{pit}, which was determined by the potential at which stable pit growth occurred (compare Section A2).

EIS measurements to parametrize the PDM were carried out in sulfuric acid due to a well-known passive behavior and a clear pronounced passive region in this medium [116]. The impedance measurements were carried out in a frequency range of $10^{-2} - 10^{5}$ Hz at a DC potential of 0.8 V, 0.9 V and 1.0 V after polarization for up to 14400 s. The effect of the electrolyte is represented in the PDM by the influence of pH and an additional constant. This constant is summarized in the standard rate constant (compare Section 4). Changing the electrolyte only leads to an even offset of this constant. The electric field strength inside the passive film was assumed to be 3.9×10^{6} V/cm, which is comparable to the field strength inside the passive film on iron [120].

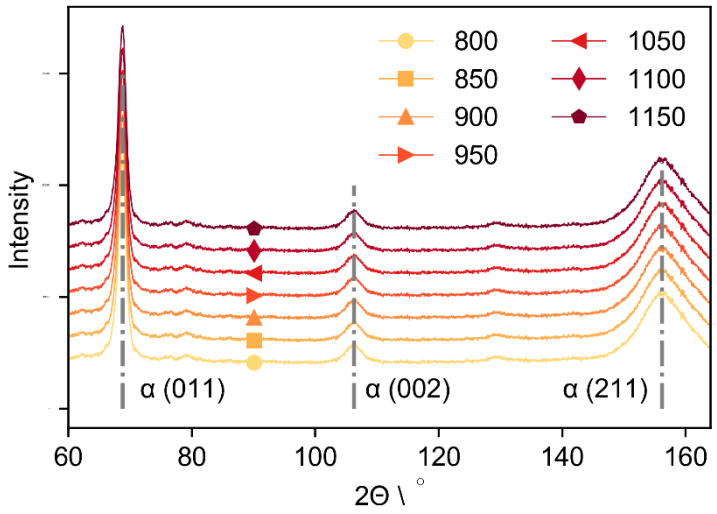

Figure 7-1: X-ray diffraction pattern for bearing steel samples with different heat treatment.

Before each measurement the working electrodes were wet grinded with SiC grinding paper (60 grid), degreased in ethanol, and cleaned in an ultrasonic bath containing deionized water. A determination of the influence of sample pretreatment is presented in Section A3.

7.2 Experimental Results and Discussion

The results of the metallographic analysis and of the electrochemical experiments are presented in the following chapter. Subsequently the results of the passive film growth kinetics fitting are given and discussed regarding the findings of the material scientific and electrochemical measurements.

7.2.1 Microstructure and Mechanical Properties

XRD measurements of the heat-treated samples reveal a martensitic-austenitic phase structure (Figure 7-1). Fitting of the intensity pattern shows a decreasing martensite content with increasing austenitizing temperature (Figure 7-2). However, the course of martensite versus temperature is not steady and shows some deviations of the expected course (compare [100]: increasing austenite content, so decreasing martensite content, with increasing temperature). Measurements of the hardness show a similar trend compared to the martensite content (Figure 7-3) with some deviations. This indicates that the hardness is not only affected by the martensite content.

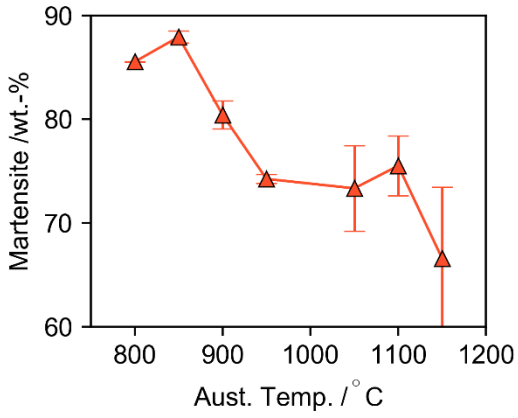

Figure 7-2: Martensite content of the samples due to the performed heat treatment at different austenitizing temperatures.

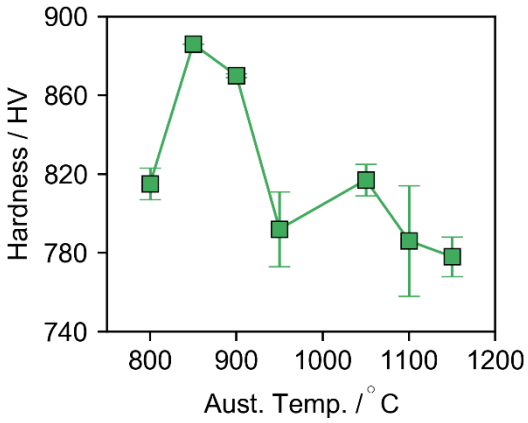

Figure 7-3: Hardness determined for different heat treated samples.

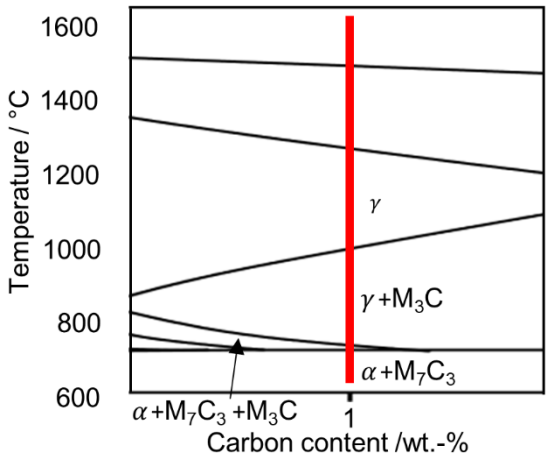

Figure 7-4: Extract from the ternary phase diagram of the Fe-Cr-C system at 2 wt.-% chromium**;** S: melt, $\boldsymbol{\gamma}$: $\boldsymbol{\gamma}$-austenite; reproduced from [92]

Figure 7-4 shows the ternary phase diagram, discussed in Chapter 5, of an iron-carbon-chromium alloy with a chromium content of 2 wt.-%. Due to the small deviation of the chromium content and additional alloying elements, the phase diagram of the investigated samples might slightly deviate of the presented one. Nevertheless, the important turnover points are similar. Following an increasing temperature at ca. 1 wt.-% carbon, a phase change at ca. 800 °C and 1000 °C is recognizable.

At ca. 800 °C the dissolution of M_7C_3carbides and at 1000 °C the dissolution of M_3C carbides occur. The dissolution of the M_7C_3 carbides increases the hardness at 850 °C drastically compared to a heat treatment at 800 °C due to the higher amount of carbon atoms stored in the lattice structure. The dissolution of M_3C carbides increases the hardness at 1050 °C even though the martensite content decreases. An additional factor next to martensite content and

carbide dissolution affecting the hardness is the grain size. Larger grain sizes are found with higher austenitizing temperatures (Figure 7-5) and have been reported to show a negative effect on the hardness. [33].

7.2.2 Electrochemical Properties

Linear sweep voltammetry measurements of all samples were performed and the characteristic values - passive current density and pitting potential - are compared. The course of all LSV measurements is qualitatively similar starting with a cathodic current at -800 mV. The current turns over to an anodic current at the corrosion potential between -750 mV and -630 mV.

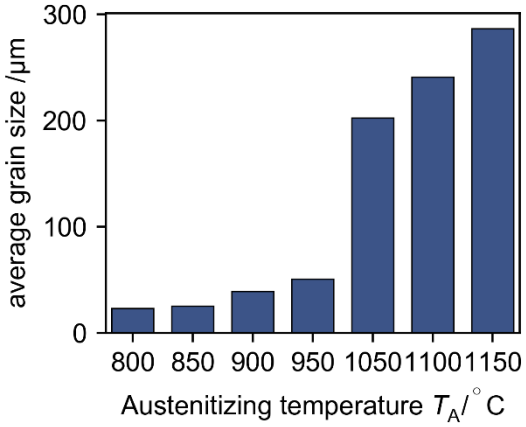

Figure 7-5: Increase of the average grain size depending on the austenitizing temperature.

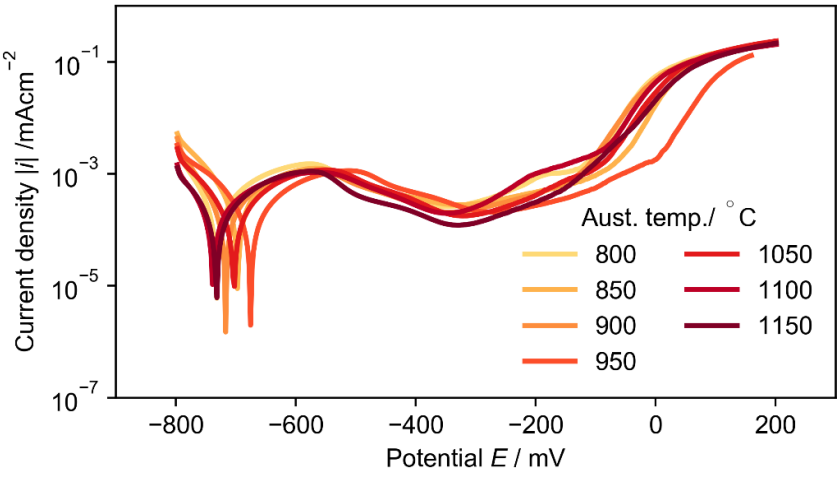

Figure 7-6: LSV measurements of bearing steel after austenitizing at different temperatures in 0.1 M phosphate buffered saline; Scan rate: 1 mVs^{-1}

The active passive region can be observed with a peak between -600 mV and -500 mV. The passive region shows a minimum between -400 mV and -300 mV and is followed by the transpassive region, characterized by a steep slope of the anodic current due to metal dissolution (Figure 7-6).

The passive current i_{pas} is linked to the protectiveness of the passive film and is related to the slowed down dissolution in the passivated state. A low passive current indicates a better protection by the oxide film. The passive current of the samples is clearly affected by the heat treatment procedure. The trends in the passive current density and the martensite content over the austenizing temperature are qualitatively remarkably similar (Figure 7-7a). The highest passive current is measured over the sample with the highest martensite content (heat treatment at 850 °C). The lowest passive current is achieved after a heat treatment at 1150 °C, which resulted in the lowest martensite content. Plotting the passive current versus the martensite content reveals a nearly linear dependency that shows that the passivation deteriorates with increasing martensite content (Figure 7-7b). The pitting potential E_{pit} indicates the potential at which the passive film breaks and accelerated corrosion occurs. A lower pitting potential, in turn, indicates a faster breakdown of the passive film and, thus, a worse passivation. The pitting potential of the heat-treated bearing steel samples shows a very similar course compared to the martensite content (Figure 7-8a). Even though the dependency of the pitting potential is not as clear as for the passive current, a decrease of pitting potential with increasing martensite is recognizable (Figure 7-8b). The lowest pitting potential (earliest film breakdown) can be found for the sample with the highest martensite content (850 °C), whereas, the highest pitting potential is measured at an austenitizing temperature of 950 °C. This is the sample with the lowest martensite content before the last carbide species dissolves.

Similar to mechanical properties (e.g. the hardness), the electrochemical properties are affected by several microstructure properties. Here, the martensite content seems to have the dominant effect. In both cases, in case of the passive current density and the pitting potential, an increasing martensite content leads to a worsening of the corrosion behavior, visible by an increasing passive current density and a decreasing pitting potential.

As discussed in chapter 6, the dissolution of carbides leads to contrary effects for martensitic stainless steel. The passive current and pitting potential decrease due to the higher amount of chromium and lattice distortions, induced by the higher carbon content, respectively. In comparison, the chromium content is much lower for the bearing steel investigated in this chapter. This is also reflected in the electrochemical properties. The effect of the carbide dissolution of the bearing steel on the pitting potential is comparable to the observed effect on martensitic stainless steel. The increased amount of carbon leads to lattice distortions and decreases the pitting potential. This is visible through the drastically lower pitting

potential for the sample austenized at 850 °C (87.9 wt.-% martensite) and the decreased potential after a heat-treatment at 1050 °C (73.3 wt.-% martensite). In contrast, the influence of carbide dissolution on the passive current density is less pronounced. This can be explained with the significantly lower chromium content in the carbides compared to the iron content. Thus, the carbide dissolution does not have the same positive effect on the passive current which could be observed for the martensitic steel.

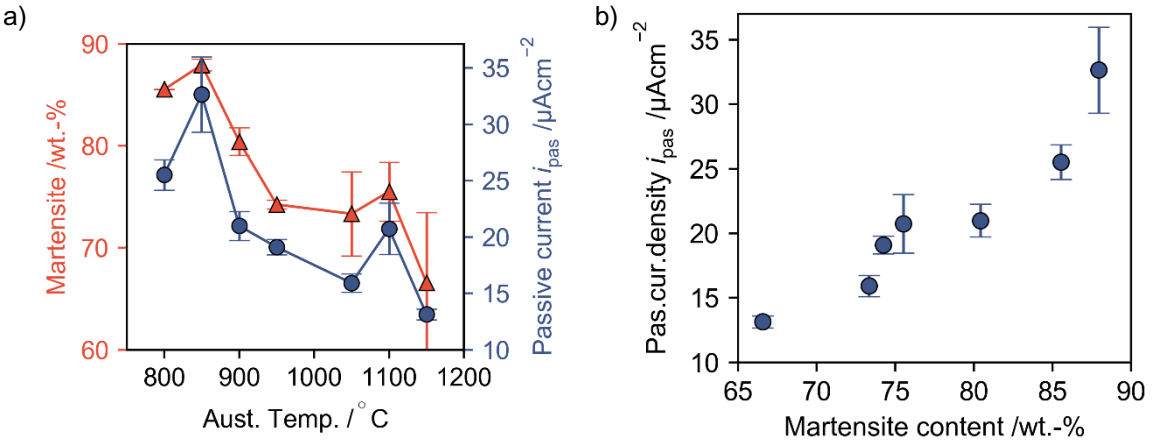

Figure 7-7: Passive current density of differently treated bearing steel samples determined from the LSV measurements presented in Figure 7-6. a) Passive current and martensite content over austenitizing temperature. b) Passive current versus martensite content. Error bars represent the standard error of three independent measurements.

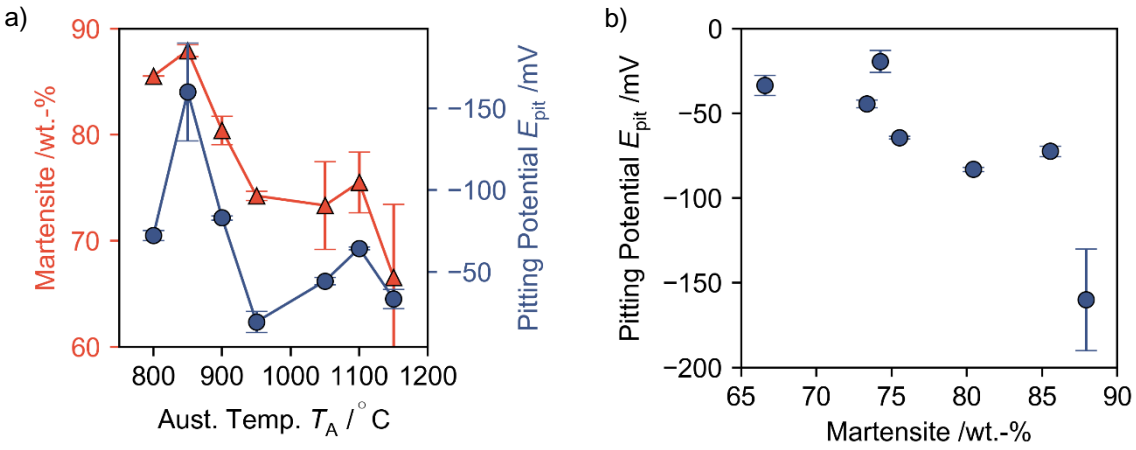

Figure 7-8: Pitting potential of different treated bearing steel samples determined from the LSV measurements presented in Figure 7-6. a) Pitting potential and martensite content over austenitizing temperature. The ordinate is inverted. b) Pitting potential versus martensite content. Error bars represent the standard error of three independent measurements.

7.3 Passive Film Growth Kinetics

To analyze the origin of the observed phenomena during LSV measurements, as discussed in the previous section, impedance measurements are performed. Subsequently, the PDM model presented in chapter 3 and 4 is fitted to the impedance data to obtain the kinetic parameter.

The samples are passivated in 0.5 M H_2SO_4 at 0.8 V, 0.9 V and 1.0 V. The passivation time is set to 14000 seconds because the impedance of the sample changes with time and seems to be constant between 12600 s and 14000 s (Figure 7-9). The variation of passivation potential leads to changes of the impedance response (Figure 7-10a). According to the PDM, higher potentials increase the passive film thickness and, thus, the EIS response of the sample. By changing the passivation potential, it is possible to determine the polarizability of the film/solution interface α (compare Chapter 4), which is found to be $\alpha = 0.85$.

The Nyquist plot of the different heat-treated samples is presented in Figure 7-11. The impedance increases for higher austenitizing temperatures from 800 °C to 950 °C. The overall impedance of the sample heated up to 1050 °C (dissolution of M_3C carbides) shows a clear decline compared to the sample heat-treated at 950 °C. Further increasing the austenitizing temperature leads to a higher overall impedance for T_A: 1100 °C, while the sample austenitized at 1150 °C shows nearly the same impedance as the 1050 °C sample.

The Bode plots of the EIS measurements of the seven bearing steel samples and the fitting according to the PDM (and the EEC presented in Figure 7-13) are presented in Figure 7-12. The EEC consists of an electrolyte resistance R_{el}, a charge transfer resistance R_{ct}, a CPE for the double layer (and the outer layer) CPE_{dl}, a CPE representing the capacitive behavior of the passive layer CPE_{pl}, and an impedance element describing the interfacial reactions predicted by the PDM Z_{PDM}. The necessity for two time constants is clearly visible by the course of the phase, and justifies the use of the presented EEC. The fitting by the PDM is in very good agreement with the measurements.

Starting from the PDM fit, the kinetic parameters for passive film growth are determined (Table 7-3). A comparison of the course of hardness vs. austenitizing temperature and the standard rate constant k_2^0 for film growth shows clear similarities (Figure 7-14a). This leads to the conclusion that both values are influenced similarly by the microstructure. Increasing the martensite content seems to increase the standard rate constant of film growth and accelerate the dissolution process, visible through a relatively linear increase of the standard rate constant with increasing martensite content (Figure 7-14b). The course of the standard rate constant differs especially at higher austenitizing temperatures (lower martensite content) compared to the course of the martensite content and is very similar to the hardness. This region seems to be mainly affected by the grain size and less by the martensite content.

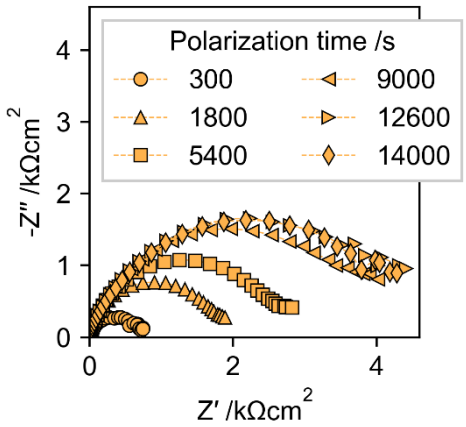

Figure 7-9: Nyquist plot of the sample austenized at 850 °C after polarization at 0.9 V in 0.5 M H_2SO_4 for different times.

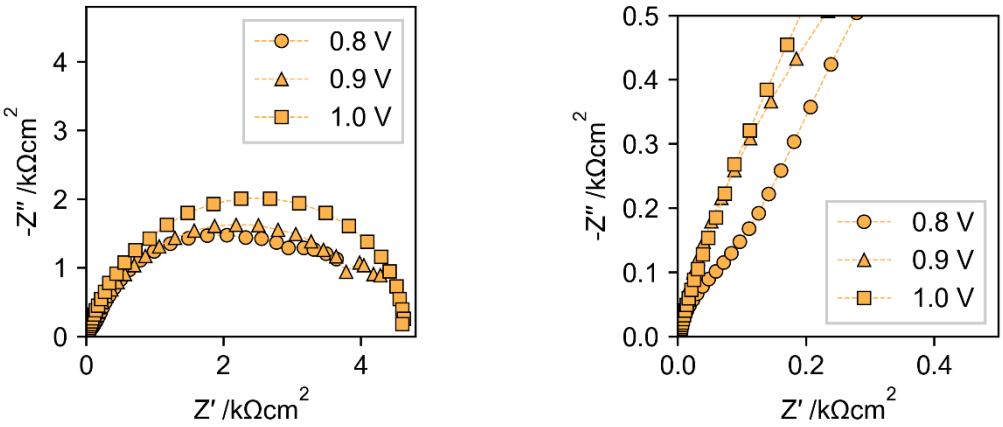

Figure 7-10: Nyquist plot of the sample austenized at 850 °C after polarization in 0.5 M **H_2SO_4** for 14000 s at different polarization potentials.

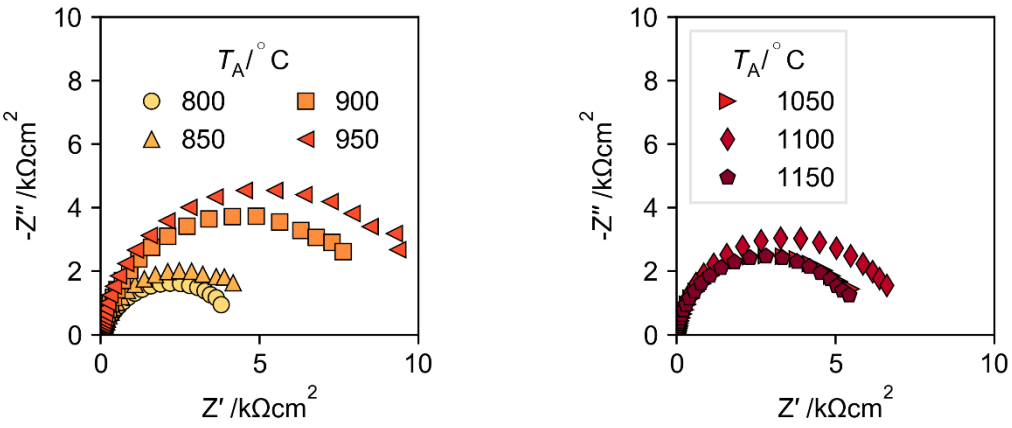

Figure 7-11: Nyquist plot of the bearing steel samples austenitized at different temperatures. Polarized at 0.9 V in 0.5 M H_2SO_4 for 14000 s.

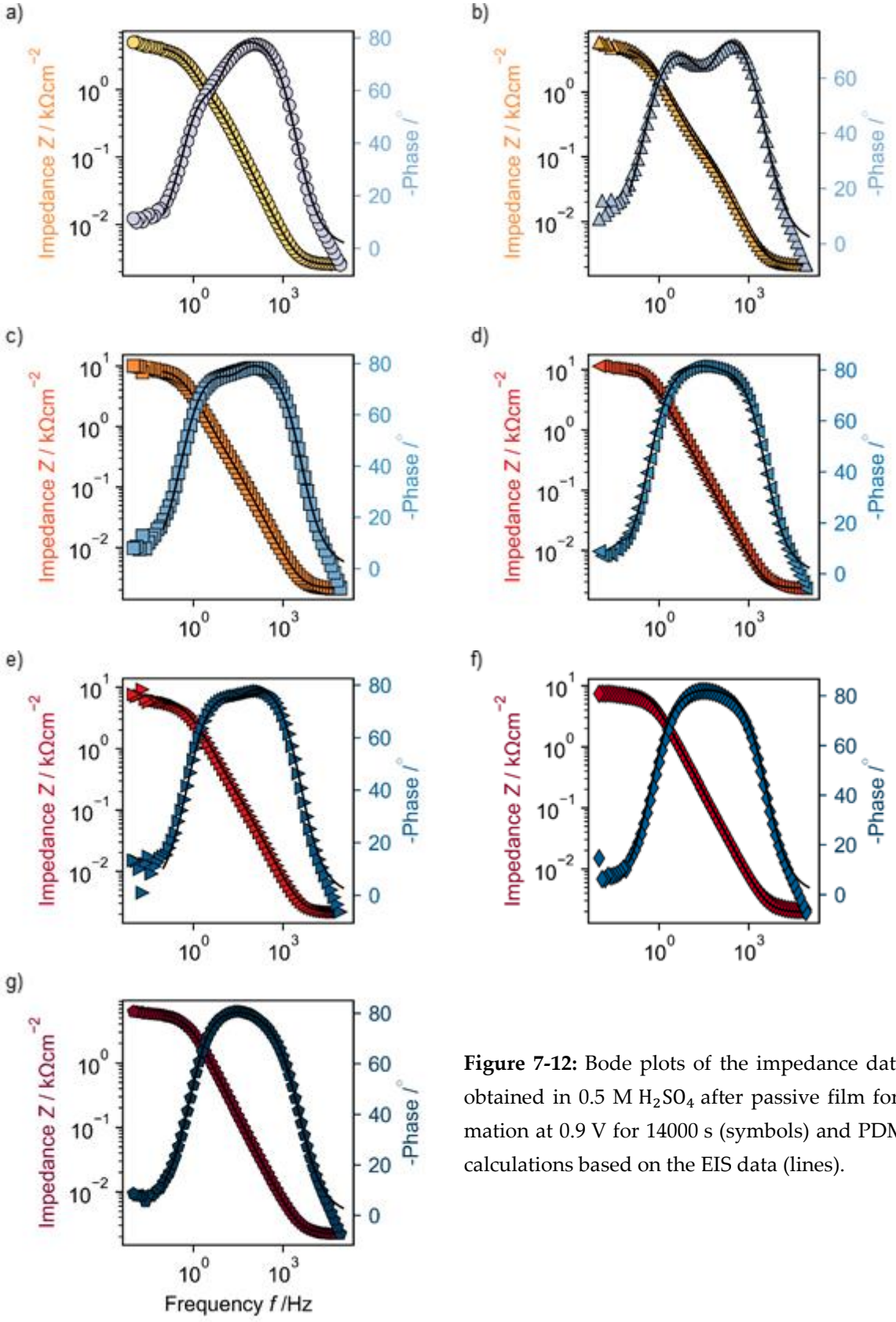

Figure 7-12: Bode plots of the impedance data obtained in 0.5 M H_2SO_4 after passive film formation at 0.9 V for 14000 s (symbols) and PDM calculations based on the EIS data (lines).

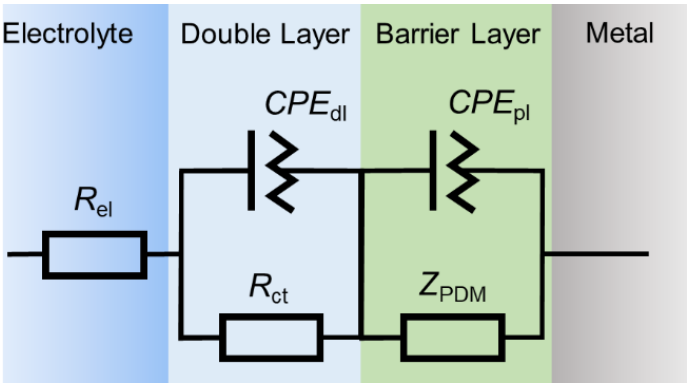

Figure 7-13: Equivalent electrical circuit to fit the impedance data. $\boldsymbol{R_{el}}$: electrolyte resistance, $\boldsymbol{CPE_{dl}}$: CPE representing the double layer, $\boldsymbol{CPE_{pl}}$: CPE representing the passive layer, $\boldsymbol{R_{ct}}$: charge transfer resistance, $\boldsymbol{Z_{PDM}}$: faradaic impedance due to the reactions on the metal–film and film-solution interface described by the point defect model.

The effect of carbide dissolution seems to be less noticeable in the standard rate constant, since k_2^0 for 800 °C and 850 °C (dissolution of M_7C_3) as well as for 950 °C and 1050 °C (dissolution of M_3C) shows relatively similar values.

The rate constant k_7, which dictates the film dissolution and, thus, the steady state corrosion rate in the passivated state, decreases with decreasing austenitizing temperature (Figure 7-15). The dissolution of the passive film is not directly linked to the properties of the bulk material but to the properties of the passive film itself. Of course, the passive film properties are determined by the bulk material and its properties but they can behave different.
It is assumed that the accelerated reaction at the metal/film interface with increasing martensite content (Figure 7-14b) leads to a higher number of defects in the passive film itself. Coarse grained material can also lead to a less defective passive film [121]. Considering the increasing grain size for higher austenitizing temperatures and the decreasing martensite content, one would expect a less defective film with increasing austenitizing temperature. Taking this in account, the decreasing rate content of film dissolution seems reasonable. An analysis of the defect density with respect to the martensite content also reveals an increase of defects inside the passive film with increasing martensite content (Figure 7-16). The calculated defect concentration for every sample over the passive film can be found in A6.

Table 7-3: Fitted kinetic parameters for all martensitic stainless steel samples.

T_A /°C	k_2^0 /mmolcm^{-2}s^{-1}	α	k_7 /mmolcm^{-2}s^{-1}	L /nm
800	4.28×10^{-11}	0.054	1.73×10^{-10}	1.51
850	4.95×10^{-11}	0.036	1.71×10^{-10}	1.55
900	1.82×10^{-11}	0.042	1.09×10^{-10}	1.35
950	1.06×10^{-11}	0.045	1.04×10^{-10}	1.08
1050	1.46×10^{-11}	0.043	7.47×10^{-11}	1.13
1100	7.59×10^{-13}	0.092	5.59×10^{-11}	1.30
1150	4.80×10^{-13}	0.105	5.58×10^{-11}	1.30

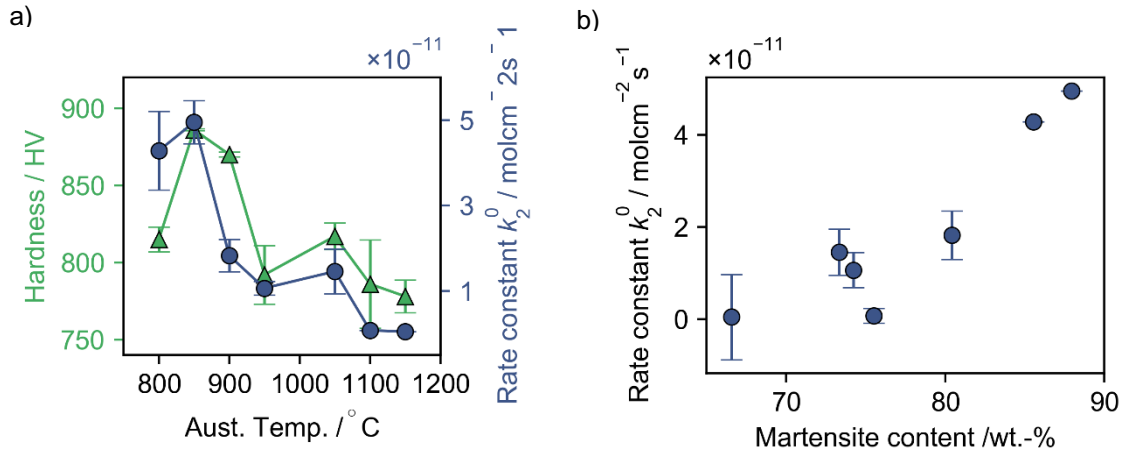

Figure 7-14: Standard rate constant of film growth $\boldsymbol{k_2^0}$ for different treated bearing steel samples determined by passive film growth kinetic fitting by the PDM. a) $\boldsymbol{k_2^0}$ over austenitizing temperature compared to hardness over austenitizing temperature. b) Standard rate constant $\boldsymbol{k_2^0}$ over martensite content.

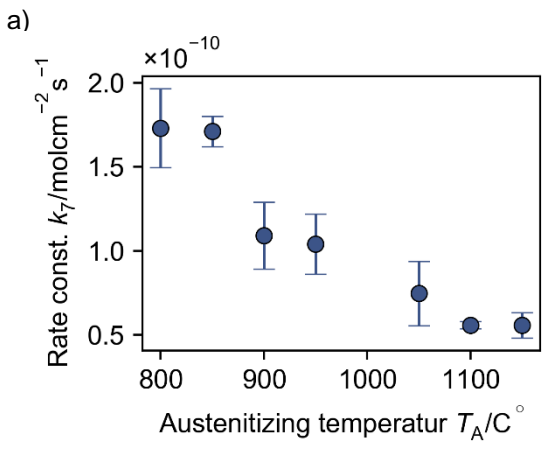

Figure 7-15: Dependency of the film dissolution rate $\boldsymbol{k_7}$ over austenitizing temperature.

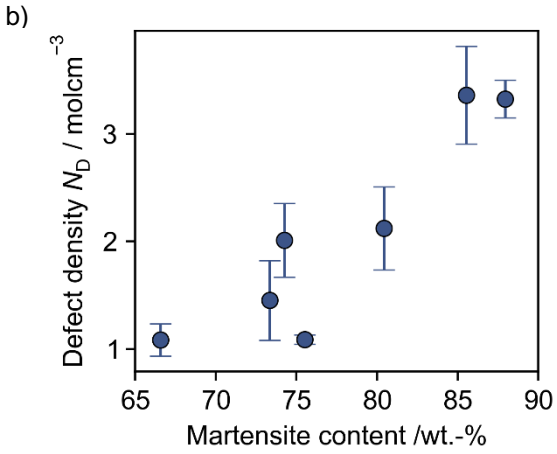

Figure 7-16: Defect density of the passive film depending on the marteniste content.

7.4 CONCLUSION

A clear dependency of electrochemical properties and passive film growth kinetics on the microstructure properties could also be found for the bearing steel. The microstructure changes due to the heat treatment are more complex for the bearing steel compared to the martensitic steel. For this reason, the electrochemical behavior of the samples regarding the austenitizing temperature is also more complex. Nevertheless, a comparison of the corrosion properties and kinetic parameters with microstructure and mechanical properties shows

clear similarities. The martensite content is the dominant microstructure parameter and shows the strongest effects on the electrochemical behavior. The passive current density exhibits a nearly linear and positive dependency on the martensite content. The pitting potential decreases with increasing martensite content but seems to be affected by the grain size and the carbide content as well. Decreasing passive current densities are due to slowed down passive film dissolution determined by the rate constant of film dissolution k_7. The decline of the pitting potential can be explained by the increasing defect densities inside the film. On the other hand, the film thickness itself increases with the martensite content (due to the accelerated standard rate constant k_2^0) which could explain why the course of pitting potential is not similar to the martensite content or the defect densities.

The main reason for the differing electrochemical behavior between the bearing steel and the martensitic stainless steel is the chromium distribution and the dissolution of carbides. Due to the significantly lower chromium content in the bearing steel this seems to be not a decisive effect. It appears that the martensite content is the main cause for the differing electrochemical behavior. Yet, the martensite content changes are overlaid by additional microstructure changes, i.e. grain size and carbide dissolution, and it is not possible to isolate the effects of one microstructure parameter on the kinetics. In the next chapter, a mechanical material treatment is used to isolate martensite/austenite phase ratio changes and to investigate the effects of the phase ratio on the passive film growth kinetics.

8

ISOLATION OF MARTENSITE CONTENT CHANGES[4]

The influence of austenitizing temperature on martensitic stainless steel corrosion properties and its passive film growth kinetics has been successful described by comprehensive electrochemical measurements and modeling based on the PDM. When transferring the results to another alloy, the common bearing steel AISI 52100, it could be shown that additional microstructure changes take place which influence the electrochemical behavior in different ways. The results clearly indicate that the martensite content has the strongest effect on the passive film growth kinetics. To verify this assumption and to isolate the influence of the martensite/austenite phase ratio on the passive film growth kinetics, the martensite content of an austenitic stainless steel has been systematically changed by rotary swaging [16,122].

By changing the feed velocity of rotary swaging it is possible to change the martensite content of austenitic steel while the grain size (in radial direction) remains constant [16,123].

[4] Parts of this chapter have been published in *Matec Web of Conferences* 190 (2018) [16] and *Int.J. Electrochem. Sci.* 15 (2020) [17]

Three samples with different martensite content are produced by changing the feed velocity of the rotary swaging process and the passive film growth kinetics are studied using the PDM.

The investigation starts with CV measurements of the three different samples to deepen the understanding of passivation in the given electrolyte. These measurements also show differences regarding the passivation processes due to the differing martensite content.

8.1 METHOD

The used methods for material treatment, microstructure investigations and electrochemical measurements are described in the following section.

8.1.1 MATERIAL

The investigated material is the industrial stainless chromium nickel steel AISI 304. The element distribution is given in Table 8-1. The high chromium and nickel content ensure a good corrosion protection.

Table 8-1: Element distribution of the stainless steel samples according to AISI guidelines.

	C	Si	Mn	P	S	Cr	Ni	N
min.	-	-	-	-	-	17.5	8	-
max.	0.07	1.0	2.0	0.045	0.03	19.5	10.5	0.1

8.1.2 ROTARY SWAGING

Rotary swaging is an incremental cold forming process to produce axisymmetric workpieces from rods and tubes. In the macro-range, it has an important field of application in the automotive industry, for example, to produce axes, steering spindles and gear shafts [124]. It is also suitable for micro manufacturing to produce micro parts. During infeed rotary swaging the workpiece is axially fed into the swaging unit and the diameter is reduced incrementally by a radially oscillating motion of three tools [122]. The swaging unit is rotating and the base jaws with the cam pass the cylinder roller and induces the simultaneously radially stroke of the tools.

Rotary swaging experiments were done by bime (Bremen Institute for Mechanical Engineering) and conducted with annealed workpieces of material AISI 304 (X5CrNi18-10). The

workpieces were fed with a direct linear motion drive with different feed velocities of v_f = 1 mm/s, 5 mm/s and 10 mm/s into the swaging head. The stroke height of the tools (h_T = 0.1 mm) and the stroke frequency (f_{st} = 102 Hz) were kept constant. A lubricant (Shell Macron 01 F-2) was applied to all forming operations. The initial diameter of the workpieces was d_0 = 1 mm. The tool set of the material 1.2379 (X155CrVMo12) were used, with a nominal diameter of d_{nom} = 0.75 mm. The tool set had a tool angle α = 10° and a calibration length l_{cal} = 20 mm. Workpieces were deformed in one stage with the tool set to a final diameter of d = 0.8 mm.

8.1.3 XRD

The XRD analysis was done analogously to the procedure described in Section 6.1.3.

8.1.4 Electrochemistry

All electrochemical measurements were carried out at room temperature in a standard three electrode cell using a Metrohm Autolab potentiostat with the PGSTAT204 and the FRA32 modules. As counter electrode served a platin electrode, and as reference electrode an Ag/AgCl electrode was used, while the investigated material acted as the working electrode. The samples were embedded with two component adhesive in a PVC holder. All potentials in this chapter are referred to the Ag/AgCl electrode.

The CV measurements were done in 0.1 M phosphate buffer solution (pH = 7.5). The cyclic voltammetry measurements were performed with a scan velocity of 100 mV/s. Each CV started from -1000 mV and ended at 1100 mV. EIS measurements to parametrize the PDM were carried out in a frequency range of $10^{-2} - 10^{5}$Hz at open circuit potential after 3600 s in solution for passive film growth.

Before each measurement, the working electrodes were wet grinded with SiC grinding paper (60 grid), degreased in ethanol, and cleaned in an ultrasonic bath containing deionized water. A determination of the influence of sample pretreatment is presented in Section A3.

8.2 Results

The results of the metallographic analysis and of the electrochemical experiments are presented in the following chapter. Subsequently the results of the passive film growth kinetics fitting are given and discussed regarding the findings of the material scientific and electrochemical measurements.

8.2.1 XRD - MEASUREMENTS

The martensitic phase formation during plastic deformation was studied by Leibniz-IWT using XRD. The XRD patterns and the Rietveld refinement of the annealed and differently deformed samples show sharp and well-resolved reflections (Figure 8-1), which illustrate well the evolution of martensitic α-peaks and the corresponding development of austenite γ-peaks depending on the process parameters. The increase of the α-peak correlates with the generation of deformation-induced martensite during the process. Moreover, a broadening of the diffraction peaks can be observed.

The results of the dislocation density calculations are given in Table 8-2. Surprisingly, the dislocation density decreases slightly with martensite content. The residuals of the weighted profiles R_{wp} of the refined XRD data lay between 3.4 and 3.6 and thus show very good agreement.

8.2.2 CYCLIC VOLTAMMETRY

The passive layer on stainless steel is mainly composed of different iron and chrome oxides. Using CV, the formation of different oxide species can be distinguished as the formation is associated with different current density peaks. Figure 8-2a shows the first CV cycle of stainless steel samples with different martensite content.

The observable total current density is composed of a capacitive current i_{cap} and a faradaic current i_{F}:

$$i_{\mathrm{tot}} = i_{\mathrm{cap}} + i_{\mathrm{F}} \qquad 8\text{-}1$$

The capacitive current density i_{cap} results from the double layer charging at the electrode surface:

$$i_{\mathrm{cap}} = C_{\mathrm{dl}} \frac{\mathrm{d}E}{\mathrm{d}t} \qquad 8\text{-}2$$

with the change of potential over time $\mathrm{d}E/\mathrm{d}t$ (synonymous with the scan rate of the CV) and the double layer capacity C_{dl}.

Table 8-2. Weighted R-factors (R_{wp}) and martensite contents extracted from the XRD analysis.

Sample	R_{wp}	Martensite content / wt.-%	Dislocation density / cm²
1	3.57	21	1.81×10^{10}
2	3.42	35	1.61×10^{10}
3	3.67	47	1.59×10^{10}

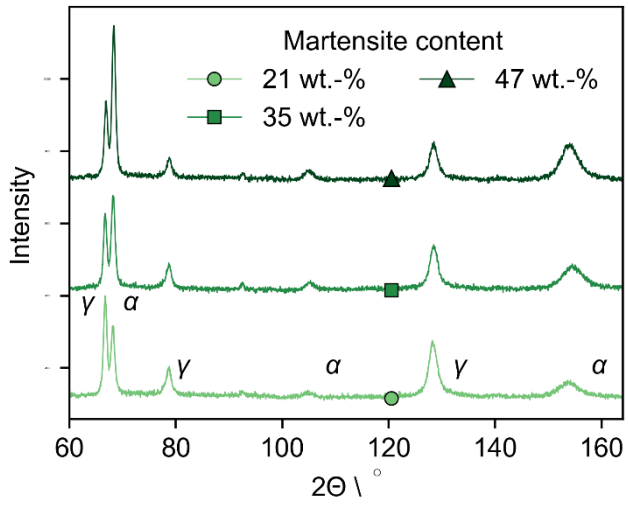

Figure 8-1: XRD pattern of the three samples with different martensite content.

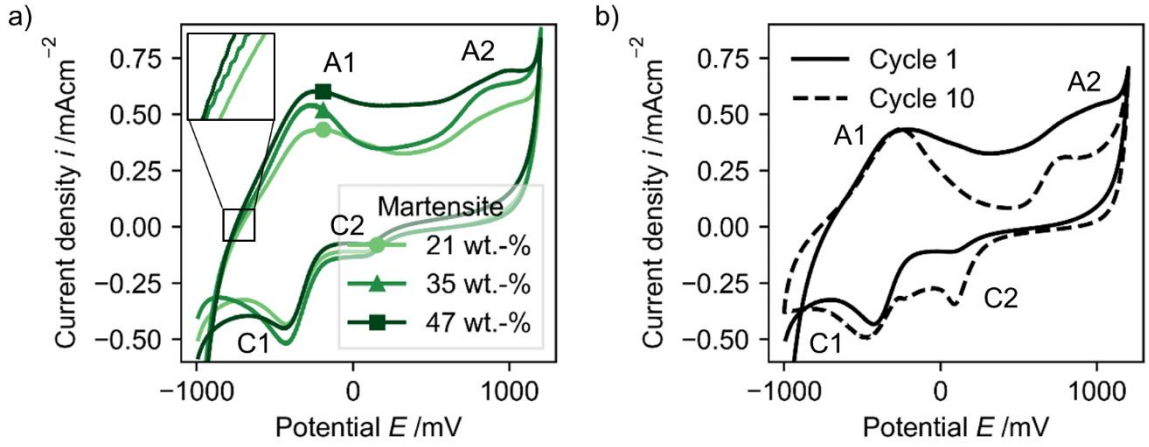

Figure 8-2: Cyclic voltammetry measurements in phosphate buffer at scan velocity 100 mV/s. a) First cycle of species with different martensite content, the inset shows the zero crossing. b) Cycles 1 and 10 of the 21 wt.-% martensite sample.

The scan rate is a process parameter and equal for every measurement (100 mVs^{-1}). The double layer capacity depends mainly on the electrolyte concentration (0.1 M) and the surface preparation, which are the same for all samples. Considering this, the capacitive current should be similar for all three samples and observable differences of the current density result from the faradaic processes. A high scan rate shifts the corrosion potential to more cathodic potentials [32,125] and, can change the current values such that the oxidation and reduction peaks become more pronounced [126,127]. It should be noted that, while a high scan rate is helpful for the investigation of oxidation/reduction processes at the steel surfaces, a lower scan rate should be used for the determination of the corrosion current and stochastic phenomena like pitting corrosion [32,125].

The faradaic current density i_f is composed of oxidation and reduction processes at the

electrode surface as well as oxidation and reduction of the metal species. At high anodic and cathodic potentials (close to the return potentials) the faradaic currents are dominated by hydrogen evolution at cathodic potentials and oxygen evolution at high anodic potentials. Additionally, the reduction of oxygen and the resulting formation of hydronium ions can occur in basic electrolyte. These processes superimpose the oxidation and reduction processes of the investigated metal species. However, since these processes should be similar for every sample they can be neglected for the interpretation of the differing current densities.

While the current increases and the overall current changes from cathodic to anodic current, the oxidation of iron occurs first in all three samples (Figure 8-2a). The first visible peak A1 was attributed to the formation of Fe(III)-oxide from Fe(II)-oxides and –hydroxides on a preexisting Cr(III)-oxide layer [128]. Due to the formation of Fe(III) oxide from Fe(II)-oxide/hydroxide, mixed species like magnetite can occur [129]. The shoulder/peak A2 indicates the oxidation of Cr(III) to soluble Cr(VI) as chromate [29, 31, 32] followed by transpassive dissolution [128] and formation of oxygen.

Naturally, the back scan leads to the reduction of the oxide species on the metal surface. First, chromium oxide is reduced, which is visible by the associated reduction peak C2. Since Cr(VI) is soluble in aqueous solutions, the peak C2 is very small in the first cycle. With increasing number of cycles C2 becomes more pronounced because Cr(VI) oxide remains arrested in the passive layer [55]. The reduction of Cr(VI) is followed by the reduction of the iron oxides and change of oxide states (reduction peak C1) [132]. The course of the CVs is in very good agreement with similar CVs in neutral and basic electrolytes reported in the literature [116,126,127,130,133,134].

Ongoing redox cycles alter some of the reactions in a different way. This becomes obvious by comparing the first and the tenth cycle (Figure 8-2b). While the maximum anodic peak current density remains the same for peak A1, the peak area gets smaller and the passive area becomes clearer. During the first cycle, the Cr(VI) species dissolve to the solution. As a result, the peak is less pronounced and the current density increases further with increasing potential. For higher cycles numbers, the chromate species are fixed inside the passive layer and the peak A2 becomes more distinct. The lower current density between peak A1 and A2 indicates a better passivation and less dissolution with increasing number of cycles.

While the qualitative trend of the CVs is similar for all three species, there are several differences due to the change of martensite content. The current density in the passive area (between peak A1 and A2) as well as the maximum peak current densities increase for higher martensite contents. This indicates a worse passivation with increasing martensite content since the passive current is an indicator for the protective effect of the passive layer.

Additional to the differences of the current densities, one can observe differences of the zero crossing potentials (inset Figure 8-2b). This potential is related to the corrosion potential

shifted by the capacitive current [32]. The zero-crossing potential increases with decreasing martensite content from -752.8 mV vs. Ag/AgCl for the sample with martensite content of 47 wt.-% over -738.7 mV vs. Ag/AgCl to -717.0 mV vs. Ag/AgCl for the sample with a martensite content of 21 wt.-%. This underpins that the martensite phase is less noble compared to the austenite phase, considering the corrosion potential being a mixed potential of both phases.

The ratio between anodic and cathodic peak area can also be used to investigate the passivation processes of the electrodes. A high charge ratio Q_A/Q_C indicates an incomplete reduction of the oxidized species to their initial state during the back scan. Either the oxidation products do not remain on the surface or they remain on the surface but are not completely reduced to their initial state. If the anodic and cathodic charge densities adjust and the charge ratio Q_A/Q_C tends towards 1, all oxidized species remain on the surface and will be reduced during the back scan. The chromium oxides get "arrested" on the electrode surface with increasing number of cycles—visible by the growing reduction peak C2—and form a more protective and stable passive film [55].

Figure 8-3a shows the ratio of anodic and cathodic charge of a full cycle in dependence of the number of cycles. The amount of oxidized species increases with martensite content (increasing anodic charge) but a smaller proportion of the oxidized species remains on the electrode surface (higher charge ratio, with increasing martensite content) and does not contribute to a better passivation (increasing passive current density). With ongoing cycles, the charge ratio of all three samples decreases. Figure 8-3b compares the anodic and cathodic total charges of the first cycle as a function of the martensite content. The amount of both, anodic charge as well as the amount of cathodic charge, during the CV increases with increasing martensite content.

The analysis of the cyclic voltammograms indicates the importance of martensite content for the formation of the passive layer. With increasing martensite content (higher charge ratio), the solubility of the oxidation products and, thus the current density in the passive region increase. This indication of a worsening passivation with an increasing martensite content goes along with a higher susceptibility to corrosion of the less-noble phases.

8.2.3 Impedance Spectroscopy

Deeper insights into the nature of the passive film formed on stainless steel with differing phase composition were provided by impedance measurements. Nyquist plots of impedance spectra performed in 0.1 M phosphate buffer reveal an overall impedance decrease with increasing martensite content (Figure 8-4). By fitting the equivalent electric circuit (EEC) shown in Figure 8-5 to the impedance data, different electrical components were assigned to elec-

trochemical counterparts on the electrode surface. The parameters proposed in the EEC represents the electrolyte resistance R_{el}, a polarization resistance R_{pol}, and the capacity of the passive layer and the electrochemical double layer *CPE*. To represent the capacity at the electrode surface, a constant phase element (CPE) is used. The impedance of a CPE is calculated using two variable CPE descriptors Q and N:

$$Z = \frac{1}{(j\omega)^N Q} \qquad 8\text{-}3$$

For N=1, the CPE behaves like a perfect plate capacitor, for N=0, the CPE behavior represents a perfect resistor and for N=-1 an inductance. Any deviation from these values during EEC parameter identification when fitting the model to the EIS data indicates non-ideal behavior of the layers. This can be expected for oxide layers that usually include in homogeneities, and their behavior should therefore deviate from the one of perfect plate capacitors.

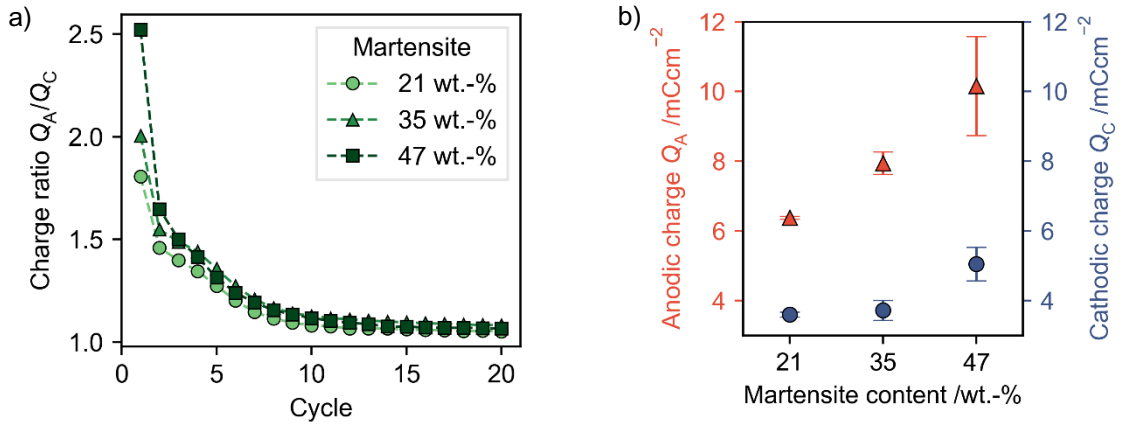

Figure 8-3: Faradaic charge for 3 different martensite contents: a) Total charge ratio for all 20 cycles and b) anodic (triangles) and cathodic (circles) charges after cycle 1

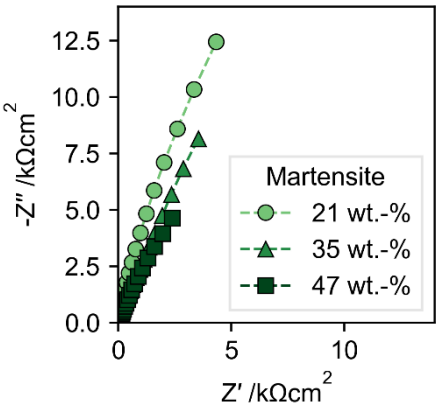

Figure 8-4: Bode plot of impedance data obtained in 0.1 M phosphate buffer after 1h passive layer formation at OCP; 100 kHz - 0.1 Hz.

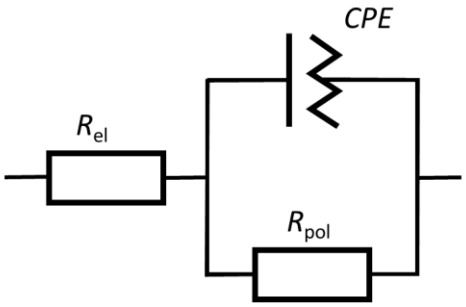

Figure 8-5: Equivalent electrical circuit (EEC).

The EEC parameters shown in Table 8-3 are obtained by fitting the impedance data to the EEC model. The goodness of fit was checked by Pearson´s chi squared-test showing chi-square values between $X^2 = 0.013$ and $X^2 = 0.255$, where a low value indicates a good fit.

The electrolyte resistance values for all samples are of the same order of magnitude and vary between 2.7 Ω and 3.1 Ω. The polarization resistance R_{pol} decreases with increasing martensite content indicating less resistance against the oxidation of the metal species and thus against corrosion. A similar result was found by Wang et al. who were able to observe a decreasing charge transfer resistance with increasing martensite content [105]. The CPE parameters Q and N also differ with martensite content. While N slightly decreases, the parameter Q increases with martensite content.

These EIS findings are in agreement with the findings of cyclic voltammetry measurements. An increasing martensite content leads to a less protective passive layer and a lower resistance against corrosion represented by the polarization resistance R_{pol}. Additionally, the change of the CPE parameter *N* indicates a structural change in the passive layer. A decreasing *N* value shows higher deviation from the plate capacity.

8.2.4 Mott-Schottky Analysis

The point-defect densities of the passive films were analyzed with Mott-Schottky analyses. By performing impedance measurements on different DC potentials, it is possible to calculate the space charge capacity C_{sc} of the oxide film depending on the potential. A plot of $\frac{1}{C_{\mathrm{sc}}^2}$ over the DC potential (Mott-Schottky plot) reveals the dopant density and the flatband potential of a semiconductor. As described in Chapter 3 for a linear dependency of $\frac{1}{C_{\mathrm{sc}}}$ on the applied potential E, the defect density N_{D} and the flat band potential E_{fb} can be calculated by the Mott-Schottky equation,

$$\frac{1}{C_{\mathrm{sc}}^2} = \frac{2}{\varepsilon\varepsilon_0 e N_{\mathrm{D}}}\left(E - E_{\mathrm{fb}} - \frac{kT}{e}\right). \qquad 3\text{-}3$$

By the slope of the Mott-Schottky plots in the linear region of the depletion area it is possible to determine whether the passive layer is n-doped (positive slope) or p-doped (negative slope). According to the Point Defect Model (PDM), developed in the 1980s by Macdonald et al., passive films on stainless steel are highly defect rich semiconductors [61]. Passive film growth depends on interfacial reactions and the transport of point defects through the film. The type of the point defects inside the passive layer determines the semi-conductive nature of the oxide film. Metal interstitials and oxygen vacancies lead to n-type films while metal vacancies lead to p-type films [54].

Table 8-3: EEC parameters obtained by fitting the impedance data presented in Figure 8-4 to the EEC shown in Figure 8-5.

Martensite content	R_{el} / (kΩcm²)	Q / ($\Omega^{-1}cm^{-2}s^{-n}$)	N	R_{pol} / (kΩcm²)
21 wt.-%	2.92×10^{-3}	1.00×10^{-4}	0.89	72.3
35 wt.-%	3.09×10^{-3}	1.32×10^{-4}	0.87	34.1
47 wt.-%	2.74×10^{-3}	2.23×10^{-4}	0.80	26.5

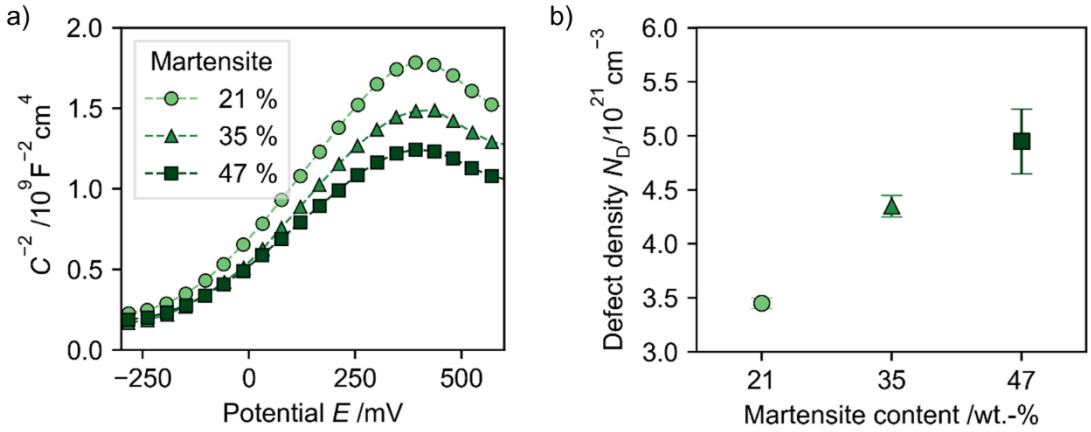

Figure 8-6: a) Mott-Schottky plots of the capacity of the space charge region within the passive layers obtained at 100 Hz b) Defect density of the passive layer in dependence of the martensite content.

The Mott-Schottky plots of the capacity of the space charge region within the passive layers were determined for all three samples in phosphate buffer after 1 h passive layer formation at OCP (Figure 8-6a). The space charge capacity was calculated at 100 Hz. The positive slope suggests the passive films, formed on the surfaces of all three samples, are n-type semiconductors. According to Equation **Fehler! Verweisquelle konnte nicht gefunden werden.**, the dopant concentration N_D (in case of n-type passive films oxygen vacancies and metal interstitials) can be calculated by the slope in the $1/C_{sc}^2$ versus E plot. The defect density inside the passive film increases with martensite content (Figure 8-6b). The lattice distortions in the bulk material (the stainless steel itself) seem to accelerate the production of point defects (metal interstitials and oxygen vacancies). Distortions of the bulk material are seemingly passed on to the passive film as lattice defects. According to the PDM, the breakdown mechanism of passive films starts with the adsorption of aggressive anions (e.g. Cl^-) at (positive charged) oxygen vacancies [38,54]:

$$V_{\ddot{O}} + X^- \cdot nH_2O \leftrightarrow X_{\dot{O}} + nH_2O. \qquad 8\text{-}4$$

Here, $V_{\ddot{O}}$ indicates a two times positive charged oxygen vacancy (Kröger-Vink notation) and X^- a halide ion. A high defect density would favor the adsorption of negative charged ions at the passive film surface (due to more positive charge defects) and the injection of this defects into the passive film, leading to the film breakdown. Indeed, Metikoš-Huković et al. could show that the change of n-type to p-type passive films can enhance the pitting corrosion resistance [135] due to less attractive adsorption sites (anion vacancies) for halide ions. The higher the defect concentration, the more attractive the sites to attack and the faster the breakdown of passivity due to pitting corrosion. Thus, the often observed decrease of pitting corrosion due to a higher martensite content [104–106] can be explained by the breakdown mechanism offered by the PDM and the observations of the shown Mott-Schottky analysis.

The results and interpretations of the Mott-Schottky analysis fit the EIS and CV measurements very well and underline the negative effect of a high martensite to austenite ratio for the formation of a protective passive film.

8.3 Influence on Passive Film Growth Kinetics

An extraction of kinetic parameter calculated from the electrochemical impedance spectroscopy data reveals a strong dependency of the passive film growth kinetics on the martensite content. It is important to note that for the extraction a simplified circuit (EEC1 compare chapter 4 and Figure 8-5) was used. The impedance data does not justify the usage of a more complex circuit and additional components would lead to overfitting and free customizable (but among themselves dependent) EEC components. The standard rate constant for film formation k_2^0 as well as the rate content of film dissolution k_7 increase along the martensite content (Figure 8-7), indicating a higher metal to oxide reaction (Reaction 2) and a higher dissolution of the passive film (Reaction 7). Both reactions lead to an increased metal consumption during the passivated state, which, eventually, results in a higher material loss depending on the martensite content. The charge transfer coefficient α_2 of the film formation reaction decreases with increasing martensite content (Figure 8-8).

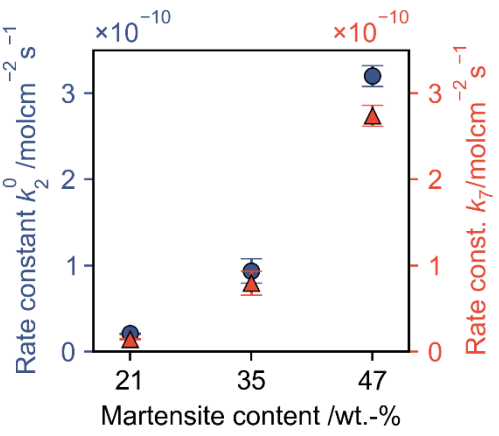

Figure 8-7: Standard rate constant of film formation k_2^0 (●) and rate constant of film dissolution k_7 (▲) depending on the martensite content.

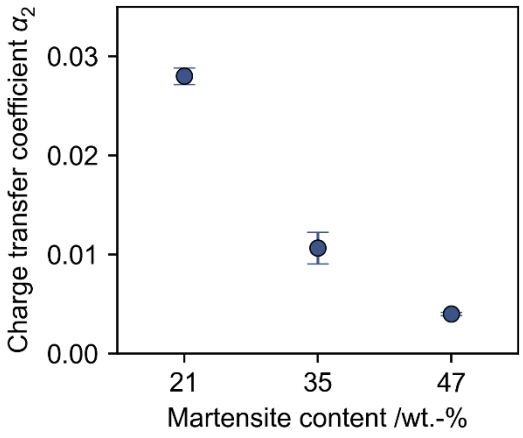

Figure 8-8: Charge transfer coefficient α depending on the martensite content.

8.4 Conclusion

The isolated change of martensite content reveals a strong dependency of the electrochemical behavior on the microstructure parameter of the investigated samples. CV measurements show increased oxidation during anodic scans, while the reduction scans do not show higher cathodic currents. The growing ratio of anodic to cathodic charge with increasing martensite content can be explained with an enhanced dissolution of metal due to a less pronounced protective passive film.

Subsequent impedance measurements could prove the assumption of a less protective film. The polarization resistance decreases with increasing martensite content indicating a higher electrochemical activity due to higher metal dissolution. The interpretation of the impedance data using the point defect model shows higher standard rate constants of film formation and of film dissolution with increasing martensite/austenite phase ratio. The increasing standard rate constant of film formation k_2^0, seems to be affected by the lattice distortions due to the phase transformation. This confirms the observations made in the last chapter about the influence of martensite on the passive film growth kinetics.

The charge transfer coefficient α_2 of the film formation reaction decreases for higher martensite content. A decrease of the charge transfer alone (considering the remaining parameter unchanged) does lead to a slower reach of steady state with a thicker passive film (compare the next chapter). As already observed and discussed in the previous chapters, a thicker film alone appears not to improve the protective effect.

Mott-Schottky analysis of the passive films were used to determine the defect densities in

the passive films of the different samples. The observed dependency of the defect density on the martensite content could be the explanation for the increasing film dissolution. A more defective film is more susceptible for film breakdown reactions and can be a direct result of the higher film formation rate. During the film formation reaction, oxygen vacancies are created. If their consumption does not accelerate to the same extent as their formation, the defect density increases.

Isolated microstructure changes increase the understanding of material treatment effects on the corrosion behavior significantly but are difficult to achieve. In contrast, the effect of a single kinetic parameter can be modeled using the PDM and, consequently contribute to deepen the insight into film growth mechanisms. An overview about how the discussed kinetic parameters affect the film growth mechanism in an isolated manner is given in the next chapter.

9

SENSITIVITY ANALYSIS

In order to indicate the influence of single kinetic parameters on the impedance data and to rank the influence of the parameter sensitivity, an analysis of impedance data with various kinetic parameter changes is performed. Afterwards, the influences of different parameters on the film thickness of passive films and on the film growth and reaction constants are investigated by kinetic modeling with artificial constants.

The PDM does not only offer the possibility to investigate kinetic constants and to compare passive film growth, but based on the model, it is possible to predict the long-term corrosion behavior. Some considerations regarding the usage of the model and about the meaning of single kinetic parameters regarding the corrosion behavior are presented in the last part of this chapter.

9.1 SENSITIVITY OF IMPEDANCE MEASUREMENTS

The effects of changing model parameters on the impedance data are shown in Figure 9-1.

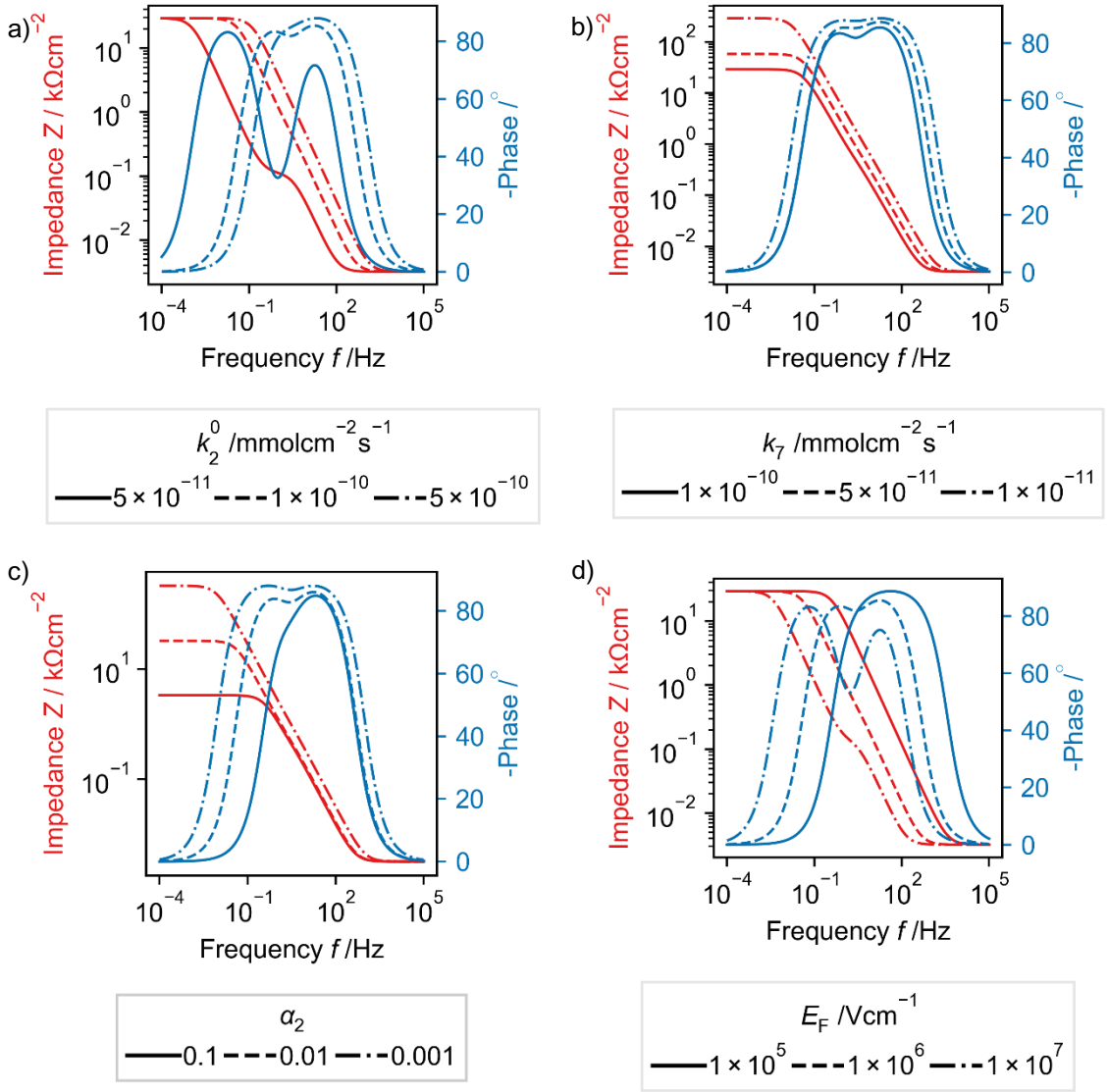

Figure 9-1: Sensitivity analysis of the electrochemical impedance regarding the changes of single kinetic parameters. Variation of kinetic parameter a) $\boldsymbol{k_2^0}$, b) $\boldsymbol{k_7}$, c) $\boldsymbol{\alpha_2}$, d) $\boldsymbol{E_F}$. All other parameters are kept constant (compare Table 9-1).

Table 9-1: Parameter of the impedance elements used for as base case the sensitivity analysis

C_{dl} /µC	R_{ct} /Ω	k_2^0 /mmolcm^{-2}s^{-1}	k_7 /mmolcm^{-2}s^{-1}	α_2	E_F /Vcm^{-1}
500	100	10^{-10}	9×10^{-11}	0.001	10^6

One parameter is changed in every subfigure; all other parameters are kept constant as presented in Table 9-1. The considered system consists of a double layer capacity and a parallel charge transfer resistance, in row with a passive film capacity and the faradic impedance calculated based on the PDM in parallel (EEC2 presented in Chapter 4, which was used in Chapter 6 and Chapter 7 to model the impedance data). The visible effects on the impedance result from changes of the passive film thickness and of the faradaic impedance. A change of each single parameter affects the course of impedance Z and the phase over frequency because of the parameter effects on the passive film thickness. k_7 and α_2 also affect the maximum impedance because both values affect the steady state faradaic impedance. How the film thickness and the rate constant changes due to parameter variations is presented below.

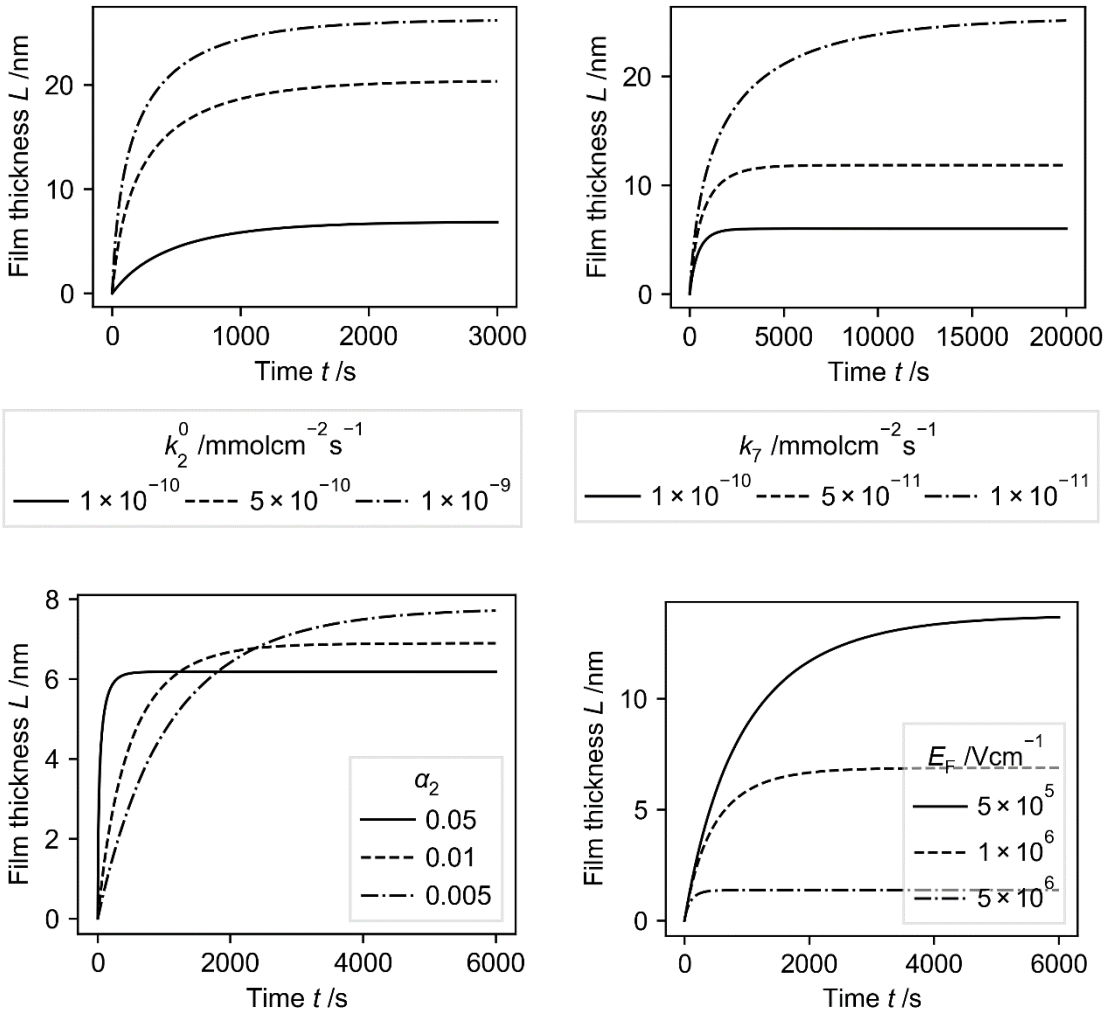

Figure 9-2: Change of passive film thickness due to variation of the kinetic parameters. The additional parameters are kept constant on the values presented in Table 9-1.

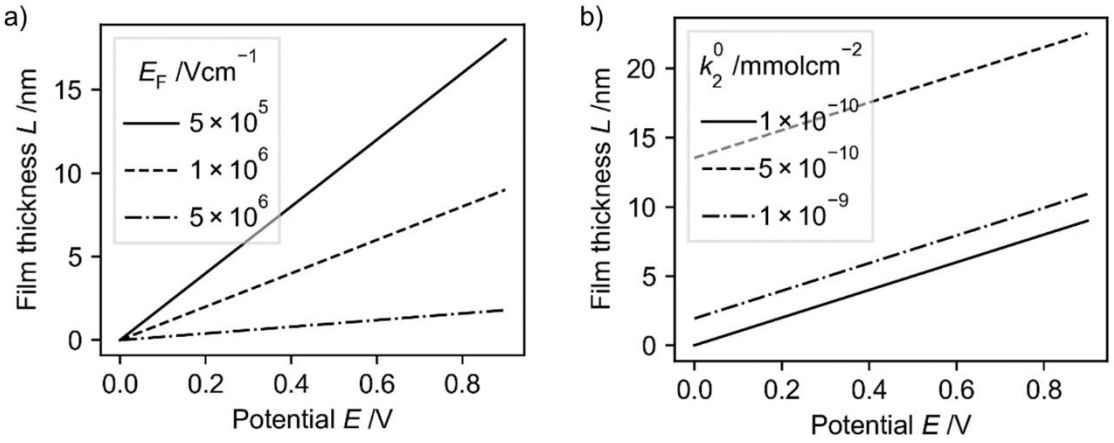

Figure 9-3: Dependency of passive film thickness on the potential for a) variing electric field strength $\boldsymbol{E_F}$ and b) variing standard rate constant of film formation $\boldsymbol{k_2^0}$.

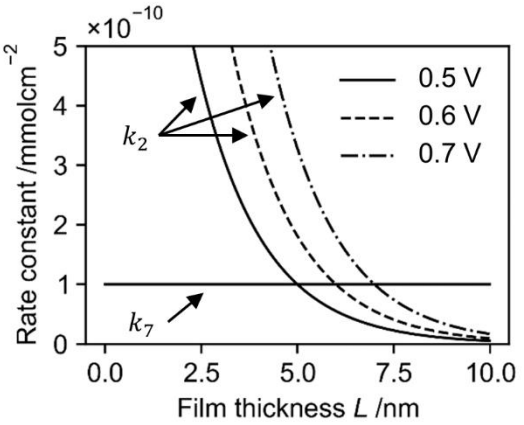

Figure 9-4: Dependency of the rate constants k_2 and k_7 under the assumption of a potential independent film dissolution reaction. Steady state is reached if both rate constants are equal.

9.2 Sensitivity of Passive Film Thickness

The effects of parameter changes on the passive film thickness are presented in Figure 9-2. Again, in every subfigure, one parameter is changed while the other parameters are kept constant analogues to the sensitivity analysis of the impedance data.

An increasing standard rate constant of film formation (k_2^0) leads to an increasing steady state film thickness while the time to reach steady state is not affected by the rate constant. In contrast, an increasing rate of film dissolution (k_7) leads to a thinning of the film with a faster reach of steady state. Increasing the charge transfer coefficient of film formation α_2 leads to a faster reach of steady state with a thinner passive film at the same time. Due to a lower potential drop across the passive film, a lower electric field strength results in a thicker passive film (whereas steady state is reached later).

The dependency of passive film thickness on the voltage is determined by the polarizability of the film/solution interface α and the electric field strength. An increase of electric field strength leads to a decreasing slope of passive film thickness over external potential (Figure 9-3a). The slope of film thickness over potential can be written as: $(1-\alpha)/E_{\mathrm{F}}$. A change of the other parameters (except α and E_{F}) does not affect the slope of passive film thickness over external potential (exemplified for k_2^0 in Figure 9-3b).

Under the assumption of a potential independent dissolution of passive film, but a potential dependent growth reaction, a potential increase does not affect the steady state rate constants $k_2 = k_7$ (Figure 9-4) but the steady state film thickness. If the steady state rate constants are not potential dependent, the passive current is also potential independent ($i_{\mathrm{pas}} = 3Fk_2^{\mathrm{ss}}$), which is consistent with the observations of nearly constant currents over the passive range for many metals [35,45].

9.3 Prediction of Corrosion Behavior

The steady state rate constants predict the dissolution of the investigated metals in the passivated state. This dissolution is related to the passive current density and the steady state corrosion rate under assumption of a passivated surface can be calculated by the rate constants. Not only the steady state behavior of metals and can be predicted, but also, statements about the passive film breakdown can be made.

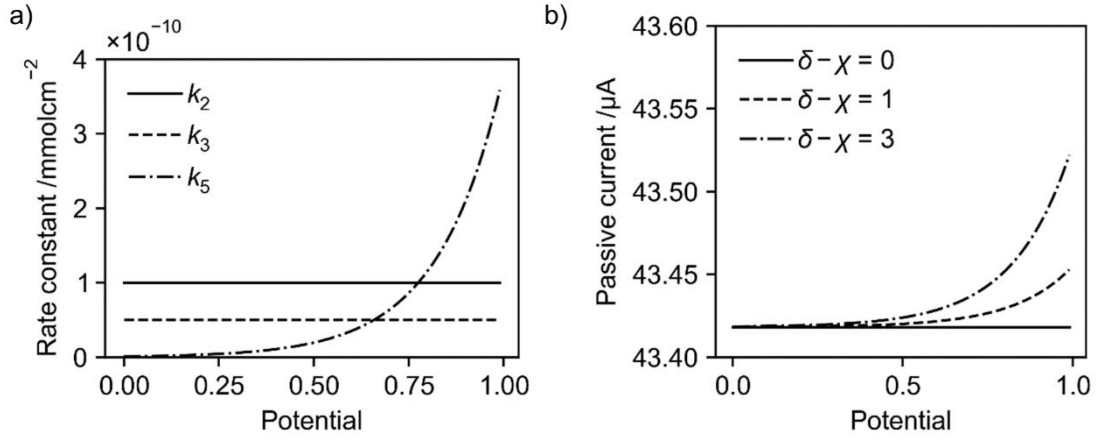

Figure 9-5: a) Dependency of possible reaction rate constants in a n-type oxide film on the applied potential. The steady state rate constant for passive film growth (Reaction 2) and the formation of interstitials (Reaction 3) are potential independent since a higher external potential leads to a thicker passive film and thus a higher potential drop over the film. The rate constant of the dissolution of interstitials (Reaction 5) at the film/solution interface increases with increasing potential. b) The resulting passive current depends on the charge difference of interstitials in the film and dissolved metal ions in solution. (Chosen parameters: k_2^0:10^{-10} mmols^{-1}cm^{-2}, α_2:0.05, k_3^0: 5×10^{-11} mmols^{-1}cm^{-2}, α_3:0.05, k_5^0: 10^{-12} mmols^{-1}cm^{-2}, α_5:0.05)

9.3.1 Passive Current Density

For the purpose of this thesis, it has been assumed that the only electrons generating reaction is the film growth reaction at the metal/film interface (Reaction 2). The steady state reaction rate of this reaction is independent of the applied potential and thus, the passive current, determined by the steady state rate constant $i_{\mathrm{pas}} = 3Fk_2^{\mathrm{ss}}$ is independent of the potential. Indeed, the potential affects the rate constant but so does the steady state film thickness. Initially, a higher potential leads to a faster dissolution of metal until a steady state is reached, at which point the metal dissolution always equals the (potential independent) film dissolution (compare Figure 9-4).

Under the assumption of additional electrons generating reactions, for example the generation of metal interstitials (Reaction 3) and the dissolution of metal interstitials (Reaction 5), the steady state current (passive current) is determined by additional reactions. All steady state reactions constants at the metal/film interface are potential independent. A higher external potential leads to a thicker passive film and thus a higher potential drop over the film. This finally leads to a constant potential drop at the metal/film interface. In contrast, the reactions at the film/solution interface show potential dependencies (Figure 9-5a). The passive current depends on all electrons generating reactions. In case of the dissolution reactions at the film/solution interface (for example Reaction 5: $\mathrm{Me_i} \rightarrow \mathrm{Me}^{\delta+} + (\delta - \chi)\mathrm{e}^-$) the passive current also depends on the ionic charge difference of the dissolved metals δ and the metal atoms in the oxide χ. If the charge difference is zero, the reaction does not affect the passive current. With increasing charge difference $\delta - \chi$, the effect of the reaction increases (Figure 9-5). That does not necessarily mean that there is no (nearly) constant current region in the passive state. Depending on the standard rate constant (or the equilibrium potential), the effect of the reaction can only be noticed at high potentials. This would mean, an increasing current, while the surface is actual still passivated, is possible.

9.3.2 Passivity Breakdown

A breakdown of passivity under the assumptions made in Chapter 3 and Chapter 4 (especially the independents of the film dissolution reaction on the external potential and the considered reactions) is not possible. The passive film would just linearly grow with increasing potential. Indeed, a linear dependency of passive film thickness on applied potential is observed over a broad potential range for many metals [62,70,74,136]. But if the potential exceeds a specific potential (transpassive potential E_{tp}), the passive film breaks and active dissolution takes place. This can be due to the presence of halide ions (for example Cl^-) or due to the further oxidation of the present metal oxides. One possible reaction for stainless steels is the oxidation of the present chromium (III) oxides to soluble chromium (VI) oxides:

$$2Cr_2O_3 + 4H_2O + 3O_2 \rightarrow 4CrO_4^{2-} + 8H^+ \qquad 9\text{-}1$$

Or following the notation of the PDM Reaction 7

$$2Cr_2O_3 + 6H^+ \rightarrow 2Cr^{6+} + 3H_2O + 6e^- \qquad 9\text{-}2$$

Since the oxidation state of chromium increases from 3 to 6 this reaction is strongly potential dependent. A potential dependency of passive film breakdown due to chloride ions is also observed. Considering a high equilibrium potential for the film breakdown reaction, which I will from now on refer to as Reaction 7.2 (with reaction constant k_7^2), the previous considerations (which match with observations of measurements), linear passive film growth during a broad potential range in the passive area and constant passive current density, still applies. In the case of the kinetic parameters of reaction 7.2 (listed in Table 9-2), the film breakdown reaction does show nearly no effect on the reaction system up to a potential of ca. 0.8 V (Figure 9-6a). At a potential of 0.97 V, the breakdown reaction is faster compared to the film formation reaction and the passive film is totally dissolved (Figure 9-6b).

Between these potentials (in this case 0.8 V and 0.97 V), the increase of the film breakdown reaction leads to a thinning of the passive film. The thinning of the film increases the rate constant of the film formation and thus leads to a steep increase of current (even before the passive film is completely dissolved). This coincides with the observed increase of current in the transpassive area [35] (Figure 9-7a). On the region of linear passive film growth follows, with increasing potential a region of steep passive film dissolution, which results in passive film breakdown (Figure 9-7b).

Table 9-2: Parameter of additional film dissolution reaction in the transpassive region.

$k_7^{2;0}$ /mmolcm^{-2+}s^{-1}	α_7	E_0 /V
10^{-10}	0.4	0.8

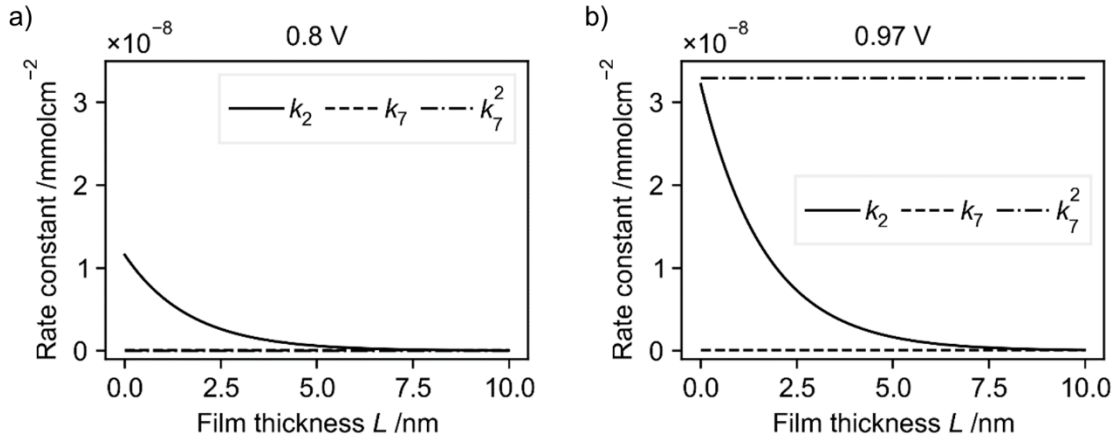

Figure 9-6: Rate constant of film formation reaction and a potential independent ($\boldsymbol{k_7}$) and potential dependent ($\boldsymbol{k_7^2}$) film dissolution reaction depending on film thickness. Crossing of film formation with the sum of film dissolution marks the steady state. a) at 0.8 V, nearly no effect of the second film dissolving reaction is noticeable and b) at 0.97 V the passive film is completely dissolved because the rate constant of potential dependent film dissolution $\boldsymbol{k_7^2}$ exceeds the film formation.

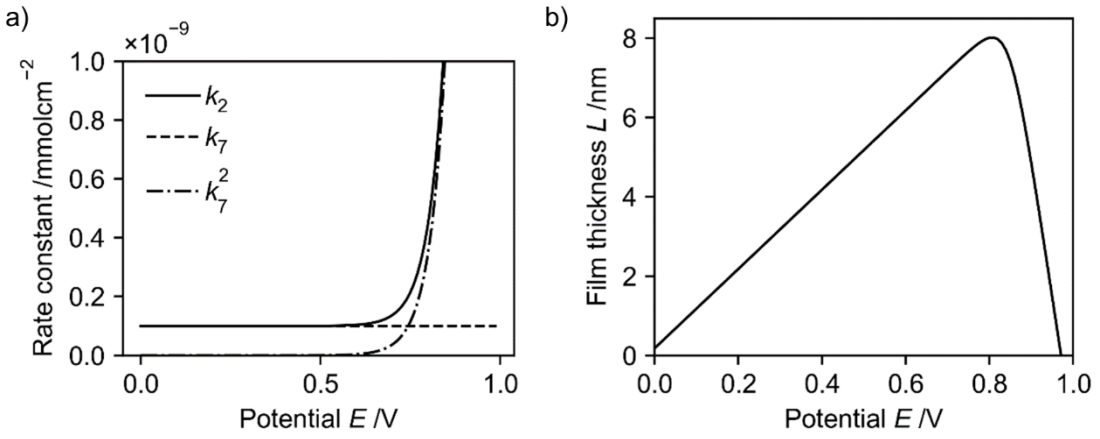

Figure 9-7: a) Rate constant of film formation reaction and a potential independent ($\boldsymbol{k_7}$) and potential dependent ($\boldsymbol{k_7^2}$) film dissolution reaction depending on the applied potential; b) resulting film thickness depending on the potential.

Both, the rate of film formation k_2 depending on the charge transfer coefficient α_2 and the standard rate constant k_2^0, and the rate constant of film breakdown (k_7/k_7^2) influence the passive film breakdown. Increasing α_2 and k_2^0 values leads to higher breakdown potential (Figure 9-8a). This behavior can lead to, as described in Chapter 6, seemingly contrary behavior of a lower passive current density, which indicates a slower dissolution in the passivated state, and an earlier passive film breakdown due to pitting corrosion.

The film breakdown reaction depends on the passive film characteristics like defect densities and element distributions. The breakdown mechanism can be much more complex than described here. Transport and adsorption phenomena can play a crucial role for film breakdown and in the case of local corrosion (for example pitting corrosion) the breakdown

of passivity can occur on local places of the passive film and not over the whole film. For a more detailed investigation of these effects by the PDM, a 2-dimensional passive film with heterogeneous potential and defect distribution, resulting in heterogeneous (depending on the passive film coordinate) rate constants can be the next step towards a comprehensive modeling of film growth and breakdown.

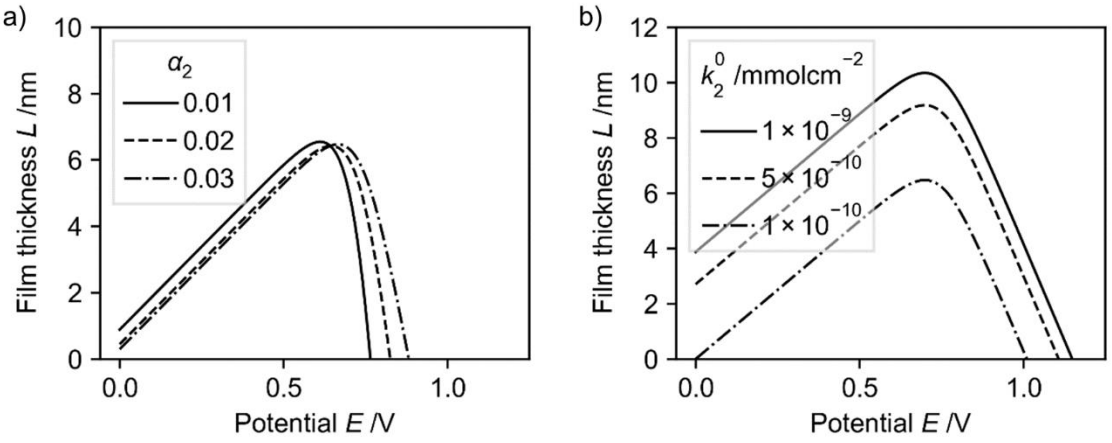

Figure 9-8: Variation of passive film thickness considering a potential dependent breakdown mechanism; a) influenced by the charge transfer coefficent of film formation and b) the standard rate constant of film formation.

10

SUMMARY AND OUTLOOK

Get your facts first,
then you can distort them as you please
Mark Twain

The previous chapter presented the results of electrochemical measurements and modeling of passive film growth of differently treated materials. Although each test series has been examined for itself, it can be very helpful to compare the findings of the different materials. In particular, the comparison could give an answer whether the same microstructure affects the electrochemical (and passive film growth) behavior of different alloys in the same way.

I will start with a detailed summary of the measurement results and their interpretation with the help of the PDM and the scientific literature. In conclusion, I will critically examine the results and the interpretations derived from them. As discussed in Chapter 4, a complete parameterizing of the PDM is not possible by EIS measurements alone. At the end of this chapter, I will present some possibilities for a more comprehensive parameterization.

10.1 Summary and Conclusion

Starting points of the research work of this thesis were the contrary works about the influence of heat treatment on martensitic stainless steel and the idea of resolving it with the help of kinetic models of passive film growth. Repeating the discussed heat treatment and subsequent electrochemical analysis in form of LSV measurement could already show that it is necessary to distinguish between different corrosion phenomena. On the one hand, the increased chromium content with rising austenitizing temperatures, due to the dissolution of carbides and the more homogenous chromium distribution, could decrease the passive current and increase the critical potential. Both circumstances indicate slower dissolution, the decreased passive current in the passivated state and the increased critical potential during transpassive dissolution due to pitting. On the other hand, the pitting potential, indicating the starting point of passive film breakdown, decreased with rising austenitizing temperatures. This leads to the conclusion of an earlier passive film breakdown in the presence of halide ions. This behavior was explained with increasing lattice distortions due to an increased amount of carbon stored in the martensitic lattice structure [1].

Indeed, these observations explain the seemingly contrary results of different investigations [1–4] due to the different methods that were used; nevertheless, it is surprising that both related phenomena behave so differently and the physical cause was also not entirely clear. Determinations of the kinetic parameters of passive film growth based on a reduced form of the Point Defect Model could clearly show that the standard rate constant of film formation k_2^0 and the rate constant of film dissolution k_7 decrease with increasing austenitizing temperatures and thus increasing chromium content. (It is important to remember both constants are summed up from two reactions: The reaction of iron and chromium from the metal to the film (k_2^0) and the dissolution of iron oxides and chromium oxides of the film to the solution (k_7)). As both constants decrease with increasing chromium content, it can be concluded that the reaction of chromium to chromium ions in the passive film as well as the dissolution of chromium oxides is slower compared to the reaction of iron to the film and the dissolution of iron oxides from the film to the solution. The lower dissolution of chromium rich oxide films is in accordance with literature [137,138]. The decreasing rate constants deliver a clear explanation for the decreasing passive current density (lower k_7), as well as decreasing dissolution in the active state (lower k_2^0).

The observed decreasing pitting potential (and thus earlier breakdown of passivity in presence of halide ions) can also be explained by kinetic modeling. The thinning of the layer with increasing austenitizing temperatures on the one hand and the decreasing standard rate constant of film formation on the other hand are both related to the observed phenomenon.

In case of all mechanisms leading to pitting corrosion (penetration mechanism, film breakdown mechanism and adsorption mechanism), a thinner passive film leads to a faster breakdown. In fact, the sensitivity analysis of passive film breakdown due to a potential depending breakdown mechanism could confirm a faster breakdown with decreasing film formation reaction and thinner passive film. Considering this analysis, the observed contrary mechanism can be explained by means of the PDM.

Candelaria *et al.* addressed their observations (increasing weight loss due to pitting), which correspond to the observation of decreasing pitting potential, to the increasing lattice distortion due to the carbon saturation inside the lattice. Following this reasoning, it can be concluded that the crystal lattice distortions increase the charge transfer coefficient, which in turn leads to the thinning of the passive film. This explanation sounds reasonable, but it remains speculative.

Transferring the results to another alloy system was not identically possible. However, this is not due to the insufficient validity of the results, but rather due to different microstructure changes as a consequence of the same heat treatment on another alloy. It is therefore important to compare the resulting microstructural properties and not just the material treatment when comparing the corrosion behavior of different materials. The austenitizing of the bearing steel AISI 52100 leads to martensite content changes, dissolution of carbides (although with a higher iron and lower chromium content compared to the martensitic stainless steel) and grain growth. The effect of increased carbon content due to carbide dissolution appears to be similar to the effect observed in martensitic stainless steel and is indicated by decrease of the pitting potential at 850 °C (dissolution of M_7C_3 carbides) and 1050 °C (dissolution of M_3C carbides). But the effects are clearly less pronounced and a dependence of carbide dissolution on the charge transfer coefficient α_2 could not be observed.

The martensite content shows the main effect on the electrochemical properties. An increasing martensite content seems to increase the dissolution at the metal/film interface in terms of the standard rate constant k_2^0 and increases the film dissolution, visible by an increase of the rate constant k_7. Martensitic structure shows higher lattice distortions (leading to a higher hardness) which seems to affect the rate constant at the metal/film interface, on the one hand. The lattice distortions in the bulk material seem to lead to defects in the passive film and to a higher film dissolution, on the other hand. In contrast to the martensitic stainless steel, it is not likely that the change of film dissolution is a product of varying chromium content but rather of the differing passive film structure.

Nevertheless, the effect was overlaid by the already discussed additional microstructure changes and to verify this assumption and to test the generality of this observation, the martensite content of an additional alloying system (austenitic stainless steel AISI 304) has been systematically changed (leaving all other microstructure parameters constant) and the kinetic parameters of passive film growth have been determined. It could be shown that an

increasing martensite content indeed increases the standard rate constant of film formation, as well as the rate constant of film dissolution. This accelerated dissolution at the metal/film interface is probably due to the increased lattice distortions. The increased dissolution of the passive film itself must have its origin in the film itself. Since the chromium content should be the same, the higher number of defects inside the passive film (which could be measured by MS analysis) seems to be the cause of the accelerated film dissolution. A higher defect density is the result of accelerated metal dissolution with unchanged vacancies consumption.

Furthermore, the charge coefficient α_2 of film formation decreases with increasing martensite content. This result is somehow surprising, as it predicts a smaller increase in reaction rate with increasing potential. But it explains why in case of the bearing steel no dependence of the charge transfer coefficient on carbide dissolution could be observed. The charge transfer coefficient seems to be affected by several microstructure properties.

The combination of electrochemical measurements and modeling based on the PDM provides informative insights into the physical causes of microstructure changes. Nevertheless, some explanations remain hypotheses and additional analysis might be necessary to verify those. In particular, it should be taken into account that the model was shortened in order to enable the fitting by the measurements at all. It is still not possible to distinguish the contribution of single metal dissolutions (iron or chromium for example) to the overall impedance. This does not necessarily reduce comparability, but additional electrochemical processes (for example the formation of interstitials) could possibly occur. The insights shown here are unique, because it was the first time kinetic passive film growth modeling has been used to describe the influence of material treatments on corrosion. Furthermore, this procedure of combined modeling and measurements shows a great potential for material science research in the area of corrosion and oxide film growth kinetics. Possibilities to parametrize a more complex Point Defect Model with the help of additional techniques are discussed in the following section.

10.2 Outlook

It has been shown that the PDM in combination with electrochemical measurements is a strong tool to compare corrosion behavior of metals, explain seemingly contrary behaviors, to gain insight into the physical causes of differing corrosion behavior and to predict long-term corrosion properties. For the purpose of this thesis, a simplification of the complete PDM was done. Despite the simplification, physically reasonable results could be achieved, the question of the observed contrary behavior could be answered satisfactorily and the impact of single microstructure parameters on passivity could be investigated.

However, it was necessary to reduce the model because the impedance data obtained was

not sufficient to fit the complete model without the risk of overfitting. Chapter 4 presented why it is not possible to overcome this issue with impedance measurements alone. Nevertheless, with the use of additional measurement techniques, it could be possible to parametrize a more comprehensive model. Some possibilities will be presented in this section.

Surface characterization methods can be used to analyze the passive film regarding its element composition. With the help of XPS measurements, the element ratio of the film can be analyzed. XPS measurements alone would not be sufficient to distinguish the film formation current regarding the different elements. This is because the dissolution of the different metal oxides also differs. Thus, the element content inside the film does not necessarily represent the reaction ratio of the elements at the metal/film interface. But by combining the element ratio in the film with an analysis of the dissolved metals during stable passivity, for example via UV-vis, it would be possible to distinguish the currents regarding the reaction of different elements.

A further possibility to distinguish between passive film formation and how much of the film dissolves during polarization is via electrochemical quartz crystal microbalance [139]. Using this technique, it is possible to measure the mass increase on a sample during polarization and thus it is possible to determine the passive film growth. This would be especially helpful for the determination of reaction rate constant k_7 (film dissolution), assuming the theory of a potential independent film dissolution is correct.

In this thesis, the passive film thickness was calculated based on the measured capacity and of the electrode surface. With XPS, Ellipsometry or TEM measurements, the film thickness can also be determined, which allows an additional description of the film thickness. By choosing the correct electrochemical active surface (compared to the geometrical surface) it is possible to adjust the calculated film thickness to the determined values. An example of passive film thickness determination by TEM measurements is given in Section A7.

Furthermore, it is possible to perform MS analysis after polarization on different potentials to determine the diffusion coefficient of the point defects inside the film [140] for a more complete parameterizing of the model. An example of this is given in Section A5.

The PDM only describes the passive film growth in the passivated state. To understand the full phenomenon of passivity a more detailed description of the active/passive region and the transpassive region would be necessary. First steps regarding the description of the transpassive dissolution based on a model similar to the PDM have already be done [69]. A combination of the above presented techniques and the modeling via an extended PDM in the active/passive and transpassive region is still pending. Especially, the active/passive to passive transformation seems to be interesting, since the transformation must include a transition between no passive film, a passive film without full protection and the fully developed passive film described by the PDM. An investigation of this state could be done using a com-

bination of potential hold experiments at different potentials in the active/passive region until steady state is reached, while the mass changes are investigated by EQCM. This would be followed by impedance measurements to reveal the nature of the reactions (for example diffusion controlled) and the change of the properties of the transition film.

With this combination of different measurement techniques, a more comprehensive version of the PDM could be parametrized. This will give the opportunity of an even deeper understanding of passivity and the influence of several microstructure parameters on the passive behavior, the corrosion resistance and the breakdown of passive films. Thereby, it is possible to develop materials regarding their mechanical and corrosion properties. A more comprehensive understanding of these factors is the next step for the development of sustainable long-lasting steels and construction materials for a wide variety of applications.

APPENDIX

A1. ELECTROLYTE COMPOSITION

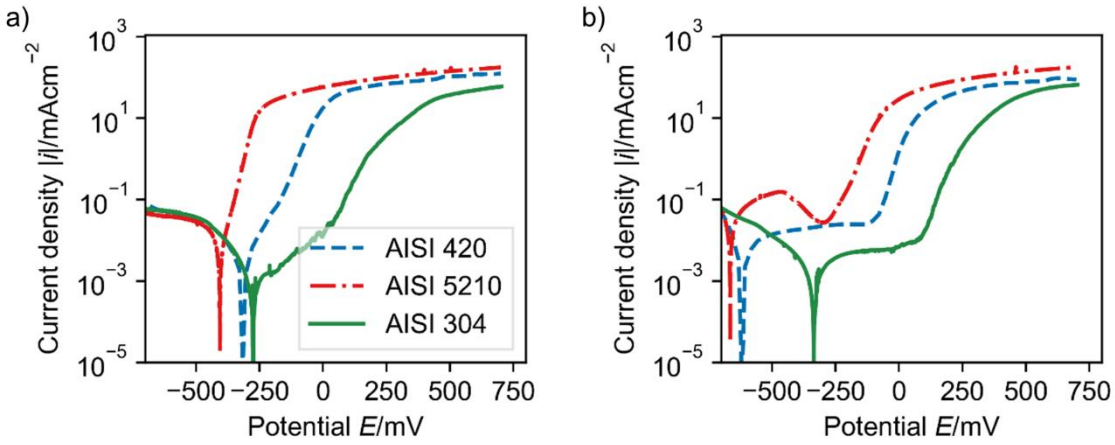

Figure A-1: LSV measurement of the martensitic steel (AISI 420), the bearing steel (AISI 5210) and the austenitic steel (AISI 304) in a) sodium chloride and b) phosphate buffered sodium chloride.

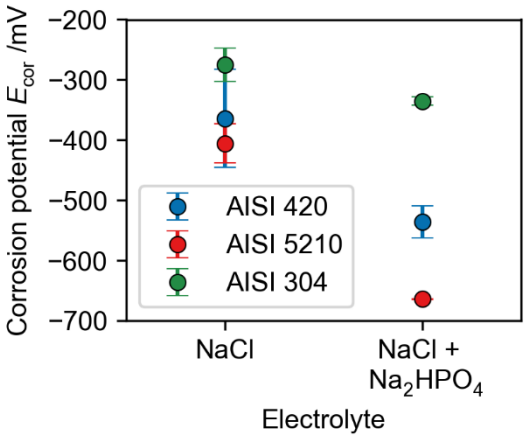

Figure A-2: Corrosion potential determined in different electrolytes.

The LSV measurements in 0.1 M sodium chloride solution and 0.1 M phosphate buffered sodium chloride show clear differences. The passive region is more pronounced and it is possible to distinguish between metastable and stable pit growth in the phosphate buffered solution (Figure A-1). The corrosion potential is better to distinguish in the phosphate buffered solution and the standard deviation of three independent measurements is smaller (Figure A-2).

A2. Analysis of LSV Measurements

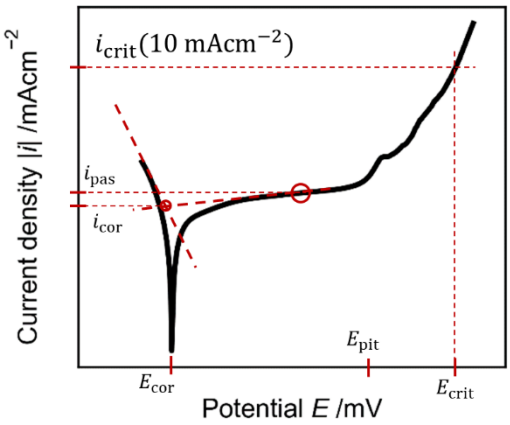

Figure A-3: Example LSV for the determination of the corrosion values.

The corrosion current i_{cor} is determined by the tafel method. The intersection of the tangents of the linear part around the equilibrium current ($i_{absolute}$ = 0) marks the corrosion current. The corrosion potential E_{cor} is the potential at which the sum of the absolute currents equals zero. The passive current i_{pas} is obtained in the passive region. The pitting potential E_{pit} marks the start of the step current increase due to pitting corrosion. The critical potential E_{crit} marks the point at wehich the current density exceeds a specific value (10 mAcm^{-2} in this thesis).

A3. Sample Pretreatment

The surface preparation of the samples can have a strong effect on the electrochemical measurements. To minimize the effect and to determine the pretreatment with the smallest standard deviation different surface preparations were compared. For this purpose cyclic

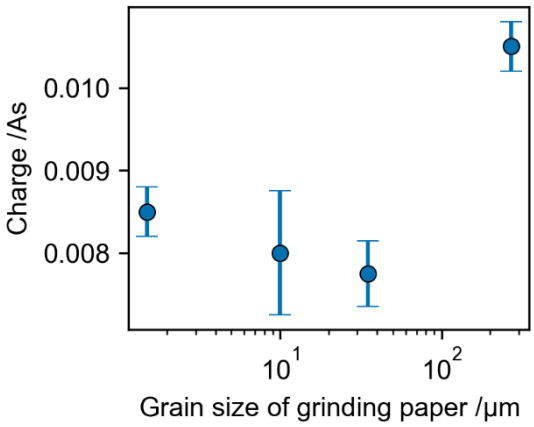

Figure A-4: Charge during anodic scan of martensitic stainless steel in 0.5 M sulfuric acid after polishing with different grinding papers. Standard deviations of three independent measurements.

voltammograms of martensitic stainless steel AISI 420 with different surface treatment are performed in sulfuric acid and the charge during anodic scan is compared (Figure A-4).

The standard deviation of three different measurements reveal nearly no difference between the single surface pretreatments. Because the surface treatment with the highest grain size needs the less preparation steps this pretreatment was chosen.

A4. KINETIC CONSTANTS ARTIFICIAL MATERIAL

Parameter	Value	Unit
χ	3	
δ	2	
E_F	10^6	V/cm
β	-0.005	
α	0.7	
k_2^0	10^{-13}	mol/(cm²s)
k_3^0	10^{-14}	mol/(cm²s)
α_2	0.1	
α_3	0.1	
k_7	10^{-13}	mol/(cm²s)

A5. DEFECT CONCENTRATION N-DOPED PASSIVE FILMS

The defect concentration inside the passive film on bearing steel passivated at 0.9 V in 0.5 M sulfuric acid is presented in A-5. The defect concentration is calculated by the Nernst-Planck equation:

$$J_d = -D_d \frac{\partial c_d}{\partial x} + \frac{z_d F D_d}{RT} E_F c_d \qquad 10\text{-}1$$

Furthermore, the flux of defects J can be calculated by the rate constant presented in Chapter 7. The diffusion coefficient is determined by MS-Analysis after polarization on different potentials. According to Sikora *et al.* [140] the diffusion coefficient can be calculated by:

$$N_D = \omega_1 \exp(-bE_{ext})\, \omega_2$$

ω_1, ω_2 and b can be determined by the experimental data.

The diffusion coefficient can be calculated by:

$$D_d = \frac{J_d}{2K\omega_2}$$

with $K = FE_{Field}/(RT)$. The calculated diffusion coefficient by the data presented in Figure A-5 is 1.11×10^{-16} cm²/s, which is in very good agreement with literature [89]. Based on the diffusion coefficient and the rate constants calculated in Chapter 7 the defect densities are calculated. The defect densities are nearly constant over a broad range of the film and decreases steeply in the near of the film/solution interface. At this interface the defects are consumed.

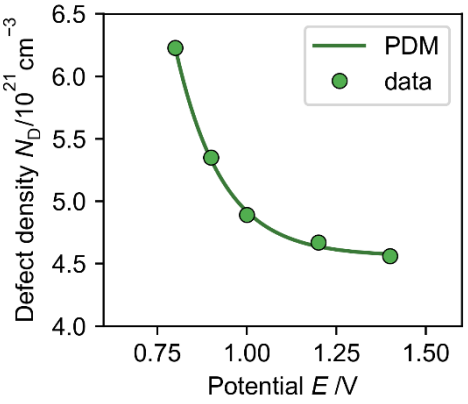

Figure A-5: Defect densities of passive films formed on bearing steel AISI 5210 at different potentials.

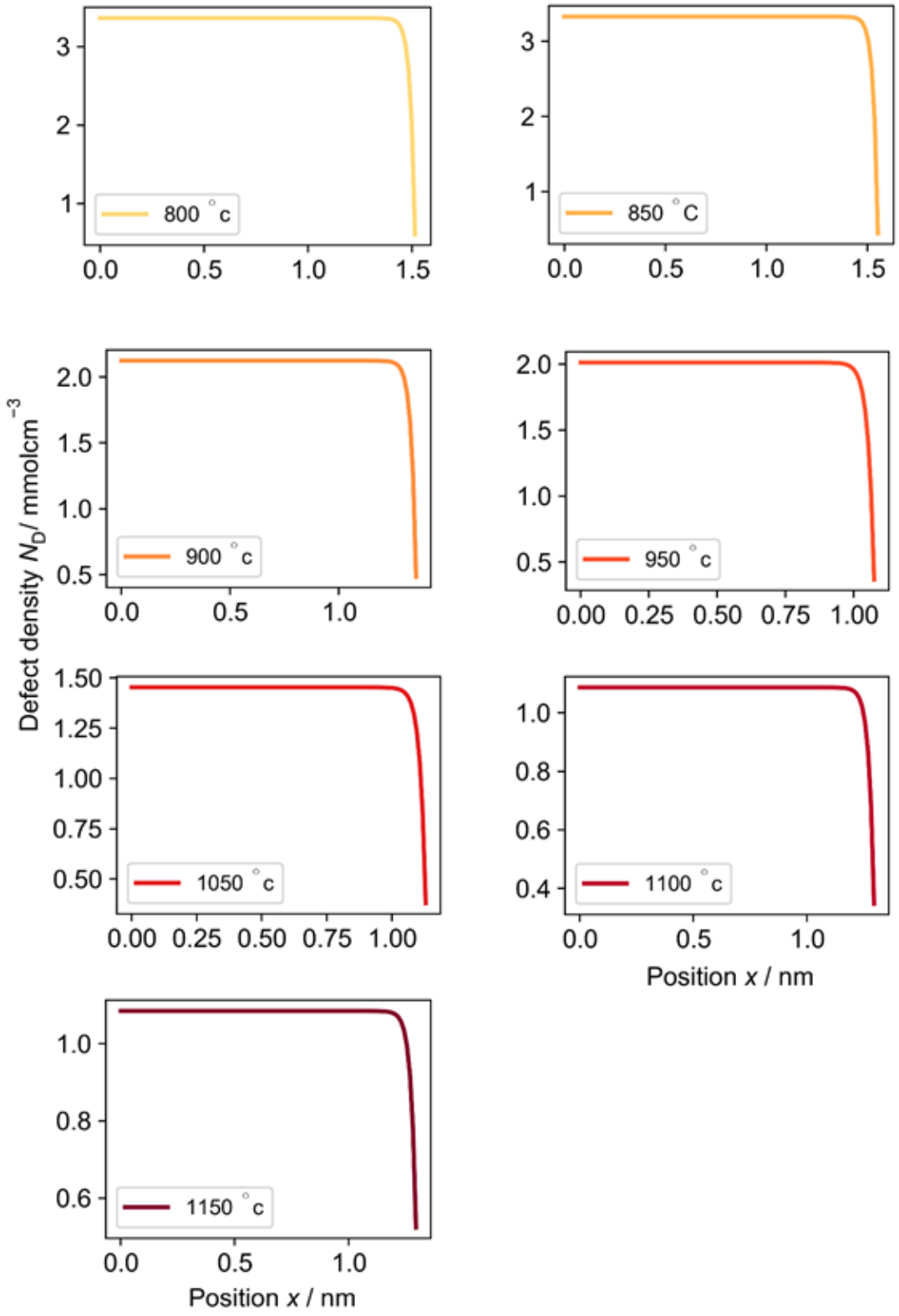

Figure A-6: Calculated defect densities of passive film formed on bearing steel AISI 5210 austinitized on different temperatures.

A6. DOUBLE LAYER EEC PARAMETER

Table A-1: CPE parameter describing the double layer during EIS measurements of martensitic stainless steel presented in Chapter 6.

T_A / °C	Y_{CPE} /$\Omega cm^{-2}s^N$	N
T_0	5.71×10^{-4}	0.858
1000	2.91×10^{-4}	0.969
1050	2.01×10^{-4}	0.905
1100	2.52×10^{-4}	0.945
1150	2.74×10^{-4}	0.804
1200	3.56×10^{-4}	0.906

Table A-2: Double layer capacity determined by EIS measurements of bearing steel in 0.5 M H_2SO_4 presented in Chapter 7.

T_A / °C	C_{dl} /Ccm^{-2}
800	9.11×10^{-5}
850	1.05×10^{-4}
900	2.19×10^{-4}
950	4.11×10^{-4}
1050	1.78×10^{-4}
1100	9.62×10^{-4}
1150	7.95×10^{-4}

A7. TEM MEASUREMENTS

The determination of passive film thickness formed on bearing steel in sulfuric acid is shown in Figure A-7. A combination of imaging by TEM and elements determination based on EDX measurements leads to an element profile across the film. The ratio of oxygen and iron is used to determine the passive film thickness. In an oxide film consisting solely of Fe_2O_3 the O/Fe ratio would be 60/40. For this imaging, it is assumed that the passive film exists if at least half of the "full" ratio is present (30% oxygen). Of course, this is a very rough approximation but it can be seen that the active surface might be adjusted compared to the geometrical surface. This would just affect the absolute values of some kinetic parameters

but would not affect the ratio of the parameters of the different samples.

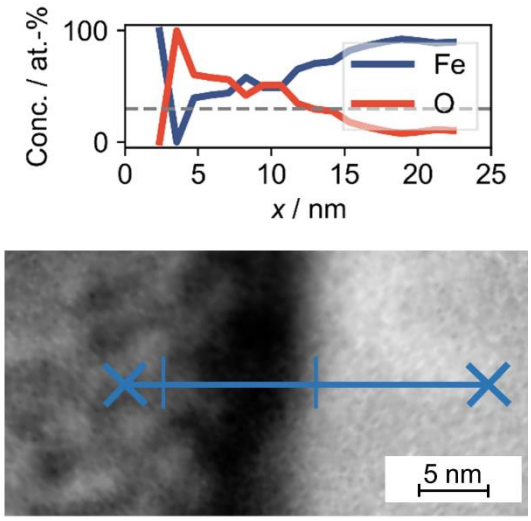

Figure 10-1: EDX analyses of the elements inside the passive film and imaging of the passive film via thin film TEM.

BIBLIOGRAPHY

[1] A.F. Candelaria, C.E. Pinedo, Influence of the heat treatment on the corrosion resistance of the martensitic stainless steel type AISI 420, *J. Mater. Sci.* 22 (2003) 1151–1153.

[2] P. Rosemann, N. Kauss, C. Müller, T. Halle, Influence of solution annealing temperature and cooling medium on microstructure, hardness and corrosion resistance of martensitic stainless steel X46Cr13, *Mater. Corros.* 66 (2015) 1068–1076.

[3] T. Müller, A. Heyn, M. Babutzka, P. Rosemann, Examination of the influence of heat treatment on the corrosion resistance of martensitic stainless steels, *Mater. Corros.* 66 (2015) 656–662.

[4] S.Y. Lu, K.F. Yao, Y.B. Chen, M.H. Wang, Y. Shao, X.Y. Ge, Effects of austenitizing temperature on the microstructure and electrochemical behavior of a martensitic stainless steel, *J. Appl. Electrochem.* 45 (2015) 375–383.

[5] S.Y. Lu, K.F. Yao, Y.B. Chen, M.H. Wang, N. Chen, X.Y. Ge, Effect of quenching and partitioning on the microstructure evolution and electrochemical properties of a martensitic stainless steel, *Corros. Sci.* 103 (2015) 95–104.

[6] Y.S. Choi, J.G. Kim, Y.S. Park, J.Y. Park, Austenitizing treatment influence on the electrochemical corrosion behavior of 0.3C-14Cr-3Mo martensitic stainless steel, *Mater. Lett.* 61 (2007) 244–247.

[7] A.N. Isfahany, H. Saghafian, G. Borhani, The effect of heat treatment on mechanical properties and corrosion behavior of AISI420 martensitic stainless steel, *J. Alloys Compd.* 509 (2011) 3931–3936.

[8] J. Müller, J. Müller, WBG Weltgeschichte. Eine globale Geschichte von den Anfängen bis ins 21. Jahrhundert, Band I: Grundlagen der globalen Welt, A. Jockenhövel, (2009).

[9] S. Milisauskas, S. Milisauskas, European Prehistory A Survey, Kluwer Academic/Plenum Publisher, New York, (2002).

[10] D. Raabe, Geschichte der Metall - 600 Jahre Hochtechnologie, in: Morde, Macht, Monet. Met. Zwischen Myth. Und Hightech, 1st ed., Dierk Raabe, Düsseldorf, (2001) 57–75.

[11] A. Jockenhövel, Der Weg zum Hochofen, in: Eisenland, Zu Den Wurzeln Der Nassau. Eisenindustrie, Verein für Nassauische Altertumskunde und Geschichtsforschung e. V, Taunusstein, (1995).

[12] U. Wengenroth, Eisen, Stahl und Buntmetalle, in: Tech. Und Wirtschaft, VDI Verlag, Düsseldorf, (1993) 161–163.

[13] Sued-hansa, Korrosionsschutz, n.d.

[14] I. Bösing, L. Cramer, M. Steinbacher, H.W. Zoch, J. Thöming, M. Baune, Influence of heat treatment on the microstructure and corrosion resistance of martensitic stainless steel, *AIP Adv.* 9 (2019) 065317.
[15] I. Bösing, G. Marquardt, J. Thöming, Effect of Heat Treatment of Martensitic Stainless Steel on Passive Layer Growth Kinetics Studied by Electrochemical Impedance Spectroscopy in Conjunction with the Point Defect Model, *Corros. Mater. Degrad.* (2020) 1–15.
[16] I. Bösing, M. Herrmann, I. Bobrov, J. Thöming, B. Kuhfuss, J. Epp, M. Baune, The influence of microstructure deformation on corrosion resistance of cold formed stainless steel the, *MATEC Web Conf.* 04002 (2018) 1–8.
[17] I. Bösing, I. Bobrov, J. Epp, M. Baune, J. Thöming, Influence of Systematically Changed Martensite Content on the Passive Film Properties of Austenitic Stainless Steel in Neutral Electrolyte, *Int. J. Electrochem. Sci.* 15 (2020) 319–333.
[18] C.H. Hamann, W. Vielstich, C.H. Hamann, W. Vielstich, Elektrochemie, 4th ed., WILEY-VCH, (2005).
[19] D. Landolt, D. Landolt, Corrosion and surface chemistry of metals, CRC Press, (2007).
[20] J. Newman, K.E. Thomas-Alyea, J. Newman, K.E. Thomas-Alyea, Electrochemical Systems, 3rd ed., John Wiley & Sons, (2012).
[21] M.E. Orazem, B. Tribollet, M.E. Orazem, B. Tribollet, Electrochemical Impedance Spectroscopy, 2nd ed., John Wiley & Sons, (2017).
[22] D. Landolt, D. Landolt, Corrosion and surface chemistry of metals.pdf, 1st ed., EPFL Press, Lausanne, Switzerland, n.d.
[23] a Bard, L. Faulkner, Allen J. Bard and Larry R. Faulkner, Electrochemical Methods: Fundamentals and Applications, New York: Wiley, 2001, *Russ. J. Electrochem.* 38 (2002) 1505–1506.
[24] P. Marcus, F.B. Mansfeld, P. Marcus, F.B. Mansfeld, Analytical methods in corrosion science and engineering, CRC press, (2005).
[25] D.S.M. Vishnu, N. Sanil, K.S. Mohandas, Measurement of Counter Electrode Potential during Cyclic Voltammetry and Demonstration on Molten Salt Electrochemical Cells, 15 (2017) 1–13.
[26] R.G. Compton, C.E. Banks, R.G. Compton, C.E. Banks, Understanding Voltammetry, World Scientific, (2007).
[27] H. Cesiulis, N. Tsyntsaru, A. Ramanavicius, G. Ragoisha, The study of thin films by electrochemical impedance spectroscopy., in: Nanostructures Thin Film. Multifunct. Appl., Springer, (2016) 3–42.
[28] A.D. King, N. Birbilis, J.R. Scully, Accurate electrochemical measurement of magnesium corrosion rates; A combined impedance, mass-loss and hydrogen collection study, *Electrochim. Acta*. 121 (2014) 394–406.
[29] C.M.A. Brett, The application of electrochemical impedance techniques to aluminium corrosion in acidic chloride solution, *J. Appl. Electrochem.* 20 (1990) 1000–1003.
[30] M. Keddam, Electrochemical Behavior of Passive Iron in Acid Medium, *J. Electrochem. Soc.* 131 (1984) 2016.
[31] M.E. Orazem, T. Bernard, Kinetic Models, in: Electrochem. Impedance Spectrosc., 48th ed., John Voley & Sons, (2011) 163–182.
[32] X.L. Zhang, Z.H. Jiang, Z.P. Yao, Y. Song, Z.D. Wu, Effects of scan rate on the

potentiodynamic polarization curve obtained to determine the Tafel slopes and corrosion current density, *Corros. Sci.* 51 (2009) 581–587.
[33] H.-J. Bargel, S. G., H.-J. Bargel, S. G., Werkstoffkunde, Springer-Verlag, (2008).
[34] P. Marcus, P. Marcus, Corrosion Mechanism in Theory and Practice, 2nd ed., Marcel Dekker, (2002).
[35] P. Schmuki, From Bacon to barriers: A review on the passivity of metals and alloys, *J. Solid State Electrochem.* 6 (2002) 145–164.
[36] J. Soltis, Passivity breakdown, pit initiation and propagation of pits in metallic materials - Review, *Corros. Sci.* 90 (2015) 5–22.
[37] U.R. Evans, The passivity of metals. Part I. The isolation of the protective film, *J. Chem. Soc.* (1927).
[38] D.D. Macdonald, The Point Defect Model for the Passive State, *J. Electrochem. Soc.* 139 (1992) 3434.
[39] T.P. Hoar, The production and breakdown of passivity of metals, *Corros. Sci.* 7 (1967).
[40] P. Schmuki, From Bacon to barriers: A review on the passivity of metals and alloys, *J. Solid State Electrochem.* 6 (2002) 145–164.
[41] J. Kruger, Passivity of metals – a materials science perspective, *Int. Mater. Rev.* 33 (1988) 113–130.
[42] J. Keir, Experiments and Observations on the Dissolution of Metals in Acids, and their Precipitations, *Phil. Trans. R. Soc.* 80 (1790).
[43] C.F. Schönbein, Über das Verhalten des Zinns und des einsens gegen die Salpetersäure, *Ann. Phys.* 37 (1836).
[44] H.H. Uhlig, PASSIVITY IN METALS AND ALLOYS, *Corros. Sci.* 19 (1979) 777–791.
[45] H.H. Strehblow, Passivity of Metals Studied by Surface Analytical Methods, a Review, *Electrochim. Acta*. 212 (2016) 630–648.
[46] M. Orlik, M. Orlik, Self-Organization in Electrochemical Systems I, 1st ed., Springer-Verlag, (2012).
[47] H.-J. Rocha, H.-J. Rocha, Archiv für das Eisenhüttenwesen, 26th–117th ed., (1955).
[48] C.-O.. Olsson, D. Landolt, Passive films on stainless steels—chemistry, structure and growth, *Electrochim. Acta*. 48 (2003) 1093–1104.
[49] S. Qian, R.C. Newman, R.A. Cottis, K. Sieradzki, Computer simulation of alloy passivation and activation, *Corros. Sci.* 31 (1990) 621–626.
[50] Sieradzki, Newman - A Percolation Model for Passivation in Stainless Steels - Verknüpfung, n.d.
[51] A. Veluchamy, D. Sherwood, B. Emmanuel, I.S. Cole, Critical review on the passive film formation and breakdown on iron electrode and the models for the mechanisms underlying passivity, *J. Electroanal. Chem.* 785 (2017) 196–215.
[52] S.P. Harrington, F. Wang, T.M. Devine, The structure and electronic properties of passive and prepassive films of iron in borate buffer, *Electrochim. Acta*. 55 (2010) 4092–4102.
[53] R. Jiang, Y. Wang, X. Wen, C. Chen, J. Zhao, Effect of time on the characteristics of passive film formed on stainless steel, *Appl. Surf. Sci.* 412 (2017) 214–222.
[54] D.D. Macdonald, Passivity–the key to our metals-based civilization, *Pure Appl. Chem.* 71 (1999) 951–978.
[55] Z. Bou-Saleh, A. Shahryari, S. Omanovic, Enhancement of corrosion resistance of a

biomedical grade 316LVM stainless steel by potentiodynamic cyclic polarization, *Thin Solid Films*. 515 (2007) 4727–4737.
[56] D. Vanmaekelbergh, W.P. Gomes, Impedance Spectroscopy At Semiconductor Electrodes: Review and Recent Developments, *Electrochim. Acta*. 41 (1996) 967–973.
[57] R. Jiang, C. Chen, S. Zheng, The non-linear fitting method to analyze the measured M – S plots of bipolar passive films, *Electrochim. Acta*. 55 (2010) 2498–2504.
[58] N. Cabrera, N.F. Mott, Theory of the oxidation of metals, *Reports Prog. Phys.* 12 (1949) 163–184.
[59] N. Sato, M. Cohen, The Kinetics of Anodic Oxidation of Iron in Neutral Solution, *J. Electrochem. Soc.* 111 (1964) 512.
[60] F.P. Fehlner, Low-temperature oxidation, *Philos. Mag. B Phys. Condens. Matter; Stat. Mech. Electron. Opt. Magn. Prop.* 55 (1987) 633–636.
[61] L.F. Lin, C.Y. Chao, D.D. Macdonald, A Point Defect Model for Anodic Passive Films, *J. Electrochem. Soc.* (1983) 1874–1879.
[62] D.D. Macdonald, On the Existence of Our Metals-Based Civilization, *J. Electrochem. Soc.* 153 (2006) B213.
[63] C.-O.A. Olsson, D. Hamm, D. Landolt, Evaluation of Passive Film Growth Models with the Electrochemical Quartz Crystal Microbalance on PVD Deposited Cr, *J. Electrochem. Soc.* 147 (2002) 4093.
[64] B. Krishnamurthy, R.E. White, H.J. Ploehn, Non-equilibrium point defect model for time-dependent passivation of metal surfaces, *Electrochim. Acta*. 46 (2001) 3387–3396.
[65] M. Vankeerberghen, 1D steady-state finite-element modelling of a bi-carrier one-layer oxide film, *Corros. Sci.* 48 (2006) 3609–3628.
[66] A. Seyeux, V. Maurice, P. Marcus, Oxide Film Growth Kinetics on Metals and Alloys: I. Physical Model, *J. Electrochem. Soc.* 160 (2013) C189–C196.
[67] K. Leistner, C. Toulemonde, B. Diawara, A. Seyeux, V. Maurice, P. Marcus, Oxide Film Growth Kinetics on Metals and Alloys: II. Numerical Simluation of Transient Behavior, *J. Electrochem. Soc.* 160 (2013) C197–C205.
[68] J. Geringer, D.D. MacDonald, Modeling fretting-corrosion wear of 316L SS against poly(methyl methacrylate) with the Point Defect Model: Fundamental theory, assessment, and outlook, *Electrochim. Acta*. 79 (2012) 17–30.
[69] A. Fattah-alhosseini, A. Saatchi, M.A. Golozar, K. Raeissi, The transpassive dissolution mechanism of 316L stainless steel, *Electrochim. Acta*. 54 (2009) 3645–3650.
[70] C.Y. Chao, L.F. Lin, D.D. Macdonald, A Point Defect Model for Anodic Passive Films, *J. Electrochem. Soc.* 128 (1981) 1187.
[71] D.D. Macdonald, G.R. Engelhardt, The Point Defect Model for Bi-Layer Passive Films, 28 (2010) 123–144.
[72] D.D. Macdonald, Some personal adventures in passivity - A review of the point defect model for film growth, *Russ. J. Electrochem.* 48 (2012) 235–258.
[73] D. Macdonald, S. Biaggio, H. Song, Steady State Passive Films Interfacial Kinetic Effects and Diagnostic Criteria, *J. Electrochem. Soc.* 139 (1992) 170–177.
[74] D. Macdonald, S. Sharifi-Asl, G. Engelhardt, Review of the extraction of electrochemical kinetic data from electrochemical impedance data using genetic algorithm optimization, *Bulg. Chem. Commun.* 49 (2017) 53–64.
[75] S. Sharifi-Asl, M.L. Taylor, Z. Lu, G.R. Engelhardt, B. Kursten, D.D. Macdonald,

Modeling of the electrochemical impedance spectroscopic behavior of passive iron using a genetic algorithm approach, *Electrochim. Acta*. 102 (2013) 161–173.

[76] A. Fattah-alhosseini, M. Naseri, S.O. Gashti, S. Vafaeian, M.K. Keshavarz, Effect of anodic potential on the electrochemical response of passive layers formed on the surface of coarse- and fine-grained pure nickel in borate buffer solutions, *Corros. Sci.* 131 (2017) 81–93.

[77] P. Handzlik, K. Fitzner, Corrosion resistance of Ti and Ti-Pd alloy in phosphate buffered saline solutions with and without H2O2 addition, *Trans. Nonferrous Met. Soc. China (English Ed.* 23 (2013) 866–875.

[78] A. Fattah-Alhosseini, S. Vafaeian, Comparison of electrochemical behavior between coarse-grained and fine-grained AISI 430 ferritic stainless steel by Mott-Schottky analysis and EIS measurements, *J. Alloys Compd.* (2015).

[79] M. BenSalah, R. Sabot, E. Triki, L. Dhouibi, P. Refait, M. Jeannin, Passivity of Sanicro28 (UNS N-08028) stainless steel in polluted phosphoric acid at different temperatures studied by electrochemical impedance spectroscopy and Mott-Schottky analysis, *Corros. Sci.* 86 (2014) 61–70.

[80] A. Igual Muñoz, L. Casabán Julián, Influence of electrochemical potential on the tribocorrosion behaviour of high carbon CoCrMo biomedical alloy in simulated body fluids by electrochemical impedance spectroscopy, *Electrochim. Acta*. 55 (2010) 5428–5439.

[81] F. Mohammadi, T. Nickchi, M.M. Attar, A. Alfantazi, EIS study of potentiostatically formed passive film on 304 stainless steel, *Electrochim. Acta*. 56 (2011) 8727–8733.

[82] G. Rondelli, P. Torricelli, M. Fini, R. Giardino, In vitro corrosion study by EIS of a nickel-free stainless steel for orthopaedic applications, *Biomaterials*. 26 (2005) 739–744.

[83] H.H. Ge, G.D. Zhou, W.Q. Wu, Passivation model of 316 stainless steel in simulated cooling water and the effect of sulfide on the passive film, *Appl. Surf. Sci.* 211 (2003) 321–334.

[84] C. Boissy, C. Alemany-Dumont, B. Normand, EIS evaluation of steady-state characteristic of 316L stainless steel passive film grown in acidic solution, *Electrochem. Commun.* 26 (2013) 10–12.

[85] J. Pan, C. Leygraf, D. Thierry, A.M. Ektessabi, Corrosion Resistance for Biomedical Applications of TiO2 Films Deposited on Titanium and Stainless Steel by Ion - Beam - Assisted Sputtering, *J. Biomed. Mater. Res.* 35 (1997) 309–318.

[86] X. Lei, H. Wang, F. Mao, J. Zhang, M. Zhao, A. Fu, Y. Feng, D.D. Macdonald, Electrochemical behaviour of martensitic stainless steel after immersion in a H 2 S-saturated solution, *Corros. Sci.* 131 (2018) 164–173.

[87] N. Priyantha, P. Jayaweera, D.D. Macdonald, A. Sun, An electrochemical impedance study of alloy 22 in NaCl brine at elevated temperature. I. Corrosion behavior, *J. Electroanal. Chem.* 572 (2004) 409–419.

[88] D.D. MacDonald, A. Sun, An electrochemical impedance spectroscopic study of the passive state on Alloy-22, *Electrochim. Acta*. 51 (2006) 1767–1779.

[89] A. Fattah-alhosseini, F. Soltani, F. Shirsalimi, B. Ezadi, N. Attarzadeh, The semiconducting properties of passive films formed on AISI 316 L and AISI 321 stainless steels: A test of the point defect model (PDM), *Corros. Sci.* 53 (2011) 3186–3192.

[90] B. Hirschorn, M.E. Orazem, B. Tribollet, V. Vivier, I. Frateur, M. Musiani, Constant-Phase-Element Behavior Caused by Resistivity Distributions in Films, *J. Electrochem. Soc.* 157 (2010) C458.
[91] Y.F. Yin, R.G. Faulkner, Model predictions of grain boundary chromium depletion in Inconel 690, *Corros. Sci.* 49 (2007) 2177–2197.
[92] K. Bungardt, E. Kunze, E. Horn, Untersuchungen über den Aufbau des Systems Eisen-Chrom-Kohlenstoff, *Arch. Eisenhüttenwes*. 29 (1958) 193–203.
[93] J. Gobrecht, J. Gobrecht, Werkstofftechnik - Metall, 3rd ed., Oldenbourg Wissenschaftsverlag GmbH, (2009).
[94] K.D. Ralston, N. Birbilis, Effect of grain size on corrosion, *Corrosion*. 66 (2010) 1–4.
[95] P. Rosemann, P. Rosemann, Einfluss der Wärmebehandlung auf die Korrosionsbeständigkeit martensitischer nichtrostender Stähle, Otto-von-Guericke-Universität, Magdeburg, (2017).
[96] J. Park, Y. Park, The effects of heat-treatment parameters on corrosion resistance and phase transformations of 14Cr – 3Mo martensitic stainless steel, 451 (2007) 1131–1134.
[97] S.K. Bonagani, V. Bathula, V. Kain, Influence of tempering treatment on microstructure and pitting corrosion of 13 wt .% Cr martensitic stainless steel, *Corros. Sci.* 131 (2018).
[98] P. Rosemann, N. Kauss, C. Müller, T. Halle, Influence of solution annealing temperature and cooling medium on microstructure, hardness and corrosion resistance of martensitic stainless steel X46Cr13, *Mater. Corros.* 66 (2015) 1068–1076.
[99] M. Babutzka, A. Heyn, P. Rosemann, Influence of austenitizing and tempering on the corrosion behavior and sensitization of martensitic stainless steel X50CrMoV15, *Mater. Corros.* 69 (2018) 1338–1349.
[100] C.A. Stickels, Carbide Refining Heat Treatments for 52100 Bearing Steel, *Metall. Trans.* 5 (1974).
[101] J. Epp, H. Surm, O. Kessler, T. Hirsch, In situ X-ray phase analysis and computer simulation of carbide dissolution of ball bearing steel at different austenitizing temperatures, 55 (2007) 5959–5967.
[102] R.J. Kar, R.M. Horn, V.F. Zackay, The effect of heat treatment on microstructure and mechanical properties in 52100 steel, *Metall. Trans. A*. 10 (1979) 1711–1717.
[103] C. Huang, C. Zhang, L. Jiang, Y. Yang, Y. Liu, Isothermal heat treatment of a bearing steel for improved mechanical properties, *J. Alloys Compd.* 660 (2016) 131–135.
[104] C.C. Xu, G. Hu, Effect of deformation-induced martensite on the pit propagation behavior of 304 stainless steel, *Anti-Corrosion Methods Mater.* 51 (2004) 381–388.
[105] J. Wang, L.F. Zhang, Effects of cold deformation on electrochemical corrosion behaviors of 304 stainless steel, *Anti-Corrosion Methods Mater.* 64 (2017) 252–262.
[106] Y. Fu, X. Wu, E.H. Han, W. Ke, K. Yang, Z. Jiang, Effects of cold work and sensitization treatment on the corrosion resistance of high nitrogen stainless steel in chloride solutions, *Electrochim. Acta*. 54 (2009) 1618–1629.
[107] N. Solomon, I. Solomon, Effect of deformation-induced phase transformation on AISI 316 stainless steel corrosion resistance, *Eng. Fail. Anal.* 79 (2017) 865–875.
[108] D. Zhang, X. Gao, G. Su, Z. Liu, N. Yang, L. Du, R.D.K. Misra, Effect of Tempered Martensite and Ferrite/Bainite on Corrosion Behavior of Low Alloy Steel Used for Flexible Pipe Exposed to High-Temperature Brine Environment, *J. Mater. Eng. Perform.*

27 (2018) 4911–4920.
[109] S. He, Effect of Deformation-Induced Martensite on Protective Performance of Passive Film on 304 Stainless Steel, *Int. J. Electrochem. Sci.* 13 (2018) 4700–4719.
[110] H. Luo, H. Su, G. Ying, C. Dong, X. Li, Effect of cold deformation on the electrochemical behaviour of 304L stainless steel in contaminated sulfuric acid environment, *Appl. Surf. Sci.* 425 (2017) 628–638.
[111] A. Abbasi Aghuy, M. Zakeri, M.H. Moayed, M. Mazinani, Effect of grain size on pitting corrosion of 304L austenitic stainless steel, *Corros. Sci.* 94 (2015).
[112] L. Jinlong, L. Tongxiang, W. Chen, D. Limin, Effect of ultrafine grain on tensile behaviour and corrosion resistance of the duplex stainless steel, *Mater. Sci. Eng. C*. 62 (2016) 558–563.
[113] J. Epp, X-Ray Diffraction (XRD) Techniques for Materials Characterization, in: Mater. Charact. Using Nondestruct. Eval. Methods, (2016) 81–124.
[114] G. Will, G. Will, Powder diffraction: The rietveld method and the two stage method to determine and refine crystal structures from powder diffraction data, (2006).
[115] I. Bösing, J. Thöming, M. Baune, Electrolyte Composition for Distinguishing Corrosion Mechanisms in Steel Alloy Screening, *Int. J. Corros.* 2017 (2017).
[116] S. Haupt, H.H. Strehblow, A combined surface analytical and electrochemical study of the formation of passive layers on Fe Cr alloys in 0.5 M H2SO4, *Corros. Sci.* 37 (1995) 43–54.
[117] R.K. Gupta, R.K. Singh Raman, C.C. Koch, Electrochemical characteristics of nano and microcrystalline Fe-Cr alloys, *J. Mater. Sci.* 47 (2012) 6118–6124.
[118] L. Jinlong, L. Hongyun, Comparison of corrosion properties of passive films formed on phase reversion induced nano/ultrafine-grained 321 stainless steel, *Appl. Surf. Sci.* 280 (2013) 124–131.
[119] T.R. McNelley, M.R. Edwards, A. Doig, D.H. Boone, C.W. Schultz, The effect of prior heat treatments on the structure and properties of warm-rolled AlSl 52100 steel, *Metall. Trans. A*. 14 (1983) 1427–1433.
[120] Z. Szklarska-Smialowska, W. Kozlowski, Electrochemical and Ellipsometric Investigations of Passive Films Formed on Iron in Borate Solutions, *J. Electrochem. Soc.* 131 (1984) 234–241.
[121] S. Vafaeian, A. Fattah-Alhosseini, M.K. Keshavarz, Y. Mazaheri, The influence of cyclic voltammetry passivation on the electrochemical behavior of fine and coarse-grained AISI 430 ferritic stainless steel in an alkaline solution, *J. Alloys Compd.* 677 (2016) 42–51.
[122] B. Kuhfuss, E. Moumi, V. Piwek, Micro rotary swaging: Process limitations and attempts to their extension, *Microsyst. Technol.* 14 (2008) 1995–2000.
[123] B. Köhler, B. Clausen, H.-W. Zoch, B. Köhler, B. Clausen, H.-W. Zoch, Kolloquium Mikroproduktion, BIAS Verlag, (2017).
[124] E. Rauschnabel, V. Schmidt, Modern applications of radial forging and swaging in the automotive industry, *J. Mater. Process. Technol.* 35 (1992) 371–383.
[125] Y. Yi, P. Cho, A. Al Zaabi, Y. Addad, C. Jang, Potentiodynamic polarization behaviour of AISI type 316 stainless steel in NaCl solution, *Corros. Sci.* 74 (2013) 92–97.
[126] L. Veleva, M.A. Alpuche-Aviles, M.K. Graves-Brook, D.O. Wipf, Comparative cyclic voltammetry and surface analysis of passive films grown on stainless steel 316 in

concrete pore model solutions, *J. Electroanal. Chem.* 537 (2002) 85–93.
[127] R.A. Antunes, M.C.L. De Oliveira, I. Costa, Study of the correlation between corrosion resistance and semi-conducting properties of the passive film of AISI 316L stainless steel in physiological solution, *Mater. Corros.* 63 (2012) 586–592.
[128] S. Haupt, H.H. Strehblow, A combined surface analytical and electrochemical study of the formation of passive layers on FeCr alloys in 1M NaOH, *Surf. Interface Anal.* 21 (1994) 514–525.
[129] X. Shang, Electrochemical Analysis of Passivation Film Formation on Steel Rebar in Concrete, *Int. J. Electrochem. Sci.* 11 (2016) 5870–5876.
[130] A. Kocijan, Č. Donik, M. Jenko, Electrochemical and XPS studies of the passive film formed on stainless steels in borate buffer and chloride solutions, *Corros. Sci.* 49 (2007) 2083–2098.
[131] N. Ramasubramanian, Analysis of passive films on stainless steel by cyclic voltammetry and Auger spectroscopy, *J. ….* (1985) 793–798.
[132] S. Chakri, A.N. Patel, I. Frateur, F. Kanoufi, E.M.M. Sutter, T.T.M. Tran, B. Tribollet, V. Vivier, Imaging of a Thin Oxide Film Formation from the Combination of Surface Reflectivity and Electrochemical Methods, *Anal. Chem.* 89 (2017) 5303–5310.
[133] J. Morales, P. Esparza, R. Salvarezza, S. Gonzalez, The pitting and crevice corrosion of 304 stainless steel in phosphate-borate buffer containing sodium chloride, *Corros. Sci.* 33 (1992) 1645–1651.
[134] A. Shahryari, S. Omanovic, J.A. Szpunar, Electrochemical formation of highly pitting resistant passive films on a biomedical grade 316LVM stainless steel surface, *Mater. Sci. Eng. C*. 28 (2008) 94–106.
[135] M. Metikoš-Huković, Z. Grubač, S. Omanovic, Change of n-type to p-type conductivity of the semiconductor passive film on N-steel: Enhancement of the pitting corrosion resistance, *J. Serbian Chem. Soc.* 78 (2013) 2053–2067.
[136] D.D. Macdonald, A. Sun, N. Priyantha, P. Jayaweera, An electrochemical impedance study of Alloy-22 in NaCl brine at elevated temperature: II. Reaction mechanism analysis, *J. Electroanal. Chem.* 572 (2004) 421–431.
[137] K. Sieradzki, R.C. Newman, Percolation Model for Passivation in Stainless Steels., *J. Electrochem. Soc.* 133 (1986) 1979–1980.
[138] S. Qian, R.C. Newman, R.A. Cottis, Validation of a Percolation Model for Passivation of Fe-Cr Alloys: Two-Dimensional Computer Simulations, *J. Electrochem. Soc.* 137 (1990) 435–439.
[139] C.-O. a. Olsson, D. Landolt, Film Growth during Anodic Polarization in the Passive Region on 304 Stainless Steels with Cr, Mo, or W Additions Studied with EQCM and XPS, *J. Electrochem. Soc.* 148 (2001) B438.
[140] E. Sikora, J. Sikora, D.D. Macdonald, A new method for estimating the diffusivities of vacancies in passive films, *Electrochim. Acta*. 41 (1996) 783–789.

STUDENTS' WORK

In this dissertation, the results of no students' works are included.

EIGENSTÄNDIGKEITSERKLÄRUNG

Hiermit erkläre ich, Ingmar Bösing, dass die vorliegende Dissertation mit dem Titel „Effect of Material Treatments on the Growth Kinetics of Passive Films on Steel Alloys“ gemäß §5 der Promotionsordnung des FB4 der Universität Bremen,

von mir ohne unerlaubte fremde Hilfe angefertigt worden ist.

Ich bestätige, dass ich keine anderen als die von mir angegebenen Quellen und Hilfsmittel benutzt habe.

Darüber hinaus versichere ich, dass ich die den benutzten Werken wörtlich oder inhaltlich entnommenen Stellen als solche kenntlich gemacht habe.

Ich bestätige, dass meine vorliegende Arbeit nach den geltenden Prinzipien der guten wissenschaftlichen Praxis der Universität Bremen und der Deutschen Forschungsgemeinschaft verfasst ist.

Ort/Datum Unterschrift

Contribution to Publications

	Electrolyte comp. for distinguishing corr. mech.in steel alloy screening	The influence of microstr. deformation on the corrosion resistance of cold formed stainless steel	Influence of heat treat on the microstr.and corr. resistance of mart. stainless steel	Influence of Syst. Changed Mart. Content on the Passive Film Prop. of Aust. Stainless Steel in Neutr. Electrolyte	Effect of Heat Treatment of Mart. Stainless Steel on Passive Layer Growth Kinetics
Journal (Year)	*Int. J of Corr. (2017)*	*Matec W. of Conf. (2018)*	*AIP Advances (2019)*	*Int. J. of Electrochem. Sci. (2020)*	*Corr. and Mat. Degr. (2020)*
Concept	IB, JT, MB	IB, JT, MB, MH, BK	IB, JT, MB	IB, JT, MB	IB
Methods	IB	IB, IBo	IB, LC	IB, IBo	IB
Measurements	IB	IB, IBo	IB, LC	IB	IB
Analysis	IB	IB	IB	IB	IB
Resources	JT, MB	JT, MB	JT, MB, HWZ, MS	JT, MB	JT
Writing	IB	IB	IB	IB	IB
Review and Editing	IB, JT, MB	IB, JT, MB, JE, MH, BK	IB, MB, JT, MS, LC	IB, JT, MB, JE, Ibo	JT
Visualization	IB	IB	IB	IB	IB
Supervision	JT, MB	JT, MB	JT, MB	JT, MB	JT

Abbreviation: IB: Ingmar Bösing, JT: Jorg Thöming, MB: Michael Baune, Ibo: Ilya Bobrov, JE: Jeremy Epp, MH: Marius Herrmann, LC: Lena Cramer, HWZ: Hans-Werner Zoch, MS: Matthias Steinbacher, BK Bernd Kuhfuss